In situ Synchrotron X-ray Scattering Studies of Atomic Structure and Surface Adsorbates at the Solid-Liquid Interface

Michael Cormack

Thesis submitted in accordance with the requirements of the University of Liverpool for the degree of Doctor in Philosophy

Oliver Lodge Laboratory

Department of Physics

UNIVERSITY OF LIVERPOOL

October 2009

Abstract

Synchrotron radiation facilities have been used to probe the effects of both potential and temperature on the structure of single crystal surfaces, and adsorbates on these surfaces. When possible, cyclic voltammetry (CV) measurements have been used to complement x-ray results. This provides a more detailed understanding of the electrochemical processes that are occurring during the x-ray measurements.

In situ surface x-ray scattering (SXS) has become a powerful probe of the atomic structure at the metal–electrolyte interface. In this thesis, I describe an experiment in which a Pt(111) sample is prepared under ultra-high vacuum (UHV) conditions to have a p(2x2) oxygen layer adsorbed on the surface. The surface is then studied using SXS under UHV conditions before successive transfer to a bulk water environment and then to the electrochemical environment (0.1 M KOH solution) under an applied electrode potential. The Pt surface structure is examined in detail using crystal truncation rod (CTR) measurements under these different conditions. It is important to note that probing adsorbed layers of OH^-, oxygen, and water with x-rays is experimentally challenging, as these species interact weakly with the incoming x-ray beam. In spite of this, results which both confirm and challenge current theory were obtained.

Surface reconstructions of low index single crystal samples are well documented, yet a fundamental understanding of the reconstruction process is lacking. Results are presented firstly for the (111) and (100) faces of Au in 0.1 M KOH. The Au(111) - (px$\sqrt{3}$) reconstruction is presented first, as an example of a surface reconstruction involving relatively little mass transport (approx 4.4%) during the phase change. Following on from this, the Au(100) reconstruction is studied. This surface is known to reconstruct to a Au(100)-(5x20) phase, termed the "hex" reconstruction. In this case, the mass transport during the phase change from the bulk termination to the "hex" phase is typically quoted at approx 20%. These reconstructions are driven by the potential across the electrode/electrolyte interface, controlled experimentally. For both systems, a small change in temperature (a range of 40 Kelvin) produced marked changes in the surface structure. For the Au(100) experiments, bromine anions were introduced into the system to inhibit surface oxide formation, as this was believed to

be responsible for the formation of an "unrotated" domain of the reconstruction. This theory seems to be supported by the findings, as the introduction of bromine resulted in a considerable reduction in the amount of unrotated reconstruction domains.

As a continuation of the temperature based measurements, a reactive adsorbate in the form of CO molecules on a Pt(111) substrate was studied. Adsorbed CO is known to form an ordered layer on Pt(111), the phase of which depends on the interface potential. This system is of particular prominence in modern surface science, as the behaviour of adsorbed CO molecules as a poison on Pt catalysts is currently seen as a barrier to widespread usage of hydrogen fuel cells. Importantly, such fuel cells typically operate at non ambient temperatures of around 80 - 100 °C. Probing the effect of temperature on the adsorbed CO layer provides some insight into its behaviour at temperatures more relevant to potential commercial applications.

Acknowledgements

First and foremost, I would like to say a huge thank you to my supervisor, Professor C. A. Lucas, for his vast contribution during my PhD studies. As well as his excellent scientific support throughout the past four years, he has consistently given me sound advice on various topics (which I have usually ignored at my peril). I am still due a squash lesson from him, and look forward to receiving this. Alongside the specific input Chris has had into my work regarding the systems I have studied, he has also provided me with an in depth insight into the academic processes surrounding university life. Importantly, he always ensured that whilst the synchrotron experiments were challenging, there was a sense of humour accompanying them. This, along with the compulsory alcohol consumption (I will never forget my "dry run" at the ESRF – a real eye opener!) made these times enjoyable in spite of the long hours.

When I first started my PhD, I was welcomed into the CMP office warmly by a large number of PhD/Post Doctoral students. I met many characters, including John Price Morris (aka "Johnny long-lunch" – we shared many beers), Mark Gallagher (that "Shirley" comment still makes me laugh aloud!), Dave Mercer (who performed a "puddle stunt" which was simply brilliant), Raymond Fan (NO MORE COMPUTER GAMES RAY – stick to the darts and poker!), Markos Skoulatos (guitar genius – too many late nights though...), and Keith Williams (the technician – always willing to help out, and some of those cups of coffee saved my life). I will never forget these people, and all the laughs, jokes, and good times we shared.

From my first day in the office up to the point they moved on, there were two people in particular who helped me no end and for this deserve a special mention. I

am deeply grateful to Simon Lee and Ben Fowler for all their efforts in helping me with my day to day work. At times, they displayed so much patience regarding my lack of IT skills/knowledge that I started to question their humanity - I am yet to tell them I now work in an IT department, for fear of causing cardiac arrest!!! It still amuses me to think that every Matlab lesson from Ben involved an example filename which was "coincidently" a direct insult to myself ("mickisstupid", "thisiseasymick" and "sillymick" are just a few of the nicer examples). One thing which helped in all this was the weekly football thrashing we used to hand out to the nuclear structure team. I think without this, Simon and Ben may have struggled to persist in their quest to help. However, I think Ben would agree it was all worth it just to see my "bollard dance" go wrong one night – a very painful experience indeed (and apparently hilarious). On a more serious note, they really stuck their neck out, giving me their time and effort on too many occasions to mention. For this, I will always be grateful.

Synchrotron Experiments abroad were always an adventure, and I was always accompanied by Paul Thompson, a Beamline scientist based at BM28 at the European Synchrotron Radiation Facility (ESRF). Paul was always extremely proficient in aligning the beamline, helping with the x-ray experiments, and also helped with the UHV preparation (for ESRF based experiments). Having said all this, perhaps his most notable talent was his uncanny ability to always make time for a Guinness, as well as his ability to summarise just about every situation, regardless of the severity, with his catchphrase "Well, it's got 2 chances..." I am deeply saddened that his Ford Mondeo is no longer with us, even if he has replaced it with another Ford Mondeo! At this point I would also like to thank the entire beamline staff at BM28, for their expert help and guidance during experiments there. It was always a well ran operation and

this helped no end in the success of the experiments performed there – especially the shorter ones whereby a smooth start was imperative.

The experiments based at the Argonne National Laboratory (APS) were mainly performed at the 12BM / BESSRC-CAT beamline, and we were lucky to have the assistance of Nadia Leyarovska. Nadia was extremely resourceful regarding the solution of some of the teething problems we faced there, and was always extremely supportive of our work.

Experiments at the APS would not have been possible if it were not for the huge input from our collaborators based at the Materials Science Division (MSD). Nenad Markovic and his team, including Vojislav Stamenkovic and Dusan Strmcnik, played an integral part in all aspects of the work I participated in at the APS. Not only would the team help with the preparation, operation, and design of the experiments, they were also extremely hospitable and made my visits there very enjoyable. I think I single-handedly saved the reputation of English food during one of my residential work placements there, when I cooked a stew for Dusan and Vlado when staying at their house. After being insulted for a whole week ("what do English people cook – fish and chips every day?...", "how much did he drink last night?" – "EVERYTHING"), I watched in awe as Dusan ate 5 bowls of "scouse" in ONE sitting! International culinary relations aside, it was extremely impressive to see first hand the level of professionalism adhered to on a daily basis by the Markovic team. I thank them all for the opportunity to work with them, and sincerely hope we stay in touch.

Most of my undergraduate friends from Liverpool continued studying, meaning there have been some ever-present faces during my studies. Initially, myself, Joe Parle, Andy Bowfield and Alex Brownrigg were inseparable (which means lots of

misspent nights in the pub), but we got through our undergraduate course by helping each other whenever necessary. Andy moved straight onto PhD studies (as did I) after the BSc, and the year later we were followed by Alex and Joe into PhD studies. Our undergraduate course provided many fun times which I will not forget. Alex joined the Lucas group after his masters (hence was the student after myself), and I have reserved special mention for him.

During our studies and experiments, Alex and I have certainly had some interesting times. I think between us we have more stories than most other entire physics departments, especially regarding our experiments abroad. To list a few in very brief terms, there is the time when I locked myself out of my hotel room ("Mickey Redsocks" – cheers ben, it stuck), Alex's BMX disaster (I will never forget the glove full of ice), "Dollargate" (DID YOU REALLY PUT IT IN YOUR HOLD LUGGAGE!!!), the 12 hour airport delay (say no more), Simons wedding, "ACCESS denied" (does "La Quinta" ring any bells?), and many more. Alex was set a high bar given the "redsocks" escapade but he is nothing if not game. Professionally, his effort and desire to succeed are matched only by his physical durability, which is why I know he will go far no matter what he chooses to do. If I could do it all again, he is one of the few things I would want to remain constant (and the same goes to Andy and Joe). Following on from this, I must mention JJ and Downey – not so much diamonds in the rough as best of a bad bunch (joke), but good friends to me who have always been there. It is at this point, when considering my past, I would like to say thank you to two former lecturers, Maurice Tickle and Dave Hardaker, who were inspirational in converting a young man with no general direction in life into someone who, well, now has slightly more direction?!!

Throughout my studies, and in general, I have been extremely fortunate to have a number of very special people who are always there for me. I cannot put down on paper what my Mum and Dad have done for me over the years, so will not attempt to. I can only say that I am completely aware of the sacrifices they have made and the effort they have invested into not just my own upbringing, but that of Robert and Jennifer's. I will forever appreciate this, and hope that they take some satisfaction/pride out of my academic journey. I have a very close relationship with my Nan, who has always supported my studies, and I completed my A-levels by studying at her (nice, quiet) house of an evening. I hope she is proud of what I have done, even if she wasn't impressed when, during dinner one evening, I told her I couldn't eat chicken from the bone. I know that certain people no longer with us would also have been pleased for me. Colette's parents must be thanked for helping us with moving into our house, and my aunts Ann, Kath, and Kathleen, have all contributed to helping me through my studies.

Finally, I must save my biggest thank you for Colette, who has in fairness at times has had to put up with my unorthodox lifestyle (and mood) over the past 4 years - especially since we moved in together. This can not have been easy, and I perhaps should have been more sensitive to her position as a working professional. In spite of this, she has always been there for me, and would be the first to admit we have had many fun times together.

Contents

Chapter 1

Introduction

The past few decades have seen significant advances in the fundamental understanding of the electrode-electrolyte interface. The developments in synchrotron radiation facilities, coupled with the design of thin layer geometry electrochemical cells which enable the immersed interface to be accessed by incoming radiation, have been key contributing factors to the progress made [1-2]. Previously, problems arose when *ex situ* techniques, such as low energy electron diffraction (LEED) and x-ray photoelectron spectroscopy (XPS), were used to monitor surface conditions after electrochemical measurements had been taken. The sample transfer from the liquid environment into UHV leads to loss of control of the electrochemical potential and thus unwanted desorption/adsorption of electrolyte, so is not ideal. Electron probe based techniques are not feasible when the surface is immersed, due to the absorption of the probing electrons in the liquid overlayer. Whilst basic Cyclic Voltammetry (CV) measurements are well established as a means of probing the interface, the characteristic I-V curves fail to shed light on the structural composition of the interface. As the structure of the interface is crucial in determining the macroscopic kinetic rates of electrochemical reactions, structure sensitive techniques such as *in situ* surface x-ray scattering (SXS), as well as in situ scanning tunneling microscopy (STM), will play a key role in both the short and long term future of interfacial surface science.

Electrochemical interfaces feature in many aspects of analytical, synthetic, and materials chemistry, as well as in chemical and photochemical energy conversion processes [3-4]. In the past, these interfaces have primarily been treated empirically, with only limited understanding of the fundamental molecular-level processes associated with the bond making and bond breaking events in an inherently complex multi-component environment. Since the early 1990s, STM and SXS techniques have enabled the transformation of electrochemistry from a largely phenomenological subject into a discipline that addresses atomic/molecular-level issues at a level of detail that is comparable with that achieved in ultra-high vacuum (UHV) based surface science [5]. Of particular interest have been potential-driven phenomena at ambient temperatures, ranging from ordering, phase transitions and mobility of both metal surface atoms [6-7] and adsorbed layers [8-10] to the surface compositions and segregation profiles of bimetallic systems [11-12]. These phenomena will now be discussed briefly.

As in the UHV environment [13], the extraction of structural information, such as surface coverage, surface roughness and layer spacings (both adsorbate-substrate distances and the expansion/contraction of the substrate surface atoms themselves), at the electrified solid-liquid interface relies on measurement of the crystal truncation rods (CTR's). By combining specular CTR results (where the momentum transfer, **Q,** is entirely along the surface normal direction) with non-specular CTR results (where **Q** has an additional in-plane contribution) it is possible to build up a 3-dimensional picture of the atomic structure at the electrode surface. If the surface or adlayer adopts a different symmetry from that of the underlying bulk crystal lattice then the scattering from the surface becomes separate from that of the bulk in reciprocal space and it is possible to measure the surface scattering independently. This independent

structural information can be combined with CTR analysis to give the registry of the surface layers with respect to the bulk lattice [13-15].

A key aspect in the study of single crystal metal electrodes is the preparation of the surface prior to the experiment and the transfer of the crystal into the electrochemical x-ray cell. One approach is to prepare the surface in an UHV environment by cycles of ion sputtering and annealing. This methodology has the advantage that the surface quality can be checked during preparation by standard surface science techniques such as low energy electron diffraction (LEED) and auger electron spectroscopy (AES). An alternative method for surface preparation for some crystals is to use the flame-annealing technique [16-18]. After pre-treatment to produce a flat, well oriented surface, the crystal is heated in a hydrogen or butane flame and then allowed to cool in air or hydrogen/argon before transfer to the electrochemical x-ray cell. This procedure has been used successfully for the preparation of Au(*hkl*) and Pt(*hkl*) surfaces. Other monometallic metal surfaces, such as Cu, Ag and Ni, cannot be prepared by flame-annealing methods. Other than UHV preparation, the most successful method for these surfaces has been to use a long pre-anneal of the surface in a forming gas, such as hydrogen, followed by a short electrochemical etch, rinsing with water and then direct transfer into the electrochemical x-ray cell [2, 19-20].

Modern surface crystallographic studies have shown that on the atomic scale most clean metals tend to minimize their surface energy by two kinds of surface atom rearrangements, *relaxation* and *reconstruction*, which collectively may be called *restructuring*. Relaxation of metal surfaces is usually defined as small interlayer spacing changes relative to the ideal bulk lattice [21-25]. The displacements should be small compared to near-neighbour distances, such that no bond-breaking/bond-making events take place within the substrate. Adsorbate-induced relaxations occur in

many varieties: as *interlayer spacing changes*, where the top layer of metal atoms undergo inward or outward relaxation; *lateral relaxation*, in which surface atoms are shifted parallel to the surface (for example, adsorbate-induced collective rotation of substrate atoms around an adsorbate site), and *layer buckling*, whereby a coplanar atomic layer loses its coplanarity because of preferred adsorption on a particular surface site. Reconstruction, on the other hand, involves large atomic displacements both perpendicular to and parallel to the surface plane leading to re-bonding and a change in the periodicity of the surface with respect to the underlying substrate. The periodicity of the surface can be defined by Woods' notation; for example an unreconstructed Pt(110) surface would be termed as (1x1) whereas if the surface unit cell size was doubled in one of the primary vector directions it would be termed as (2x1) *etc.*

The present knowledge of surface restructuring at electrified metal-solution interfaces would not have been possible without certain key advances, for example, the many excellent UHV [21] and theoretical studies [26]. A further advance was the advent of *in situ* surface sensitive techniques and the development of efficient methods for surface preparation of monometallic and bimetallic single crystal surfaces and their clean transfer from UHV into the electrochemical environment

There have been numerous experimental and theoretical studies of the relaxation of metal surfaces in UHV and a significant data base now exists based mainly on LEED studies. In UHV, on unreconstructed clean low-index single crystal surfaces it is often found that the outermost layer of atoms is contracted toward the second atomic layer. The tendency for surface contraction has been explained by Finnis and Heine using the Hellman-Feynmen theorem, which states that the force on an ion is just the electrostatic force from the other ions and the self-consistent electron density.

Adsorption onto clean metal surfaces in UHV often reverses the surface contraction such that the outermost layer of atoms is *expanded* away from the second atomic layer. These concepts can be extended to the metal-electrolyte interface and, indeed, surface relaxation has been observed at coinage-metal surfaces (Cu, Ag, and Au) as well as at Pt-group monometallic and bimetallic single crystal surfaces in the electrochemical environment. .

As noted previously, accurate determination of adsorbate-induced changes in surface-normal structure , *i.e.,* the Δd_{12} inter-planar spacing between the first and the second atomic layers, can be achieved by measuring the CTR's [14, 27-31]. Previous reviews summarized adsorbate induced relaxation and reconstruction on well defined Pt(*hkl*) and Pt-bimetallic surfaces in aqueous electrolytes at electrode potentials at which a maximum surface coverage of adsorbed species is established [32-33]. The data revealed that either close to the hydrogen evolution potential (0.05 V) or close to the onset of irreversible oxide formation (ca. 1.0 V) the surface expansion increases in the sequence Pt(111) < Pt (100) << Pt(110) in both H_2SO_4 and KOH solutions. It has been proposed that the observed differences in relaxation of Pt(*hkl*) arise due to the interplay between the Pt-adsorbate bonding and the coordination of surface atoms, for details see [32].

Direct confirmation of the relationship between surface relaxation and binding interaction is obtained in experiments in which relatively weakly-bonded H_{upd} is displaced from the surface by strongly-bonded CO. As shown previously [32], following the adsorption of CO onto Pt(111) at 0.05 V, the surface expansion increases from 2% on the H_{upd}-covered surface to 4% on the CO-covered surface, supporting the proposition that the difference in relaxation can be correlated with metal-adsorbate bonding, the Pt-CO interaction being much stronger than the Pt-H_{upd}

interaction. The surface coverage by CO at 0.05 V is 0.75 ML and a p(2x2)-3CO structure is formed that can be measured by SXS. The potential stability of the p(2x2)-3CO structure is strongly affected by the oxidation of a small fraction of the CO adlayer so that at 0.65 V a ($\sqrt{19}$x$\sqrt{19}$)R23.4°-13CO structure (hereafter dubbed the "$\sqrt{19}$" structure), forms with Θ_{CO} = 0.68 ML. Recently, the structural relaxation of the Pt(111)-CO surface has been studied in detail in the presence of the "$\sqrt{19}$" structure [34].

The surface expansion of the group 1B metals, Cu, Ag and Au, particularly the close-packed (111) surfaces, have been studied in the most detail. In terms of surface expansion effects, the 1B metals are more difficult to study than Pt as no H_{upd} is formed and so it is difficult to correlate structural changes with well-defined adsorption processes. Furthermore, the Au(*hkl*) surfaces reconstruct at negative potential which limits the potential window where the surfaces are in the unreconstructed state. Despite these difficulties relaxation at the Au(111) surface was recently studied by a combination of SXS and surface stress measurements. For potentials positive of the potential of zero charge (*pzc*), where the surface is unreconstructed, increasing positive surface charge causes a decrease in the tensile stress, a result that can be understood on the basis of a simple "jellium" model [35]. Correspondingly one might expect that positive surface charge would lead to an increase in the surface expansion due to the apparent weakening of the surface bonds but it was found that the opposite was true. Measurements of the surface expansion of Au(111) in 0.5 M H_2SO_4 solution show that close to the *pzc* the surface is expanded by ~1.5% of the bulk layer spacing and that this expansion decreases with increasing surface charge to ~0.2% at the positive potential limit [36]. In order to rationalize the apparent conflict between the surface stress and surface expansion results, first

principle density functional theory (DFT) calculations of Au(111) surface relaxation were performed. For the uncharged surface the calculations gave an outward relaxation of 1.3% of the bulk layer spacing, in good agreement with the x-ray measurements. Based on these results, it was proposed that surface relaxation is a trade-off between cohesion between adjacent atoms and the band energy due to the band structure of the crystal. The density of states (DOS) for the relaxed surface is depleted near the Fermi level but enriched in the interval –4 eV to –1 eV below the Fermi level. The authors concluded that the shifting of the crystal bands to lower energies is the driving force for the outward relaxation.

It is now well established that in UHV, the clean low-index faces of some *fcc* metals tend to exhibit reconstruction under certain conditions of sample temperature and surface preparation. This is certainly true of Pt and Au whereas most other *fcc* metals (e.g. Cu, Ni, Ag…) do not reconstruct. The tendency of the clean Pt and Au surfaces to reconstruct in UHV has been explained by Ho and Bohnen using first principle calculations [37] and later by Norskov using a combination of local density functional calculations and modelling within the effective medium theory [38]. Both theories predicted that the participation of d electrons in bonding in the solid and the decrease of the kinetic energy of delocalized electrons at the surface play a decisive role in the stabilization of the experimentally-observed missing-row reconstructions of Au(110) and Pt(110) surfaces. Several experiments also illustrated that, in the UHV environment, the adsorption of atoms and molecules on clean metal surfaces has a dramatic effect on the metal surface relaxation and can cause clean metal surfaces to reconstruct or to deconstruct ("lift") back to the (1x1) phase [32]. The thermodynamic driving force for adsorbate-induced restructuring is the formation of strong adsorbate-substrate bonds that are comparable to, or stronger than, the bonds between the

substrate atoms in the clean surface. Although the same thermodynamic effects may be valid in electrochemistry, significant differences in adsorbate-induced restructuring in UHV and in electrochemical systems have been observed. As has been demonstrated [32-33], these differences can be accounted for in terms of (i) the presence of co-adsorbed solvent and adsorbed species, and (ii) differing surface potentials (φ) and (continuously adjustable) variations in electrode potential. The former effect communally results in the formation of an adsorbed layer of water, the adsorption of hydrogen, reversible/irreversible formation of oxygenated species and the adsorption of anions from supporting electrolyte. The latter effect results in potential-induced changes of the surface electron density. Although in an electrochemical environment thermodynamic and/or electronic effects are difficult to decouple, taken together these two effects play a major role in determining surface restructuring in electrochemical systems.

Given that adsorbate-induced lifting of reconstruction is observed only at Au(*hkl*)-solution interfaces, the work focuses on the transition between the reconstructed ("rec") and (1x1) phases of two Au(*hkl*) surfaces in the electrochemical environment. The reconstructions of the Au(*hkl*) surfaces are observed at negative potentials where the surfaces are (almost) free of strongly adsorbing anions. For Au(111), the reconstruction is rather complex and involves a small increase in the surface density which leads to a large unit cell, with a (23x$\sqrt{3}$) periodicity [39-40]. Of particular interest in this regard has been the behaviour of Au(100) in alkaline as well in acidic electrolytes. The potential stability of the "hex" reconstruction in the electrochemical environment has been studied by cyclic voltammetry, *ex situ* emersion LEED experiments, STM and x-ray diffraction [7, 32-33, 41-42]. In both acid and alkaline solutions there is good agreement between the experimental

techniques that the "5x20" reconstruction can be reversibly lifted and formed upon cycling the applied potential although the exact details of the transition can depend on the potential scan rate and sample history.

The chemisorption of atoms or molecules onto monocrystalline metal surfaces characteristically yields ordered adlayer structures. This ordering can be understood, in general terms, from a balance between the preference for adsorbate bonding in specific coordination sites and the dominant adsorbate-adsorbate interaction at higher coverages. This leads to a rich variety of structural behaviour that is ideally suited to study by SXS due to the resolution of the technique

The adsorption of anions on metal electrodes has been one of the major topics in surface electrochemistry. Specific adsorption of anions occurs when the anion loses all or part of its solvation shell and forms a direct chemical bond with the substrate. In this situation the surface coverage by anions can be high and the adlayer tends to form a close-packed structure that depends critically on the surface atomic geometry of the underlying substrate and the balance between the anion-metal and anion-anion interaction energies. The structures of halide anions adsorbed onto Au(*hkl*), Ag(*hkl*) and Pt(*hkl*) low-index surfaces have been the most widely studied systems by SXS and a comprehensive review of ordered anion adlayers on metal electrodes is given by Magnussen [41].

On the close-packed (111) surfaces, halide anions form hexagonal overlayers that undergo electrocompression and a variety of structures are observed; commensurate, incommensurate, uniaxially incommensurate and rotated phases. On the more open (100) and (110) metal surfaces the symmetry of the substrate differs from the energetically-favourable hexagonal symmetry of the halide adlayers and, in addition, the corrugation potential is higher and this favours the formation of low-

order commensurate phases. In fact, on (100) surfaces the most commonly observed structure is the c(2x2) phase, a structure with a simple square symmetry and a surface coverage of 0.5 adatoms per metal surface atom. This structure has been observed on Ag(100), Cu(100), Pt(100) and Pd(100) for Cl^-, Br^- and I^- halide anions despite the fact that the atomic size mismatch can lead to large anion-anion bondlengths compared to the bondlengths found in the corresponding hexagonal phases [43-46].

It is only on the Au(100) surface that the anion-anion interaction is sufficient to perturb the influence of the substrate corrugation potential. For example, the bromide adlayer on Au(100) undergoes a commensurate-incommensurate transition where a commensurate c($\sqrt{2}$x$\sqrt{2}$)R45° structure transforms continuously to an incommensurate c($\sqrt{2}$xp)R45° structure [47]. This implies that the elastic interactions between the relatively large Br adatoms (which would favour hexagonal packing) dominate over the adsorbate-substrate interaction.

The surface electrochemistry of CO adsorbed on transition metal surfaces has been the subject of intense theoretical and experimental work; for an overview see refs [32, 48-49]. In these studies there has been an emphasis on linking the microscopic structure of the CO adlayer to the thermodynamics and other macroscopic electrochemical responses at electrified interfaces. Whereas information regarding macroscopic properties has come from classical electrochemical techniques [50-52], the chemical, physical and structural properties on the atomic scale have been obtained from either a combination of *in-situ* STM and vibrational spectroscopy [53-54] or SXS and vibrational spectroscopy [55]. The adsorptive and catalytic properties of CO adsorbed on platinum single crystals have been most widely studied. This is because the system offers an opportunity to gain understanding that ultimately can

lead to the design of new catalysts and also for understanding the activity pattern of Pt metal nanoparticles employed in fuel cells in the size range of a few nanometers.

The first *in situ* determination of CO_{ad} structure was reported for a CO adlayer on Pt(111) in acidic electrolytes. Using *in situ* STM, Villegas and Weaver [53, 56] observed a hexagonal close-packed (2 x 2)-3CO adlayer structure at potentials below 0.25 V (vs. SCE), with a CO coverage of $\Theta_{CO} = 0.75$ ML. The z-corrugated pattern evident in STM images indicated the presence of adsorbed CO at two threefold hollow Pt sites and one atop Pt site per (2x2) unit cell. At potentials above 0 V (up to the onset of CO oxidation) a markedly different adlayer arrangement was formed, having a ($\sqrt{19}$x$\sqrt{19}$)R23.4°-13CO unit cell with $\Theta_{CO} = 13/19$. Following these earlier STM studies, direct information regarding the CO_{ad} structure was obtained in SXS measurements. While holding the potential at 0.05 V and with a continuous supply of CO to the x-ray cell, a diffraction pattern consistent with p(2x2) symmetry was observed [50, 57]. Once formed the structure was stable only when the CO was continuously supplied to the x-ray cell, i.e., when CO was replaced by nitrogen the p(2x2) structure slowly vanished. It is also worth mentioning that the potential range of stability of the p(2x2)-3CO phase was strongly affected by the oxidation of a *small* fraction (~15 %) of CO in the pre-ignition potential region. The potential window of stability as well as the domain size of this structure can be controlled by the nature of anions present in supporting electrolytes. For example, in one study the CO coherent domain size increased from KOH (ca. 30 Å), to $HClO_4$ (ca. 140 Å) to $HClO_4 + Br^-$ (ca. 350 Å) electrolytes. Given that the potential range of stability increased in the same order, it was suggested [58] that CO ordering at low overpotentials is determined by the competition between OH_{ad} and spectator anions for the defect/step

sites, *i.e.*, the less active the surface is towards CO oxidation the larger the ordered domains and the greater the potential range of stability of the p(2x2) structure.

Metal UPD corresponds to the electrochemical adsorption, often of one monolayer, that occurs at electrode potentials positive of the Nernst potential below which bulk metal adsorption occurs [59]. Numerous experiments have shown that the UPD layer can dramatically alter the chemical and electronic properties of the interface. The UPD layer is also the first stage of bulk metal deposition and its structure, therefore, can strongly influence the structure of the bulk deposit. UPD was the first process to be studied using synchrotron x-ray diffraction in the late 1980's [27]. Quite a few systems have now been studied using this technique and this has led to a greater understanding of the physics determining the structure of the UPD layer, in particular with regards to the role of the electrode potential and of various other adsorbing species that can be present in solution. In fact, considerable work was devoted to the co-adsorbate structures formed during UPD in the presence of halide anions and results for Pt(hkl) and Au(hkl) surfaces have recently been reviewed [33].

In determining the electrochemical reactivity of a surface towards a particular chemical reaction, it is clear that the electrode potential is integral in determining the relative coverage by anion and/or cation species. For example, the coverage by anion species is an important factor in determining the rate of the oxygen reduction reaction on transition metal surfaces [33]. It is also important, however, to remember that the electrochemical interface is in chemical equilibrium and that adsorption/desorption processes are determined by the energies of adsorption unless kinetic barriers are present. This latter effect was illustrated in recent studies of the adsorption and oxidation of CO on Pt(*hkl*) surfaces modified by UPD metals. In these studies RRDE and SXS measurements showed that UPD Cu and Pb are almost completely displaced

from the Pt(100) and Pt(111) surfaces in perchloric acid (free of halide anions) by CO [60-61]. Although these results are somewhat surprising and would not be observed in UHV studies, metal displacement can be understood from a simple thermodynamic analysis by calculating the Gibbs energy change (ΔG) for the component steps of the process [62]. These calculations predict the spontaneous displacement of Cu and Pb by CO from the Pt electrode due to the corresponding exothermicity of the overall ΔG.

A series of experiments are presented which consider both the structural and electrochemical processes which are occurring at the solid/liquid interface, and also some UHV-based x-ray measurements to highlight the sensitivity of this technique. Chapter 4 describes a series of experiments designed to probe ordered oxygen layers and water structures on Pt. Central to all electrochemical reactions in water-based electrolytes and, indeed, to a wide range of physical phenomena in nature, is the structure and bonding of water at a surface. The interaction of water with solid surfaces plays a crucial role in many areas of science. The water structure at well-defined metal surfaces is of particular importance in catalysis and electrochemistry, as the activation of water is the crucial step in many surface reactions. Despite this importance, at the electrified interface numerous experimental and theoretical studies have yet to provide a detailed picture of the atomic-scale structure of water and its behaviour remains poorly understood. Chapter 4 describes a series of x-ray scattering experiments designed to probe an ordered oxygen layer and an ordered water layer - both these experiments were performed using a Pt(111) single crystal sample as the substrate.

Metal surface reconstruction, in which the topmost atomic layer assumes an ordered structure that can differ from the underlying bulk phase of the crystal, is a topic that is

well studied in both UHV [21] and electrochemical surface science [7, 63]. In UHV, the surface reconstructions of Au are stable up to high temperatures, whereas in the electrochemical environment the state of the surface can be controlled by the electrode potential *via* the strong metal-adsorbate interaction and/or the electrode surface charge [64]. For the Au(111) surface, it is known that the reordering process required for surface reconstruction to the (px$\sqrt{3}$) phase does not require a great deal of mass transport (see detailed discussion above) as the compression is only 24/23, that is, 4.4%. This system is presented in Chapter 5 first, with the effects of potential and temperature being focused upon.

For Au (100), the reconstruction involves significant transport of surface Au atoms as the hexagonal reconstructed surface layer (on the underlying square bulk crystal lattice) has an atomic density that is ~20% greater than the (100) surface plane. Recent video-STM studies, in combination with previous STM results, have shown that the reconstruction proceeds by rapid nucleation of atom strings, at the adislands formed by the excess surface Au atoms, followed by agglomeration of the strings to form the long-range ordered hexagonal phase [65]. Au surface reconstructions, and the effects of temperature, will constitute Chapter 5 of this thesis.

In addition to the study of surface reconstruction, considerable attention has also been focused on the potential-induced structural changes of halide ions and CO adsorbed onto Au and Pt single crystal surfaces. For example, it has been found that, on both Au and Pt, adsorbed Br can form ordered structures which are critically dependent on the potential-controlled surface coverage by the Br^- ions [5, 41]. In the case of the potential-driven CO structure changes, the p(2x2)-3CO (Θ_{CO} = 0.75 ML) $\leftrightarrow$ ($\sqrt{19}$x$\sqrt{19}$)R23.4°-13CO (Θ_{CO} = 0.68 ML) structural transition has been studied in some detail by SXS [50, 57], as well as by many other experimental techniques [10,

53]. These studies have shown unambiguously that at an *ambient temperature* the driving force for the structural rearrangement is a small, yet clearly discernable, oxidative removal of CO in a Langmuir-Hinshelwood type reaction. The work on the CO/Pt(111) system will form Chapter 6 of this thesis.

Despite these advances, however, in practical applications the structural phenomena described above, as well as many other relevant electrochemical processes, occur at non-ambient temperatures and yet little is known about the effect of temperature on the atomic structure at the electrochemical interface. It is very difficult, however, to probe the effect of temperature on the electrode structure using STM due to a number of experimental constraints. In contrast, SXS is an ideal technique if the SXS electrochemical cell is modified to control the temperature of the electrolyte during the SXS measurements. In this thesis results that have been obtained in an electrochemical SXS cell that can operate over the range 275-325 K are presented. It is shown that, in contrast to UHV, a very small change in temperature had dramatic effects on the "hex" $\leftrightarrow$ (1x1) phase transition of Au(100) and the ordering and structural transitions of both spectator species (Br adlayers on Au(100) and Pt(111)), and also reactive species (CO adlayer on Pt(111)). The results for both Au and Pt indicate that the temperature-induced changes result primarily from the kinetically-driven diffusion of surface atoms/adsorbates with concomitant oxide formation. The results form a starting point for developing a wider understanding of temperature effects in structure-function relationships relevant to many electrochemical applications.

Chapter 2

Theoretical Principles

2.1 The Solid-Liquid Interface

The current model of the solid-liquid interface was developed over a long period of time, and can be traced back to the initial model proposed in 1853 by Helmholtz. This model assumes no faradaic processes occur at the interface, and that any surface charge density at the interface is counteracted by the resulting redistribution of solvated ions in the electrolyte. This results in electric neutrality across the interface. The model proposed that the minimum distance between a solvated ion and the electrode was defined by the solvation shell of the ion. From this, the Outer Helmholtz Plane (OHP) was devised, which is an imaginary plane drawn through the centre of the solvated ions at closest approach to the electrode. This results in a linear potential drop between the interface and the centre of the solvated ions. As this model depicts two planes of equal but opposite charge (*i.e.* the OHP and the electrode surface itself), it was termed the "electrical double layer".

The model was subsequently modified by Gouy and Chapman, who suggested a diffuse charged layer close to the electrode surface. This was attributed to two effects. Firstly, the electrostatic attraction/repulsion acting on the electrolyte ions would result in a diffuse layer. Secondly, the effects of Brownian motion are also conducive to a diffuse interpretation of the charge distribution. In 1924, Stern was responsible for

effectively merging the two previous models. Using point charges to represent the ions, he also proposed a linear potential drop between the electrode and the OHP, followed by a more gradual potential decrease into the bulk electrolyte. In 1947 Grahame proposed a revised model to account for ions which have lost all or part of their solvation shell. He realised that these ions could come into direct contact with the surface, allowing specific adsorption to occur. These "closest approach" ions create the Inner Helmholtz Plane (IHP). A schematic of the Grahame model can be seen in Figure 2.1.

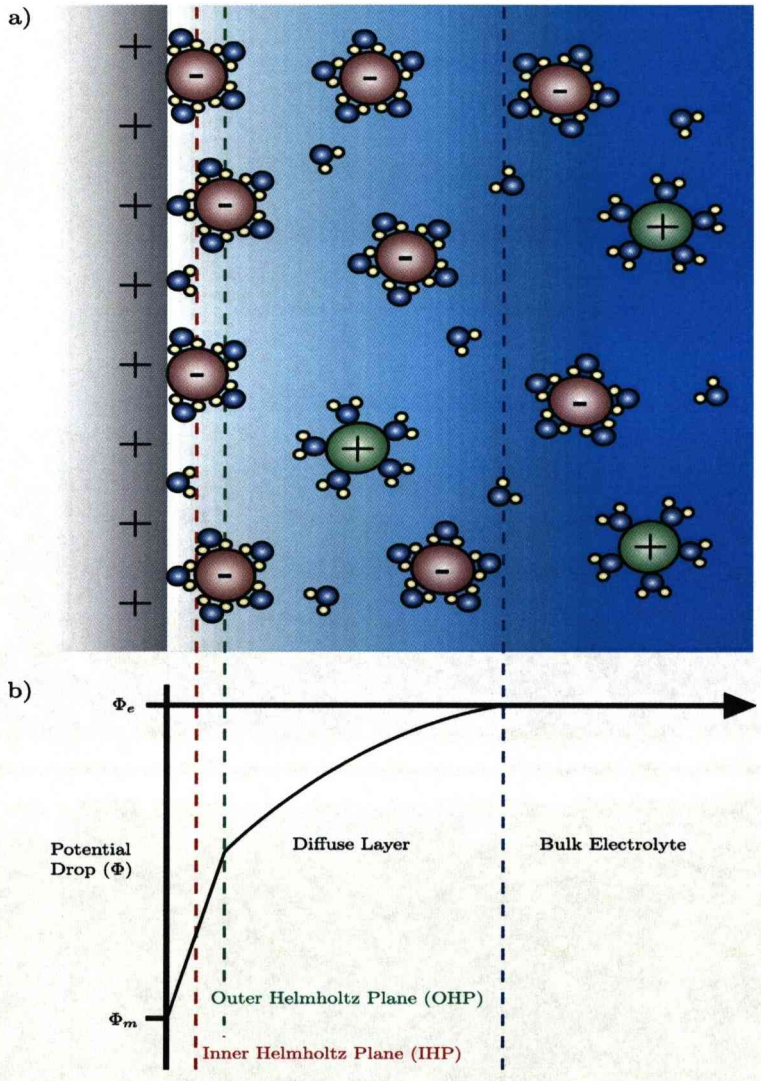

Figure 2.1: Schematic of (a) the Grahame model of the electrode/electrolyte interface, and (b) the potential drop across the interface.

2.2 Electrode Processes

This section gives a brief description of the theoretical considerations involved when performing potential dependent measurements, such as cyclic voltammetry (CV) and Rotating Ring Disk Electrode (RRDE) measurements. The interested reader is referred to references [66-69] for a more detailed description.

2.2.1 Electrode Potentials

The applied potential difference across the solid-liquid interface is one of the key variables in the experiments presented within this thesis, as it (largely) controls the current flow at the electrode-electrolyte interface. The measurement of this potential difference, and the manipulation of it, are thus of key importance. What follows is an explanation of the requirement for a three electrode system.

When measuring I-V response curves for electrochemical systems, it is imperative that the potential drop we measure/control is that at the working electrode, as this is the interface we are attempting to probe/study. Let us consider a working electrode immersed in electrolyte. To apply a potential at the working electrode (we) requires a second electrode, as the potential of this secondary electrode (sec) is effectively what determines the potential at the working electrode/electrolyte interface (*i.e.* potential is a relative quantity). The potential drop measured is now as follows:

$$\varphi = (\varphi_{we} - \varphi_{electrolyte}) - (\varphi_{sec} - \varphi_{electrolyte})$$

$$= \varphi_{we} - \varphi_{sec}$$

Thus it can be seen that, using a two electrode system, what is actually measured/applied is the potential difference between the two metal electrodes, and not that across the working electrode/electrolyte as required. This leads to the introduction of a third electrode, termed the reference electrode.

The key function of the reference electrode is to keep the potential drop between itself and the electrolyte constant. Experimentally, the current will pass between the working and secondary electrodes, but the potential is measured/applied across the working and reference electrodes (it is important to note that the reference electrode does require an extremely small current to flow through it to operate, but this must remain small to maintain a constant reference, *i.e.* not change the composition of the reference via oxidation/reduction processes). This means that the measured potential is as follows:

$$\varphi = (\varphi_{we} - \varphi_{electrolyte}) - \text{constant}$$

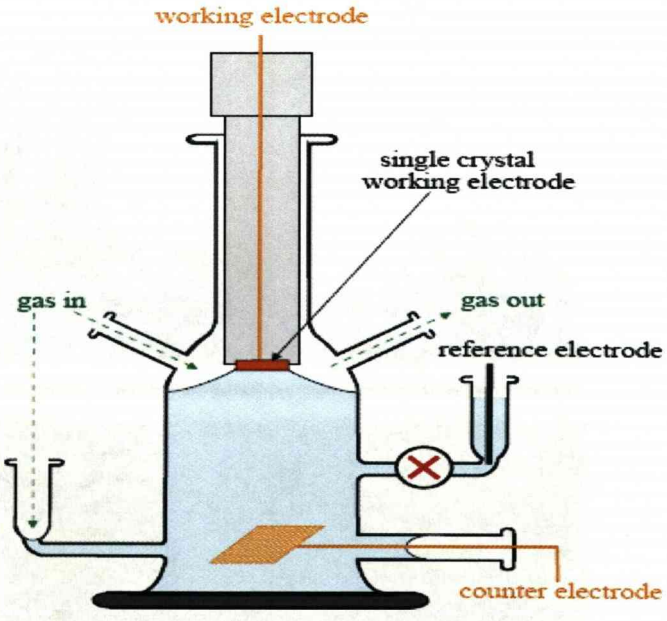

Fig 2.2.1: A typical three electrode system, as used for cyclic voltammetry (CV) measurements

As a result, we can apply a known potential difference across the electrode/electrolyte interface. The reason a two electrode system cannot be used is that the large currents passing cause oxidation/reduction effects at the secondary electrode. This means that the potential drop across the secondary/electrolyte interface is not constant. A schematic of a three electrode system is presented in Figure 2.2.1.

2.2.2 Cyclic Voltammetry

One of the simplest ways to study electrochemical systems is to perform cyclic voltammetry (CV) measurements, which provide information in the form of I-V response curves and are considered a fundamental technique to surface scientists [68]. Such I-V response curves are sensitive to numerous processes. These include electron transfer at the interface, adsorption/desorption of anions, and even changes in the ordering of adsorbate layers or surface atoms. A lack of sensitivity means that CV measurements are often used as a complementary technique, in conjunction with other techniques such as surface x-ray scattering (SXS) and scanning tunnelling microscopy (STM).

A typical schematic of a CV experiment was presented in Figure 2.2.1, showing an experiment performed in the hanging meniscus geometry. This reduces the electrical contact of the electrolyte with parts of the single crystal sample which are not oriented along the desired plane. Thus any measurements are more representative of the specific surface arrangement being studied. Inert Gas, such as argon or nitrogen, is used both to purge oxygen from the solution and to maintain an overpressure to avoid the solution becoming oxygenated. This is illustrated in Figure 2.2.1. Throughout the

work presented here, either saturated calomel reference electrodes (SCE) or silver/silver-chloride reference electrodes were used. However, all potentials are quoted with respect to the Normal Hydrogen Electrode (NHE), or the equivalent reversible hydrogen electrode (RHE).

A cyclic voltammogram is performed with a potentiostat, which sweeps the potential across the electrode/electrolyte interface in a linear fashion. It uses the three electrode system described previously, and is characterised in Figure 2.2.2(a) below.

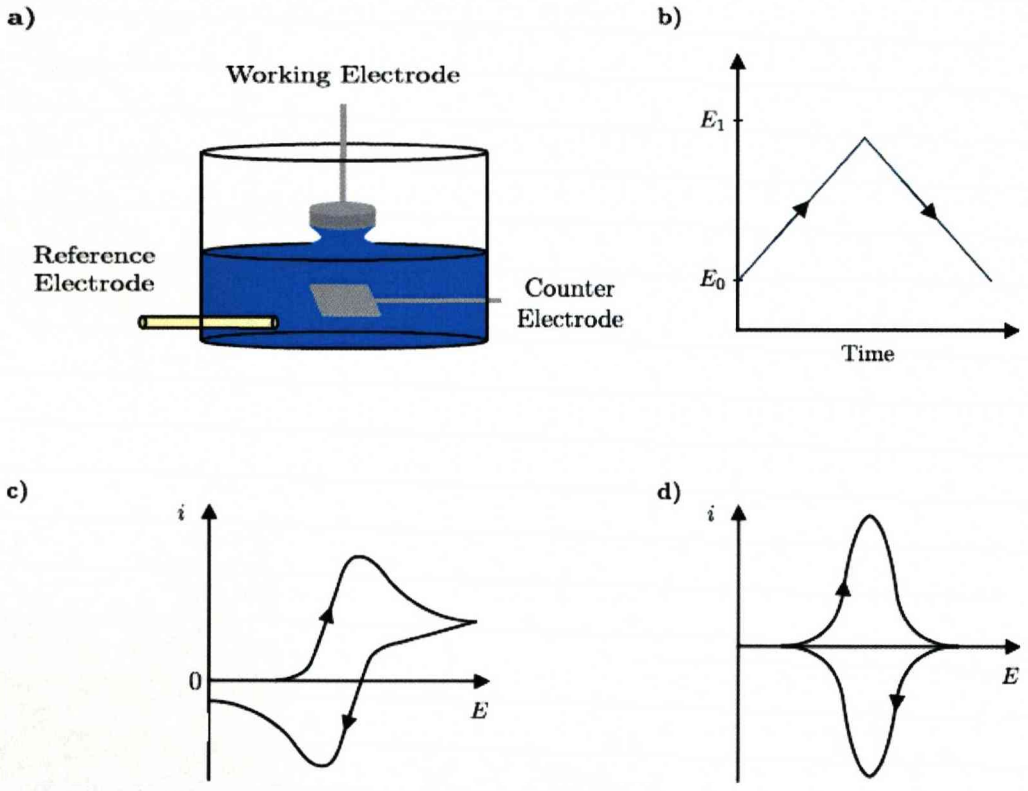

Figure 2.2.2: (a) Schematic of the hanging-meniscus orientation used in cyclic voltammetry (CV) experiments. (b) Typical applied potential employed during a CV experiment. (c) An example of a current-potential curve obtained from a solution phase single-electron transfer reaction. (d) An example of a cyclic voltammogram of a surface-adsorbed species.

Figure 2.2.2(b) shows the applied potential, and how it varies with time. Figure 2.2.2(c) shows the resulting current from a typical reversible one electron reaction.

Initially, the over-potential is too small to induce a reaction. As the over-potential increases, electron transfer takes place until a maximum current is obtained. At potentials greater than this, the current flow reduces as the concentration of charge carriers at the electrode weakens due to kinetic limitations within the diffuse layer of electrolyte, until a constant minimum level is reached.

For adsorption processes, we are considering the single electron reduction of electroactive species via the following mechanism:

$$A^{-}_{(aq)} \Leftrightarrow A_{(ad)} + e^{-}_{(m)} \tag{2.1}$$

At large positive potentials, the current reaches zero as the amount of electroactive substance is limited. Also, the oxidation/reduction peaks occur at the same potential (but opposite potential sweep directions) as the process is not diffusion-limited [66], but is instead governed by electron transfer kinetics. This is summarised in Figure 2.2.2(d) above.

2.2.3 The Rotating Disk Electrode (RDE)

The Rotating Ring Disk Electrode (RDE) has a distinct advantage over CV measurements, in that it is not a diffusion limited technique. A typical RDE experimental setup is similar in geometrical configuration to that illustrated for the CV technique (see Figure 2.2.2 above). The key difference is that the RDE technique involves rotating the working electrode at high speed. The resulting centrifugal force which acts on the electrolyte at the surface causes a laminar flow of solution, both

towards and across the surface [66, 70]. This means that, as solution from the bulk is readily supplied to the sample surface, any reactions that take place there are not diffusion limited. This technique has many uses and was used to probe the I-V response curve for all systems presented in this thesis. For all CV and RDE measurements presented, a large amount of credit and thanks must go to Dr. Dusan Strmcnik, Dr. Vojislav Stamenkovic, and Prof N. M. Markovic, from the Material Science Division, Argonne National Laboratory, USA.

2.3 X-Ray Diffraction

The following derivations closely follow references [71-73], and are intended to provide the reader with a description of the fundamental mathematics underpinning the practical techniques used throughout this thesis. For the experiments presented in the data Chapters, kinematical scattering theory was considered a suitable model for the scattering events taking place. The theory suggests that the x-ray/crystal interaction is weak. This implies that each photon is only scattered once (by the atomic electron) and thus multiple scattering events are not allowed. The model has limitations, for example it is better suited to surface scattering geometries as the photon passes through fewer atomic layers. Other factors are also important, such as sample scattering strength (atomic number) and crystalline perfection. However, for single crystal samples in thin layer geometry electrochemical cells, it has been shown that the kinematical approach is a good approximation.

2.3.1 Scattering from a single electron

To fully describe X-ray scattering, we must start by considering the scattering from a single electron. From this we can combine the scattering from multiple electrons to describe that from a given atom, and then combine the scattering from individual atoms to build up the scattering from a given atomic plane. Finally, we can consider the summation of scattering events from all atomic planes to fully define the scattering from a given sample. To do this, Figure 2.3.1 illustrates the relative position vectors for a *unit cell* within a sample, an atom within the unit cell, and an electron within the atom (a unit cell is a 3D atomic arrangement which can be used to map out fully the whole sample by simple translations).

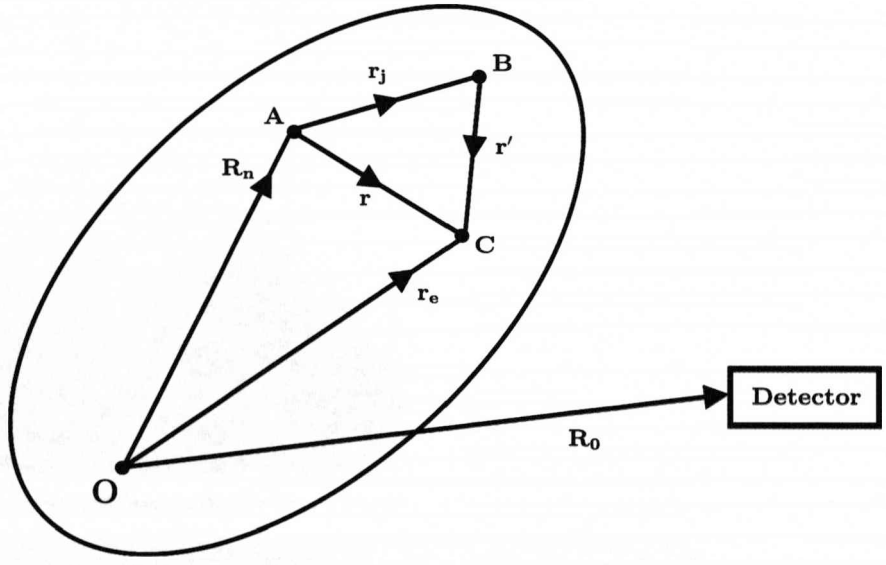

Figure 2.3.1: Definition of the vectors used during the derivation of kinematical x-ray scattering theory. Point O is the origin of the crystal, point A is the origin of the nth unit cell, point B is the jth atom of the nth unit cell and point C is the location of an electron belonging to the atom at point B. Reproduced from Reference [71].

Incoming (polarized) x-rays have an associated electric field, which causes electrons to oscillate and emit spherical radiation of identical wavelength. The amplitude of a

wave A_1 emitted by an electron at $\mathbf{r_e}$ is related to the incoming plane polarized x-ray wave amplitude, A_0, by the Thompson formula,

$$A_1 e^{-i(k_f \cdot r_e)} = A_0 \frac{e^2}{4\pi\varepsilon_0 mc^2} \frac{1}{R_0} e^{-i(k_i \cdot r_e)} \tag{2.2}$$

whereby the R_0 term arises due to the spherical nature of the resulting wave. The electron mass and charge are denoted *e* and *m* respectively. The speed of light is denoted as c, and k_i/k_r denotes the incoming/outgoing reciprocal wave-vector respectively (see Figure 2.3.2 below).

2.3.2 Momentum Transfer

When an incoming wave interacts with a sample, it is useful to define the momentum transfer, $\mathbf{q} = \mathbf{k_f} - \mathbf{k_i}$, which is simply the difference between the outgoing and incoming reciprocal wave-vectors (Figure 2.3.2 below). For elastic scattering events where no energy is absorbed, $|\mathbf{k_i}| = |\mathbf{k_f}| = |\mathbf{k}| = 2\pi/\lambda$, where λ is the wavelength of the incoming radiation.

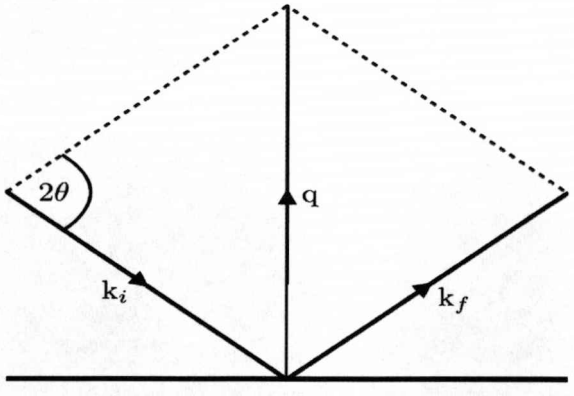

Figure 2.3.2: Momentum transfer **q**, illustrated using the reciprocal wave-vectors $\mathbf{k_f}$ and $\mathbf{k_i}$.

Combined with some simple trigonometry, this leads us to the following definition of Bragg's law,

$$|\mathbf{q}| = 2|\mathbf{k}|\sin\left(\frac{2\theta}{2}\right) = \frac{4\pi}{\lambda}\sin\left(\frac{2\theta}{2}\right) \tag{2.3}$$

therefore, Equation 2.3 can be rearranged using

$$e^{i(\mathbf{q}\cdot\mathbf{r_e})} = \frac{e^{-i(\mathbf{k_i}\cdot\mathbf{r_e})}}{e^{-i(\mathbf{k_f}\cdot\mathbf{r_e})}} \tag{2.4}$$

resulting in,

$$A_1 = A_0 \frac{r_0}{R_0} e^{i(\mathbf{q}\cdot\mathbf{r_e})} \tag{2.5}$$

where

$$r_0 = \frac{e^2}{4\pi\varepsilon_0 mc^2} \tag{2.6}$$

The last expression is known as the Thomson scattering length. It comes from classical electrostatic models which take an electron to be a spherical mass with constant charge density on the surface. This scattering length can then be equated to the relativistic energy of the electron.

2.3.3 Scattering from an Atom

The scattering amplitude of an atom, A_2, is the summation of the scattering amplitudes from each individual electron. Classically each electron has an associated density distribution at $\mathbf{r}'$ denoted $\rho(\mathbf{r}')$. The summation therefore becomes an integral, and replacing $\mathbf{r_e}$ with $\mathbf{R_n} + \mathbf{r_j} + \mathbf{r}'$, it becomes

$$A_2 = A_0 \frac{r_0}{R_0} \int_{-\infty}^{+\infty} \rho(\mathbf{r}') \mathbf{e}^{\mathbf{iq}\cdot(\mathbf{R_n}+\mathbf{r_j}+\mathbf{r}')} \mathrm{d}^3\mathbf{r}'$$

$$= A_0 \frac{r_0}{R_0} f(\mathbf{q}) e^{i\mathbf{q}\cdot(\mathbf{R_n}+\mathbf{r_j})} \tag{2.7}$$

Where f(**q**) is known as the atomic form factor,

$$f(\mathbf{q}) = \int_{-\infty}^{+\infty} \rho(\mathbf{r}') \mathbf{e}^{\mathbf{iq}\cdot\mathbf{r}'} \mathrm{d}^3\mathbf{r}' \tag{2.8}$$

When the incoming x-ray differs from the energy required to excite atomic electrons, the atomic form factor is essentially q dependent. However, if the x-ray energy is close to the energy difference between two orbital energy levels, so to induce atomic transitions, the form factor requires further energy-dependent terms. This is known as the dispersion correction and is as follows

$$f(\mathbf{q},E) = f(\mathbf{q}) + f'(E) + if''(E) \tag{2.9}$$

where $f(\mathbf{q},E)$ is the corrected form factor, $f(\mathbf{q})$ is the uncorrected form factor, and $f'(E)$ and $if''(E)$ are the real and imaginary terms of the dispersion correction. The International tables of Crystallography [74] contain a list of uncorrected form factors for the various elements, and dispersion correction programmes (Fortran based) are available from the SSRL [75].

2.3.4 Scattering from a Unit Cell

The next step is to calculate the scattering due to one unit cell of a crystal, A_3. A unit cell is significant in that it constitutes a basic "building block" from which the entire crystal can be constructed using simple translations. This simplifies the mathematics greatly. Atoms contained within the unit cell are not necessarily of the same chemical element therefore a separate form factor must be assigned to each atom. For a unit cell of N_c atoms, the scattering amplitude is given by

$$\begin{aligned} A_3 &= A_0 \frac{r_0}{R_0} \sum_{j=1}^{N_c} f_j(\mathbf{q}) \mathbf{e}^{\mathbf{iq}\cdot(\mathbf{R_n}+\mathbf{r_j})} \\ &= A_0 \frac{r_0}{R_0} F(\mathbf{q}) e^{(i\mathbf{q}\cdot\mathbf{R_n})} \end{aligned} \tag{2.10}$$

Where F(**q**) is called the structure factor

$$F(\mathbf{q}) = \sum_{j=1}^{N_c} f_j(\mathbf{q}) e^{i(\mathbf{q}\cdot\mathbf{r}_j)} \tag{2.11}$$

and is dependent on **q**, and on the geometric arrangement of atoms within the unit cell also. This equation describes mathematically how crystalline solids interact with electromagnetic radiation.

2.3.5 Diffraction from a Crystal

To account for scattering from the entire crystal, A_4, we must sum the scattering amplitudes arising from each unit cell. We define our crystal to be of N_1, N_2 and N_3 unit cells, corresponding to the associated axis directions, $\boldsymbol{a}_1$, $\boldsymbol{a}_2$ and $\boldsymbol{a}_3$. The origin of each unit cell can therefore is thus

$$\boldsymbol{R}_n = n_1\boldsymbol{a}_1 + n_2\boldsymbol{a}_2 + n_3\boldsymbol{a}_3 \tag{2.12}$$

where n_1, n_2, and n_3 are integer values. This gives the scattering amplitude as

$$A_4 = A_0 \frac{r_0}{R_0} F(\mathbf{q}) \sum_{n_1=0}^{N_1-1} \sum_{n_2=0}^{N_2-1} \sum_{n_3=0}^{N_3-1} e^{i(\mathbf{q}\cdot(n_1\mathbf{a}_1 + n_2\mathbf{a}_2 + n_3\mathbf{a}_3))} \tag{2.13}$$

The above equation has two parts; the structure factor which is determined by the elemental properties of the material(s), and the remainder which is simple a geometric

sum. We shall now consider Equation 2.13 more closely. What we have is a geometric progression for a one dimensional crystal of *N* atoms, where x = **q.a**, such that

$$S_N(x) = \sum_{n=0}^{N-1} e^{ixN} \tag{2.14}$$

$$= \frac{1 - e^{ixN}}{1 - e^{ix}}$$

$$= \frac{e^{ixN/2}(e^{-ixN/2} - e^{ixN/2})}{e^{ix/2}(e^{-ix/2} - e^{ix/2})} \tag{2.15}$$

The intensity of the scattered beam is always the experimental variable, as opposed to the amplitude. The square modulus of S is proportional to the scattered intensity and, using $e^{i\theta} = \cos\theta + i\sin\theta$,

$$|S_N(x)|^2 = \frac{\sin^2(xN/2)}{\sin^2(x/2)} \tag{2.16}$$

The above equation is prominent in the field of optics, and is known as the N-slit interference function. It shows that the primary maxima within the scattered signal are spaced 2π apart in units of **q.a** and are of magnitude N^2. Extending this to three-dimensions, *i.e.* analogous to a large 3D crystal, we find the diffracted amplitude, A_4, can now be written as a product of slit functions

$$A_4 = A_0 \frac{r_0}{R_0} F(\mathbf{q}) S_{N_1}(\mathbf{q}\cdot\mathbf{a}_1) S_{N_2}(\mathbf{q}\cdot\mathbf{a}_2) S_{N_3}(\mathbf{q}\cdot\mathbf{a}_3) \tag{2.17}$$

The diffracted intensity is thus a product of three periodic δ functions along well-defined crystallographic directions. This leads to the concept of a reciprocal lattice, whereby diffraction only occurs when the Laue conditions for diffraction are met. That is, when

$$\begin{aligned} \mathbf{q}\cdot\mathbf{a}_1 &= 2\pi h \\ \mathbf{q}\cdot\mathbf{a}_2 &= 2\pi k \\ \mathbf{q}\cdot\mathbf{a}_3 &= 2\pi l \end{aligned} \tag{2.18}$$

h, k and l are called the Miller indices and take integer values. The Laue conditions can be satisfied simultaneously by the vector

$$\mathbf{q} = h\mathbf{b}_1 + k\mathbf{b}_2 + l\mathbf{b}_3 \tag{2.19}$$

where

$$\begin{aligned} \mathbf{b}_1 &= 2\pi \frac{\mathbf{a}_2 \times \mathbf{a}_3}{\mathbf{a}_1 \cdot (\mathbf{a}_2 \times \mathbf{a}_3)} \\ \mathbf{b}_2 &= 2\pi \frac{\mathbf{a}_3 \times \mathbf{a}_1}{\mathbf{a}_1 \cdot (\mathbf{a}_2 \times \mathbf{a}_3)} \\ \mathbf{b}_3 &= 2\pi \frac{\mathbf{a}_1 \times \mathbf{a}_2}{\mathbf{a}_1 \cdot (\mathbf{a}_2 \times \mathbf{a}_3)} \end{aligned} \tag{2.20}$$

We are now able to describe scattering in three dimensions in terms of h, k and l, and more usefully **q**. The vectors $\mathbf{b}_1$, $\mathbf{b}_2$ and $\mathbf{b}_3$ are orthogonal to the real space lattice vectors $\mathbf{a}_1$, $\mathbf{a}_2$ and $\mathbf{a}_3$ and produce a lattice of allowed scattering, the reciprocal lattice;

therefore the diffracted intensity is zero at positions which are not defined by these integer reciprocal lattice positions. This is not experimentally true however; as the derivations presented are based on infinite crystallographic arrays *i.e.* not finite samples as used for experimentation (see next section). The real space vectors are measured in Å, which means that the reciprocal lattice has the inverse unit, *i.e.* $Å^{-1}$. The diffracted intensity can now be written as a function of **q**, and for a particular set of h, k and l values is given by

$$|I_{hkl}|=|A_0\frac{r_0}{R_0}f(h\mathbf{b}_1+k\mathbf{b}_2+l\mathbf{b}_3)N_1N_2N_3|^2 \qquad (2.21)$$

2.3.6 Crystal Truncation Rods

We will now look in detail at the effects on the reciprocal lattice of using a sample with finite dimensions. We will start by defining the crystal lattice vectors, such that, $\mathbf{a_1}$ and $\mathbf{a_2}$ lie in the surface plane of the crystal, and $\mathbf{a_3}$ is along the surface normal direction. By considering a 2D monolayer, we find that, along the surface normal direction, Equation 2.17 becomes independent of momentum transfer as $N_3 = 1$. This results in rods of scattering along the surface normal direction in reciprocal space, and is represented in Figure 2.3.6.1(a) below. Figure 2.3.6.1(b) shows the scattered intensity from a bulk crystal and a 2D-monolayer case. This illustrates that the Bragg rods, which are due to the 2D monolayer, pass through the Bragg points, which originate from the 3D bulk sample. A smooth intensity profile is observed between the Bragg peaks. This is because each layer contributes to the scattering. These scattering patterns (Figure 2.3.6.1(c)) are labelled crystal truncation rods (CTRs).

Equation 2.16 is utilised when calculating the scattering intensity. The numerator, $\sin^2(N_3\mathbf{q}\cdot\mathbf{a}_3/2)$, is a rapidly varying function of $\mathbf{q}$ (for large N) which becomes smeared out in a real experiment due to resolution effects and is suitably approximated to its average value of 1/2. Replacing this term into Equation 2.17 gives

$$I_{CTR} = |A_0 \frac{r_0}{R_0} F(\mathbf{q}) N_1 N_2|^2 \frac{1}{2\sin^2(\mathbf{q}\cdot\mathbf{a}_3/2)} \tag{2.22}$$

This concludes the derivation for the expected scattering intensity from CTR measurements resulting from a perfectly terminated and defect-free single crystal.

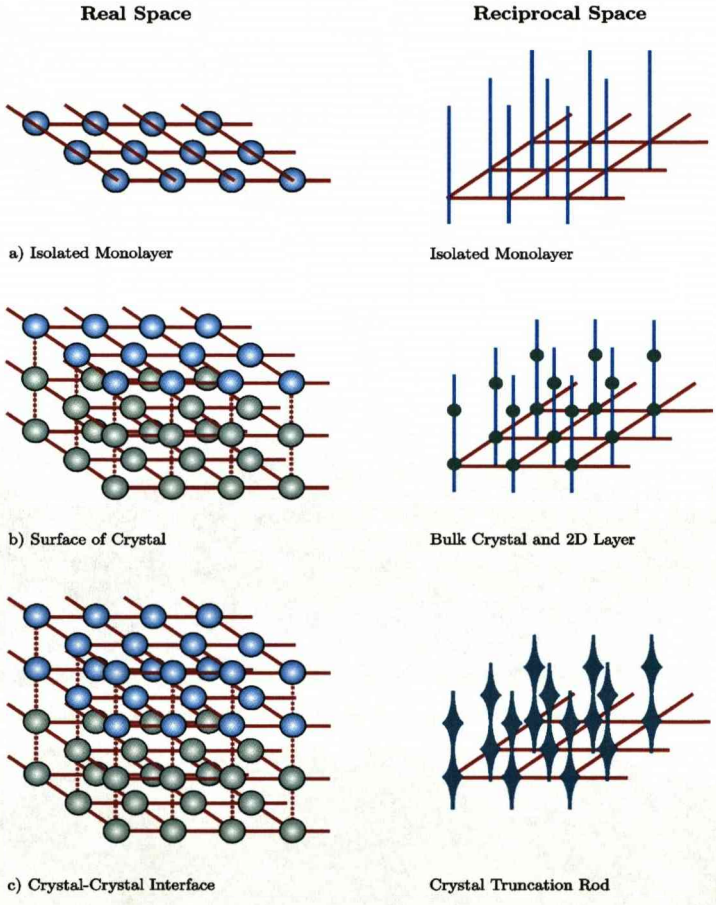

Figure 2.3.6.1: Real space representations and corresponding reciprocal space models (a) of an isolated monolayer, (b) surface of a crystal, (c) and a crystal-crystal interface.

However, many samples exhibit occupation and expansion effects of surface atomic layers. From Equation 2.22, we can see that the intensity maxima are situated at positions in l for which the Laue conditions are met. The intensity minima are found directly between the maxima, at half-integer l values known as anti-Bragg positions. These positions are analogous to scattering from a monolayer as scattering from the bulk layers cancels out. The black line in Figure 2.3.6.2 (a) shows the scattering intensity profile of a perfectly terminated crystal. The red line illustrates the calculation for the identical crystal, but with a 70% occupation of the surface atomic layer. The most apparent difference is the decrease in the intensity profile of the partially-occupied surface at the anti-Bragg positions. This clearly demonstrates the sensitivity of this position to surface occupation. In much the same way, Figure 2.3.6.2(b) shows the effect of surface-layer expansion on the CTR intensity profile. Again, the black line is a calculation of a perfectly-terminated single crystal, and the green line is a calculation of a single crystal with a surface atomic-layer expansion of 5%. In this case, the profile of the expanded surface exhibits asymmetry about the Bragg peaks. The l positions which exhibit the greatest difference in the intensity profile have been termed expansion positions as they are most sensitive to surface expansion. We shall now discuss in-plane momentum transfer, which deals with scattering events which include momentum transfer into the surface plane. This is vital for detecting phenomena such as surface reconstructions, whereby the arrangement of atoms in the surface layer(s) differs from the bulk arrangement. In providing both specular and non specular (in-plane) measurements, CTRs provide a valuable tool for the structural characterisation of various systems, including crystal surfaces and also deposited/adsorbed surface structures.

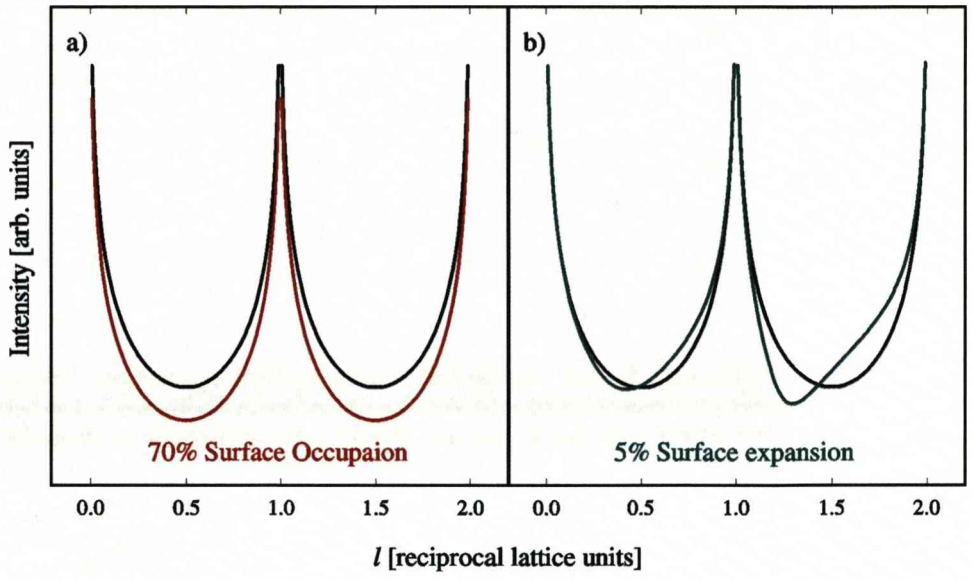

Figure 2.3.6.2: The profile from a perfectly-terminated single crystal, black line, (a) a surface-layer occupation of 70%, red line, and (b) a surface-layer expansion of 5%, green line.

.We shall now discuss in-plane momentum transfer, which deals with scattering events which include momentum transfer into the surface plane. This is vital for detecting phenomena such as surface reconstructions, whereby the arrangement of atoms in the surface layer(s) differs from the bulk arrangement. In providing both specular and non specular (in-plane) measurements, CTRs provide a valuable tool for the structural characterisation of various systems, including crystal surfaces and also deposited/adsorbed surface structures.

2.3.7 The Reciprocal Lattice

During surface x-ray scattering experiments the Miller indices are defined such that h and k lie in the surface plane. This constrains the specular CTR to be along the surface-normal direction. The results discussed in this thesis involve (100) and (111) orientated face centred cubic (fcc) metals. This section will provide a description of

the real-space parameters, the resultant reciprocal-space lattices, and the surface parameters used in subsequent modelling.

2.4 The fcc(100) Surface

The fcc(100) surface is presented in Figure 2.4.1, showing its unit cell from above (a), and also showing the side view (b); the corresponding reciprocal-space map is shown in Figure 2.4.1(c), where the solid-circles denote Bragg reflections and the black-lines represent the CTRs.

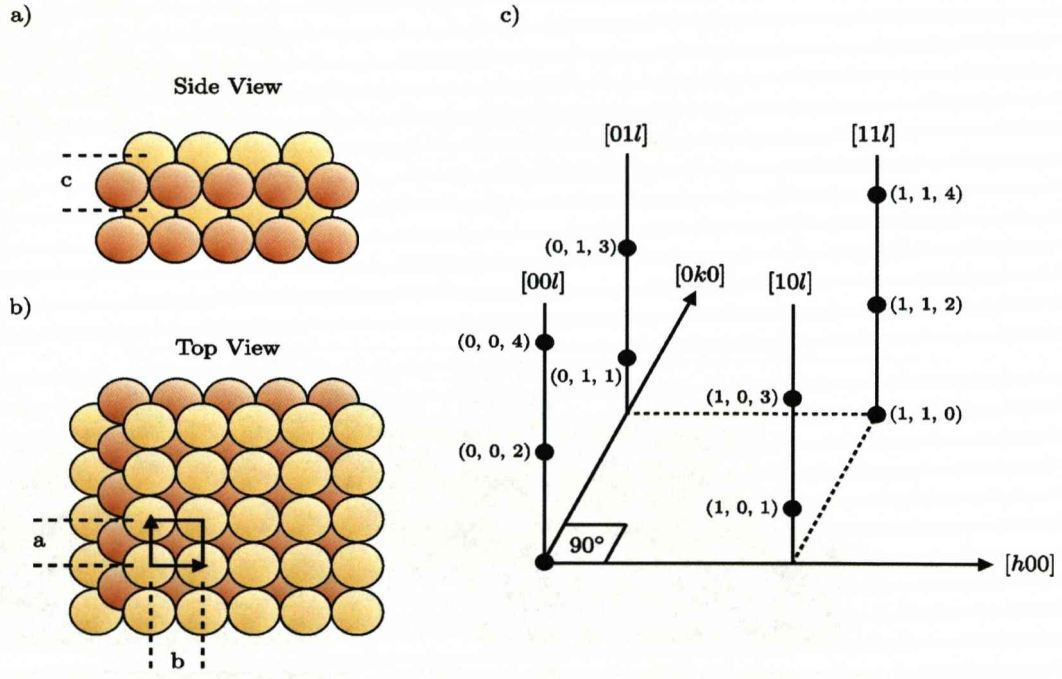

Figure 2.4.1: Schematic real-space model of the fcc(100) surface as viewed from (a) the side, and (b) above. (c) Corresponding reciprocal space model showing the Bragg reflections (solid circles) and CTRs (vertical black lines).

The surface tetragonal unit cell can be related to the cubic unit cell using the following translations

$$h_c = h_t + k_t$$

$$k_c = h_t - k_t$$

$$l_c = l_t$$

The surface units of h, k and l are

$$a^* = b^* = \frac{2\pi}{a_{NN}}$$
$$c^* = \frac{4\pi}{\sqrt{2}\,a_{NN}} \qquad (2.23)$$

where $\mathbf{a}_{NN}$ is the nearest-neighbour distance. The phase difference between successive atomic layers is expressed as, $e^{2\pi i(h/2+k/2+l/2)}$, and from this the bulk structure factor becomes

$$F_{Bulk} = fDW_{Bulk} \sum_{n=0}^{-\infty} e^{in[2\pi\left(\frac{h}{2}+\frac{k}{2}+\frac{l}{2}\right)]}$$

$$= \frac{fDW_{Bulk}}{1 - e^{-\pi i(h+k+l)}} \qquad (2.24)$$

where DW_{Bulk} is called the bulk Debye-Waller factor – this accounts for the thermal disorder of bulk atoms. It is determined from the root-mean-squared displacement of atoms about their average atomic positions, σ. These values have been calculated for

all elements and can be found in Reference [74]. The bulk Debye-Waller factor is related to σ

$$DW_{Bulk} = e^{-\frac{1}{2}(\mathbf{q}\sigma)^2} \tag{2.25}$$

To establish a real structural model, the three outermost atomic layers are summed as a continuation of the bulk scattering described by Equation 2.24

$$F_{Surf} = f\theta_n DW_n e^{2\pi i\left[n\left(\frac{h}{2}+\frac{k}{2}+l\left(\frac{1}{2}+\varepsilon_n\right)\right)\right]} \tag{2.26}$$

(for integer n values), where the structural variables are the fractional occupation, θ_n, the static enhanced Debye-Waller factor, DW_n, and expansion of the surface along the surface normal direction, ε_n. In this model, each parameter is considered independently for each of the three surface atomic layers. The total structure factor is found by adding the bulk structure factor, F_{Bulk}, and surface structure factor, F_{Surf}, and hence the total scattered intensity is

$$I_{tot} = |F_{tot}|^2 = |F_{Bulk} + F_{Surf}|^2 \tag{2.27}$$

2.5 The fcc(111) Surface

As with the fcc(100) surface, the fcc(111) surface is defined such that the surface normal direction is along the (0, 0, l) hex direction, and the (h, 0, 0) hex and (0, k, 0) hex directions lie in the surface plane, but subtend 60° (and not 90°). Figure 2.5.1 is a

schematic real-space model and unit cell of an fcc(111) crystal, as viewed from above (a) and the side (b). The corresponding reciprocal-space map is shown in (c),

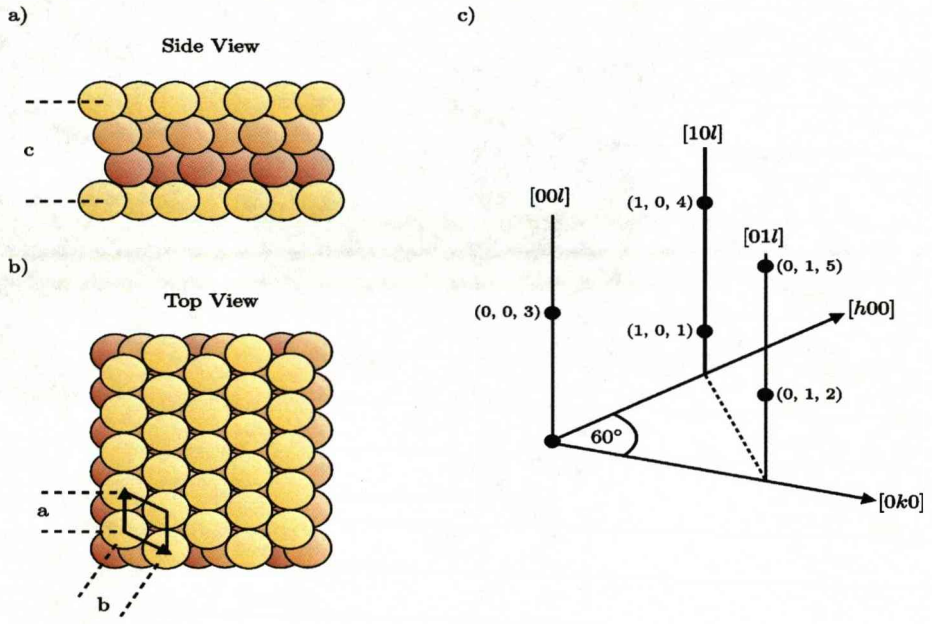

Figure 2.5.1: Schematic real-space model of the fcc(111) surface as viewed from (a) the side, and (b) above. (c) Corresponding reciprocal space model showing the Bragg reflections (solid circles) and CTRs (vertical black lines)

where the solid circles show Bragg reflections and the vertical lines represent the CTRs. The hexagonal unit cell and the conventional cubic unit cell are linked as follows

$$h_c = \frac{2}{3}h_s - \frac{2}{3}k_s + \frac{1}{3}l_s$$

$$k_c = \frac{2}{3}h_s + \frac{4}{3}k_s + \frac{1}{3}l_s$$

$$l_c = -\frac{4}{3}h_s - \frac{2}{3}k_s + \frac{1}{3}l_s$$

The units for h, k and l are

$$a^* = b^* = \frac{4\pi}{\sqrt{3}a_{NN}}$$
$$c^* = \frac{2\pi}{\sqrt{6}a_{NN}} \tag{2.28}$$

Analogous to the fcc(100) surface, the phase difference between consecutive atomic layers is given by, $e^{2\pi i(-h/3+k/3+l/3)}$, which gives the Bulk structure factor as

$$F_{Bulk} = fDW_{Bulk}\sum_{n=0}^{-\infty} e^{in[2\pi\left(-\frac{h}{3}+\frac{k}{3}+\frac{l}{3}\right)]}$$

$$= \frac{fDW_{Bulk}}{1-e^{2\pi i\left(\frac{h}{3}-\frac{k}{3}-\frac{l}{3}\right)}} \tag{2.29}$$

the structure factor from the three outermost surface layers is therefore

$$F_{Surf} = f\theta_n DW_n e^{2\pi i\left[n\left(-\frac{h}{3}+\frac{k}{3}+l\left(\frac{1}{3}+\varepsilon_n\right)\right)\right]}$$

(2.30)

for integer n values. The definitions of DW_n, θ_n, DW_n and ε_n are unchanged from the previous explanation.

Chapter 3

Experimental Methods

3.1 Single Crystal Sample Preparation

To probe the low index faces of single crystal samples experimentally requires a systematic procedure to ensure the surface quality. It is vital that all possible measures are taken to ensure the sample surface is free from unwanted contaminants, and providing the required atomic arrangement. For the x-ray measurements, samples (both Au and Pt) are typically cylindrical disks with a 10 mm diameter face, and are 3 mm in depth (although this is approximate). They were sourced from the Surface Preparation Lab, a company in Holland, and are said to be 99.9+ % pure with a miscut of <0.1 deg. For some of the Pt electrochemical measurements, a smaller sample (a cylinder of greater depth but of smaller diameter) was used for ease of preparation. Mechanical polishing is the first stage of the preparation process, whereby diamond paste and lubricating fluid are used to provide an optically good surface. After polishing, the sample is washed in ultra pure water and placed in an ultrasonic bath to remove any excess paste/impurities. This process is repeated, each polishing stage using a less coarse paste than the previous, until a final polish/rinse cycle with 0.1 mm paste is performed. The sample is then optically good, but the top 10 mm of the surface is atomically disturbed. The sample then undergoes UHV preparation, which involves numerous cycles of ion sputtering followed by annealing. The UHV prep of

the Au samples was heat to around 600 degrees C for a few hours, then ion beam for another hour and repeat this cycle for a few days. We used a resistive heater to get the sample hot for the Au samples. Cleanliness was checked with auger electron spectroscopy (AES) and surface structure with low energy electron diffraction (LEED). For the Pt samples, we used an electron beam heater to heat the sample to nearly 1000 deg C. The sample was ion beamed and annealed repeatedly, and checked for cleanliness and structure using AES and LEED. Solutions were made from pyrolitically triply distilled water (using chemicals purchased from Aldrich, 99.99% purity) and purged with Ar: Bay Gas Research Purity (or research grade nitrogen). Before sample preparation, the electrochemical/x-ray equipment (used in the experiments described in Chapters 5 and 6) would be bathed in a 50:50 mixture of concentrated nitric/sulphuric acid overnight, followed by repeated cycles of boiling and rinsing in Milli-Q water. Also, all metal contacts were checked for electrical soundness before experiments. The counter and working electrodes were flame annealed to remove impurities. This cleaning procedure was then repeated directly before the electrochemical/x-ray cell was constructed. For gold samples, a butane flame was used to heat the sample. The platinum samples were annealed in a hydrogen flame, and cooled in a hydrogen atmosphere to prevent oxidation of the sample. After cooling, all samples were protected by a drop of ultra pure water to prevent contamination, before transfer to the electrochemical cell. For experiments performed at the Advanced Photon Source, the samples were annealed by placing them between metal coils, which are then heated by applying RF waves (thus not a naked flame). This provides a more systematic method for the heating stage of this process – the other aspects are identical to the naked flame method described above.

For the platinum-based experiments in Chapter 4, the sample was transferred to the diffractometer under UHV conditions using a portable UHV chamber. Figure 3.1.1 shows the electrochemical cell schematically and the portable UHV chamber (called TRECXI) in operation. Whilst Pt itself will not oxidize, the stability of oxygen adsorbed on the (111) surface (relevant to the experiment in Chapter 4), will be affected by aggressive reactants in air. Therefore, UHV conditions are desirable for such an experiment. The TRECXI chamber allows incident/exit angles of up to 45 degrees through a beryllium window, and maintains vacuum via portable UHV (ion) pumps. Electrolyte is passed along a glass rod to achieve contact with the sample, and a 0.1 mm Pt wire is used as a counter electrode. The reference electrode used is a commercial Ag/AgCl microelectrode. The glass rod is manually positioned directly above the sample and then fixed to the chamber wall with screws. An endoscope (Everest VIT, rigid boroscope including a video camera) allows the user to move the rod to the desired position. A visual inspection is performed to ensure that air is not leaking into/out of the inlet/outlet capillaries. The droplet is controlled by a set of computer controlled syringe pumps (PSD3 syringe pumps, Hamilton Company) connected to the inlet and outlet PFA-PTFE tubes. This allows fresh electrolyte to be supplied to the sample. These pumps also allow the droplet size to be maintained regardless of evaporation effects.

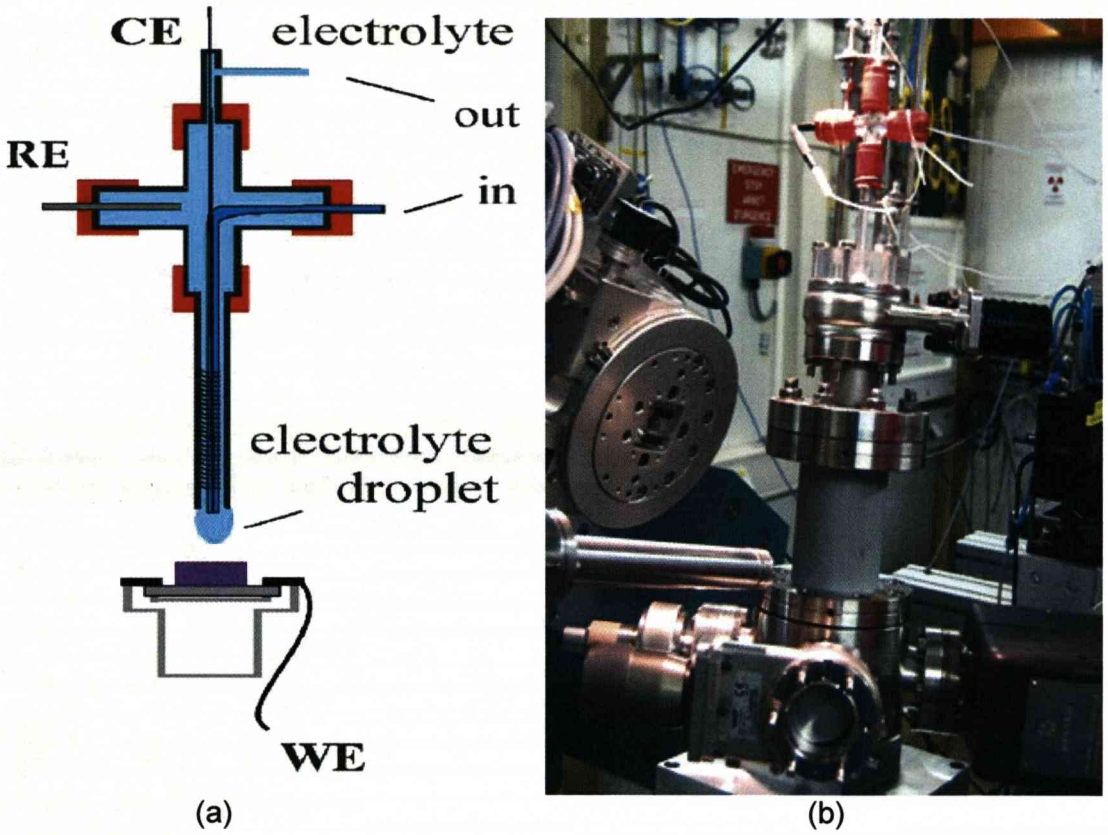

Fig 3.1.1: (a), showing a schematic of the glass cross contained inside of the portable UHV chamber (called TRECXI), and (b), showing the TREXCI chamber mounted on the diffractometer. Photograph taken from reference [76].

The sample was transferred to the TRECXI chamber, connected with a CF38 UHV valve to a docking port of the main UHV chamber. This is then detached from the main chamber and mounted onto the diffractometer. More information on the UHV transfer system (TREXCI) can be found in reference [76].

3.2 The X-ray cell

To probe the temperature effects on the systems presented in Chapters 5 and 6, the X-ray cell, as shown in Figure 3.2.1, was used. The sample was transferred into the cell

using Teflon wrapped forceps, and then placed into the sample holder. This was then tightened into place. Beforehand, all the electrical connections would be tested. When in place the sample is also checked for electrical connection. Finally, the cell would be sealed with a polypropylene film which is held in place by a rubber 'O-ring'.

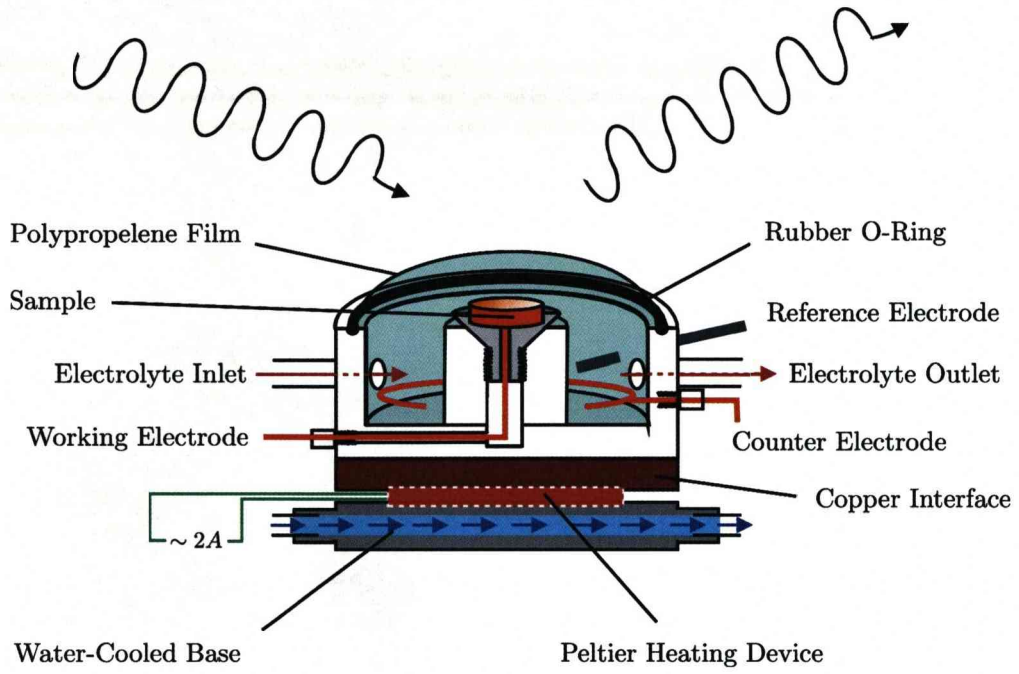

Figure 3.2.1: A schematic of the temperature X-ray cell.

Electrolyte enters the cell from the inlet tap, which comes from a reservoir of electrolyte which has been purged so as to remove oxygen. The cell is surrounded by a Mylar hood, which allows the cell to be kept in an inert atmosphere such as nitrogen. The permeable polypropylene film allows the introduction of gas into the system – a slight overpressure is all that is required for the diffusion of CO into the cell. The x-ray cell is a Macor ceramic construction, which sits on a peltier heating device. This material is chosen as it conducts heat well but is chemically inactive. The

secondary electrode (a polycrystalline Pt wire, 99.9% purity) curves around the base of the cell to provide an even electric field distribution to the sample. To control the temperature, a thermocouple is attached to the cell wall. The current polarity through the peltier determines whether the system is to be heated or cooled – typically achievable temperatures are 0-60 °C. Any higher temperatures usually result in problems with the polypropylene film splitting.

The cell has two modes of operation, one with the film inflated (film up), the other with it deflated (film down). The film is inflated when CV type measurements are required – here the system effectively behaves as a typical electrochemical cell. By comparison with established laboratory measurements, this provides a measure of the system cleanliness and potential induced behaviour. When the film is deflated a thin layer of electrolyte (~10μm, inferred from analysis of data) is trapped on the surface. This thin layer still allows us to manipulate the surface potential, but is thin enough to allow x-rays to pass through without absorption problems.

3.3 X-ray Beam-line configuration

All X-ray based measurements presented in this thesis were taken at either the European Synchrotron Radiation Facility (ESRF) in Grenoble, France (BM28 [77] and ID32 [78]), or the Advanced Photon Source (APS) situated in Argonne, Chicago (12BM[79]). Synchrotron radiation is provided by the acceleration of electrons around a large storage ring. Bending Magnet (BM) beamlines use wigglers to oscillate electrons and give off radiation, whereas "ID" beamlines use an undulator. The difference is that the undulator causes the electrons to oscillate at the same frequency

as the radiation which they are producing. The constructive interference which results provides a much more intense beam, with a much narrower band of wavelengths. As such, ID beamlines are well suited to experiments which require a high flux x-ray beam.

The monochromator allows the user to select the required wavelength from the incoming "white beam", consisting of a range of wavelengths. A single crystal (typically silicon) target is used to select a certain wavelength from the white beam – from Bragg's law it can be seen that x-rays of a certain wavelength will be preferentially diffracted. Once the wavelength is defined, the beamline optics are used to focus the beam at the centre of the circles of rotation of the diffractometer. Aluminium attenuators can be used to reduce the flux, and the use of ion chambers allows the user to "monitor" the incoming beam intensity (for the purpose of normalising their signal).

When the cell is mounted on the diffractometer, it is imperative that the sample is placed at the centre of the rotation of all the circles of motion. These can be seen in Figure 3.3.1. If this does not occur, then any rotations will cause the incoming beam to illuminate a different area of the sample surface and thus provide unsystematic measurements.

To ensure this is avoided, the sample is "laser aligned", which involves shining a laser on the sample and rotating it through the different circles of motion, to ensure iteratively that the sample is not translated under rotation. The sample is then used to "half cut the beam – this ensures it is illuminated by the incoming x-rays. During experiments, the detector slits can be used to select the optimal signal to background ratio by filtering some of the diffracted beam.

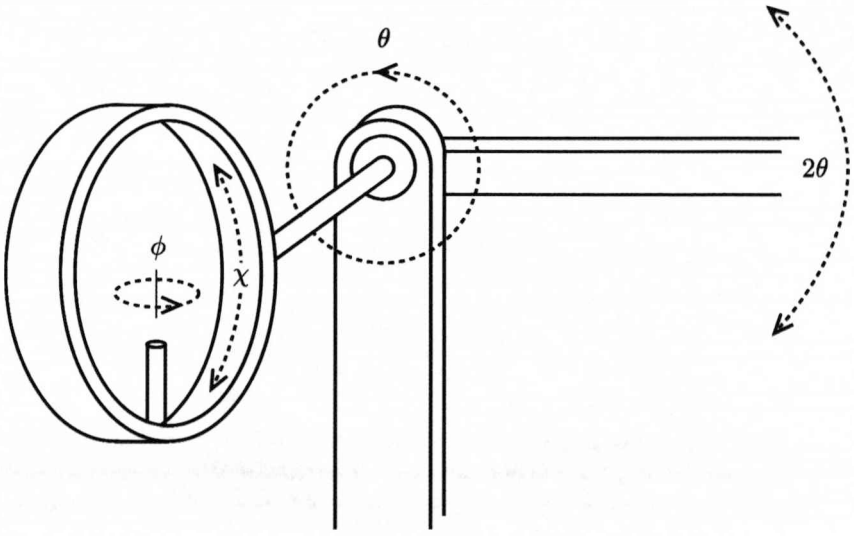

Figure 3.3.1: The various circles of rotation of a typical diffractometer

A Germanium based solid state detector (Vortex brand) was used. Also, the flight path between the sample and detector was under vacuum to reduce air scatter.

The sample is aligned on the diffractometer by manually locating two Bragg positions in real space, and then relating them to their reciprocal space lattice positions. This requires the real lattice parameters of the sample, and the reciprocal lattice coordinates of the two chosen reflections, to be entered into a computer program called SPEC. By relating the real space angles to the reciprocal space positions, the program allows the user to select which point in reciprocal space the detected rays come from.

3.4 Data Acquisition

To profile the behaviour of a given system, various different x-ray measurements can be performed. A rocking scan is used to profile fully the intensity at a given reciprocal space position – the integrated intensity (obtained either by fitting a lineshape, or using a numerical method) of the background subtracted scan is used as a value of the intensity at the scan position. Such scans are also indicative of the sample surface quality – if a rocking scan at an 'anti-Bragg' position yields a detectable peak then the surface is deemed of high enough quality to work with. This is because at anti-Bragg positions, the scattered intensity from the bulk destructively interferes (see Chapter 2). These positions are thus extremely surface sensitive, and a sharp peak shows that the surface layers are well ordered. When taking CTR measurements, it is desirable to probe the background on both sides of the position in reciprocal space. This ensures any errors due to misalignment effects are minimised. Theoretically, it is good practice to look at the intensity profiles at various different symmetrically equivalent positions. This gives a measure of the systematic errors incurred due to misalignment, illuminating different areas of the sample surface, and different sample motion directions. Typically, these errors are found to be approximately 10%. As this is much greater than the associated statistical errors (from counting scintillation events in the detector), 10% is often used as an approximate error on data points. Time constraints mean that checking the symmetry equivalent positions is sometimes not feasible, but from experimental experience this 10% value is quite standard. CTR measurements must be corrected before fitting them with a suitable model. The low angle correction accounts for the fact that at small incident angles, the beam footprint is larger than the sample. The correction factor

$$A = R \sin \theta_i \tag{3.1}$$

is used, where R is the ratio of the sample diameter to the beam width and θ_i is the angle of incidence; θ_i for the specular CTR is given by $\theta_i = \sin^{-1}(\lambda q/4\pi)$ and $\theta_i = \sin^{-1}(\sin\theta\sin\chi)$ for scattering with an in-plane contribution to momentum transfer. For the above equation, λ is the incident x-ray wavelength, whereas θ and χ are diffractometer motor positions. Although not shown here, corrections were also made for instrumental resolution differences between different scattering geometries. See reference [80] for details.

The in-plane structure of a surface (or adsorbate) can be probed using the following method. A scan along a <hk> direction, with minimal out of plane momentum transfer (*e.g.* l = 0.15 for a Pt(111) sample) is used to detect the structure initially. Due to surface energy considerations, these scans are typically (but not exclusively) along high symmetry directions. When a structure peak is found, a rocking scan is used to locate the exact position of the scattering in reciprocal space. This scan can then be used to determine the coherent domain size (D) of the structure, from

$$D = \frac{2}{\Delta q} = \frac{2}{q\Delta\theta} \tag{3.2}$$

where $\Delta\theta$ is the full width at half maximum (FWHM) of the peak (radians) obtained from the fitted line-shape to the rocking scan, and q is the momentum transfer.

One of the key measurements performed throughout this thesis has been the potential dependent response of the x-ray signal at key reciprocal lattice positions. Such measurements are termed x-ray voltammetry (XRV), as they show the potential

induced effect on the scattered signal. Such scans can be used to probe various phenomena, such as in-plane ordering (at in-plane anti-Bragg positions), lateral surface relaxations (at positions close to specular rods), and phase transitions occurring on both surface reconstructions and surface adsorbates (see Chapters 4-6). As such, they play a vital role in developing a structural understanding of the systems studied in this thesis.

Chapter 4

Pt(111) – from UHV to an Electrochemical Environment

4.1 Introduction

The structure and bonding of water molecules at a surface is a key issue in electrochemistry, as water activation plays a crucial role in many solid surface electrochemical reactions. As a result, water structures are of fundamental importance when trying to determine structure-function relationships in electrochemical systems. Despite numerous experiments, water structures and their behaviour at the electrified interface are not yet truly understood. Menzel *et al.* have recently used traditional surface science techniques to study the structure and bonding of water on transition metal surfaces, enhancing the current understanding [81]. Feibelman proposed that the stable configuration of water on Ru(0001) was a partially dissociated overlayer consisting of a hexagonal network, and that this partial dissociation was required for wetting to occur on Ru(0001) [82]. Vibrational spectroscopy experiments have shown similar results for Pt(111) [83], although here it was found that the overlayer comprised intact H_2O molecules. However, low energy electron diffraction (LEED) analysis suggested a dissociated layer of OH on Pt(111) [84]. Clay *et al.* have recently addressed the issue of dissociation, by studying a mixed composition overlayer (OH_x) on Pt(111) to determine how hydrogen bonding affects stability [85]. They found that the optimal structure is a mixed (OH + H_2O) phase forming a hexagonal ($\sqrt{3}x\sqrt{3}$)R30°

lattice with a weak (3x3) superstructure caused by ordering of the hydrogen bonds. The stability of the overlayer decreases as the H_2O content is reduced although a range of compositions can exist.

Although water structures can be observed by LEED on metal surfaces under ultra-high vacuum (UHV) conditions, the electrochemical interface is much harder to study due to the presence of the bulk electrolyte. In order to understand the role of hydration water molecules on the electrochemical double layer, it is imperative to reveal the structure under control of the electrode potential. By developing a better of understanding of water-metal interactions, we can develop our knowledge of various key electrochemical processes, including metal potentials, corrosion, and catalysis.

In electrolyte solutions free of strongly adsorbing anions, *e.g.* KOH, the electrochemical interface offers the opportunity of controlling the surface coverage by hydrogen, H_2O and OH species simply by controlling the applied electrode potential. To probe, *in situ*, the structure of the water layer at the metal-electrolyte interface is a technically challenging experiment as the scattering signal from the ordered oxygen atoms is relatively small compared with the diffuse scattering from the bulk of the electrolyte solution.

In this Chapter, preliminary results obtained using a UHV transfer system to provide unprecedented control over the electrode surface structure during transfer from UHV to the electrochemical environment, are presented. To illustrate the experimental possibilities, a single experiment in which a Pt(111) surface was prepared in UHV, dosed with oxygen to form a p(2x2) oxygen adlayer and then studied with SXS, initially under UHV conditions, then in a N_2 atmosphere before a droplet of water was contacted with the surface. Measurements of the surface structure were then performed on the surface modified by the bulk water overlayer before the water was

exchanged with 0.1 M KOH electrolyte and the Pt(111) electrode put under potential control to allow potential-dependent studies of the interface structure.

4.2 Experimental Methods

After UHV preparation of a sample, the surface quality can be checked using low energy electron diffraction (LEED) and auger electron spectroscopy (AES) techniques, to ensure it is both clean and structurally well defined. The Pt(111) electrode was prepared at the surface characterization laboratory (SCL) at the ESRF [86]. This involved numerous cycles of sputtering and annealing until a sharp (1x1) LEED pattern was obtained. The sample was then exposed to molecular oxygen at room temperature until a sharp p(2x2) LEED pattern, characteristic of the stable Pt(111)-O structure with a saturation coverage of 0.25 monolayers, was observed [87]. The chamber pressure was 10^{-6} τ whilst dosing with oxygen.

SXS measurements were performed on the 6-circle surface diffractometer at the ID32 beamline at the ESRF. The horizontal sample surface was aligned with the x-ray beam for a fixed incidence angle of 0.2 deg and the orientation of the crystal lattice determined. The close-packed (111) surface has a hexagonal unit cell that is defined such that the surface normal is along the (0, 0, L) hex direction and the (H, 0, 0) hex and (0, K, 0) hex vectors lie in the plane of the surface and subtend 60 deg. The units for H, K and L are $a^* = b^* = 4\pi/\sqrt{3a_{NN}}$ and $c^* = 2\pi/\sqrt{6a_{NN}}$ where a_{NN} is the nearest-neighbour distance in the crystal (a_{NN}=2.78 Å). Due to the ABC stacking along the surface normal direction, the unit cell contains three monolayers and the Bragg reflections are spaced apart by multiples of three in L. The incident X-ray beam

(energy=22.2 keV) was collimated to a spot size of 40 μm (vertically) by 0.3 mm (horizontally) and the scattered X-ray beam was detected after reflection from a graphite analyzer crystal. CTR data were obtained by performing rocking scans around the surface normal at successive L values to obtain background-subtracted integrated intensities at each L position.

Following the X-ray experiments performed under UHV conditions, the TRECXI chamber was filled with high purity nitrogen and selected X-ray measurements were performed to verify the stability of the Pt(111)–O surface. The electrochemical cell was then mounted above a UHV valve on top of the Be cylinder and can be lowered toward the sample once the chamber is filled with inert gas at ambient temperature and the UHV valve is open. Once the measurements in N_2 were performed, a droplet of pure water was contacted with the Pt(111)–O and the measurements were repeated. Following the measurements in pure water, ultra high purity 0.1 M KOH (Aldrich) was used as the electrolyte and potential contact to the sample was made at -1.0 V (relative to Ag/AgCl).

4.3 Results and Discussion

4.3.1 Pt(111)-p(2x2)-O

Characterization of the Pt(111)-O surface whilst under UHV conditions inside the TRECXI chamber was performed immediately after transfer to the diffractometer. Rocking scans were performed at (1, 0, 0.1) and (0, 1, 0.2) to determine qualitatively the quality of the Pt(111) surface. Chapter 3 explains this process, but it is worth noting that at these positions we are particularly sensitive to the in-plane ordering of

the Pt surface. From these scans, it was deduced that the surface order was sufficient to perform the experiments.

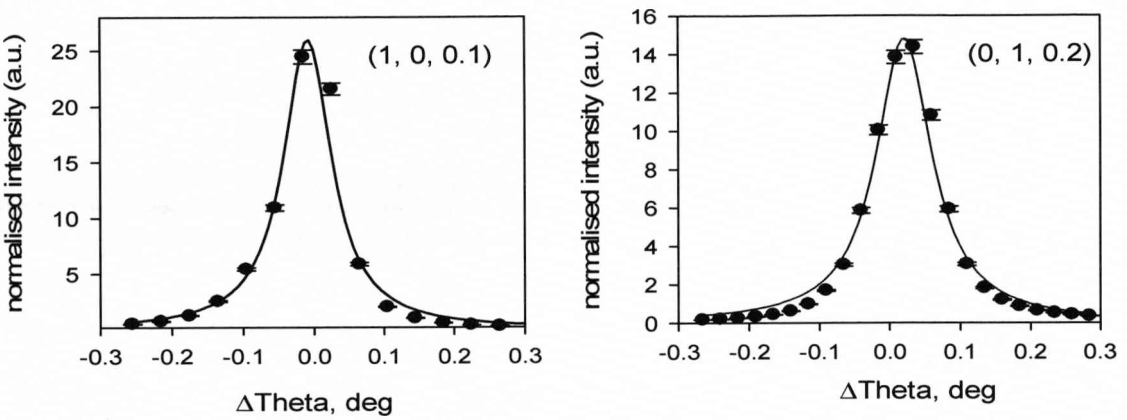

Fig 4.3.1.1: Preliminary qualitative checks of the sample surface at in-plane surface sensitive reciprocal space positions. The solid lines show Lorentzian fits to the curves. The count rate at (1, 0, 0.1) was $2x10^6$ counts per second (cps) on a background of $9x10^3$. At (0, 1, 0.2), the count rate was $1.3x10^6$ cps on a background of $7x10^3$ cps.

Figure 4.3.1.2 shows a rocking scan and a radial scan through the (1/2, 1,2, 0.1) position, both of which are sensitive to the scattered intensity from the p(2x2)-O structure. The scans performed were measured for 5 seconds per point indicating the weakness of the scattered signal from this layer. This is to be expected from a 0.25 monolayer, due to the low atomic number of oxygen.

Fits of a Lorentzian lineshape to the data (shown by the solid lines in Fig 4.3.1.2a and Fig 4.3.1.2b) give a coherent domain size in the range 90–130 Å (see Equation 3.2). Due to the weakness of the scattering it was impossible to collect a full set of structure factors that could then

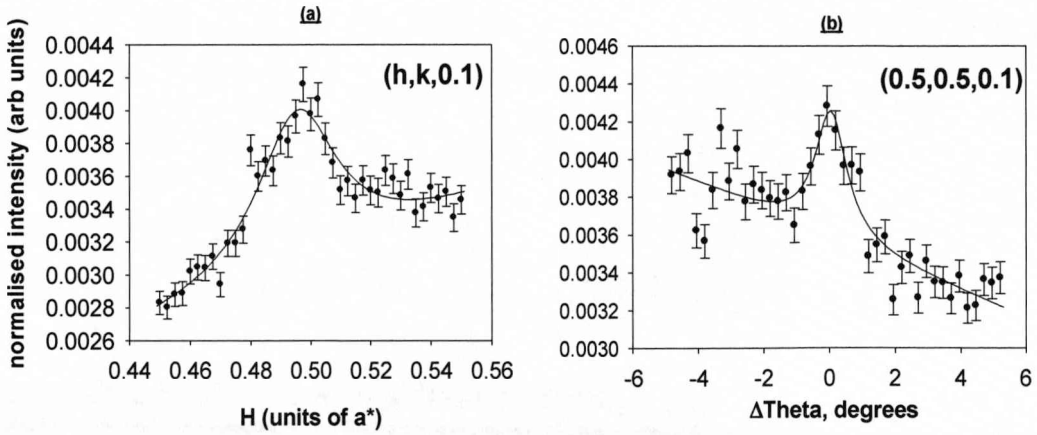

Figure 4.3.1.2: A radial scan (a) and a rocking scan (b) through the (0.5, 0.5, 0.1) reciprocal lattice position from the Pt(111) p(2x2)-O surface in UHV. For the radial scan we measured 440cps on a background of 360cps, and for the rocking scan 440cps on a background of 365cps.

be used for structural refinement. However, the intensity distribution implied that there was no significant Pt contribution to the scattering from the p(2x2) unit cell, in contrast to previous SXS measurements of the structure in which relaxation of multiple Pt layers was proposed [88]. In these previous studies, Nakamura *et al* found displacements of platinum atoms over ten surface platinum layers. Such behaviour would result in asymmetric CTR profiles, which was in contrast to our data.

To characterise fully the surface, seven symmetry independent CTR's were measured, of which six are shown in Figure 4.3.1.3. For each CTR corrections have been made for instrumental resolution using methods devised by Vleig [89]. In essence these corrections account for the fact that at different CTR positions a different proportion of the beam is absorbed. A 10% systematic error was associated with each data point, which is consistent with the differences typically found between symmetry equivalent CTR positions and was discussed in Chapter 3.

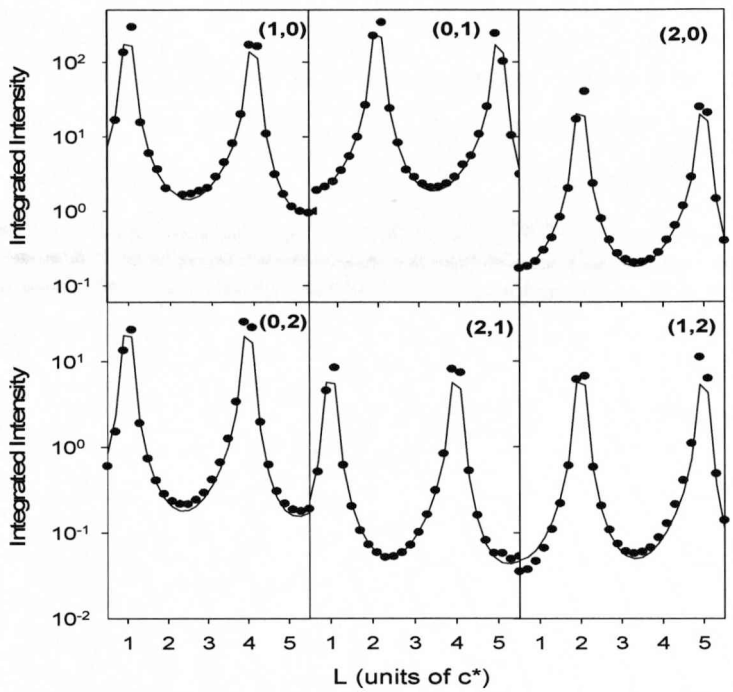

Figure 4.3.1.3 Crystal truncation rod (CTR) data of the Pt(111)-p(2x2)-O surface measured in UHV. The circles correspond to background-subtracted integrated intensities that are corrected for the instrumental resolution. The (H, K) values for each CTR are indicated. The solid line is a fit to the data using the structural model shown in Fig. 4.5 according to the parameters listed in Table 4.1.

The CTR data lack any significant features, again highlighting the weakness of the scattered signal from the p(2x2)-O layer, and indicate no significant Pt reconstruction as the anti-Bragg positions are largely unchanged. Fig. 4.3.1.4 illustrates the structural model used to fit the CTR data. Results are summarized in Table 4.1 below.

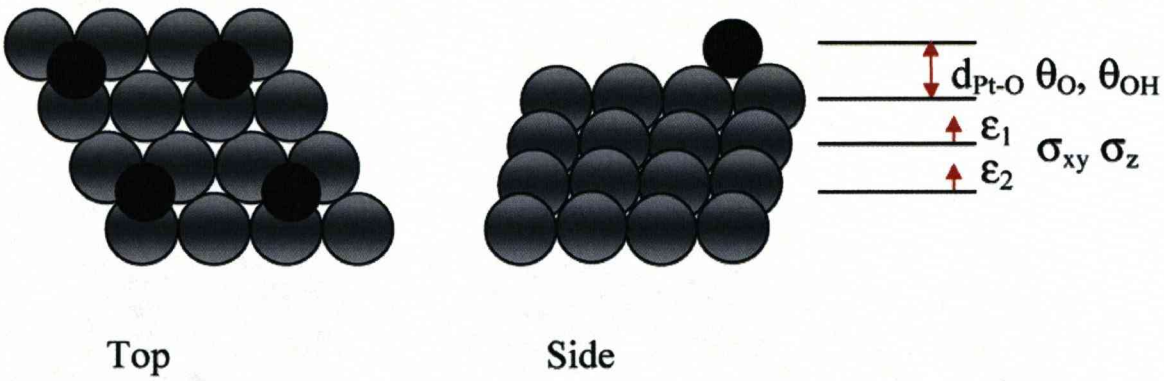

Figure 4.3.1.4: Structural model showing the set of parameters used to fit the CTR data.

System	θ_H, θ_{OH}	d_{Pt-O}/A °	ε_1/A °	ε_2/A °	σ_{xy}/A °	σ_z/A °
Pt(111)-O	0.25f	1.5(0.2)	+0.05 (0.005) [2.2%]	0.005 (0.005)	0.06 (0.01)	0.0
Pt(111)-H_2O	0.7(0.3)	1.9 (0.4)	+0.03 (1.3%)	0.01	0.10	0.0
Pt(111)KOH (E=-1.0V)	0	na	+0.05 (2.2%)	0.005	0.06	0.0
Pt(111)KOH (E=-0.1.0 V)	0.55 (0.2)	2.1 (0.4)	+0.04 (1.8%)	0.0	0.06	0.0

Table 4.1: Structural parameters for the fits to the Pt(111) CTR data - f indicates a parameter that was fixed. Uncertainties are indicated in brackets. ε_1 is also quoted as a percentage of the Pt(111) atomic layer spacing.

A least squares refinement procedure was used to provide the fit to the CTR data. The χ^2 parameter, indicating the accuracy of the calculated curve relative to the measured data, improved from 4.0 to 3.5 when the p(2x2)-O structure was added to the model. It

must be noted that the value itself is arbitrary as it is dependent on the error values assigned to each data point. However, it gives a good measure of the relative accuracy of the calculated curves. This model considers the oxygen atom to be adsorbed at the 3-fold hollow Pt surface site, as other sites were tested but the 3-fold hollow site gave the best fit. Table 4.1 illustrates the best fit parameters. The fit to the data was not improved by including buckling of the surface and sub-surface Pt atoms in the p(2x2) unit cell (which differs from previous LEED-IV studies of the Pt(111)-O surface [87]). Therefore we modelled the data with a Pt-(1x1) unit cell allowing for relaxation, according to parameters ε_1 and ε_2, and an asymmetric static Debye-Waller factor of the form:

$$\exp(-0.5Q_{in-plane}^2 Q_{xy}^2)\exp(-0.5Q_z^2\sigma_z^2) \tag{4.1}$$

This accounts for small Pt lattice distortions. The same model was then used to fit all of the CTR measurements made for the different states of the Pt surface. The fitted rods provided a set of structural parameters which implied outward relaxation of the Pt atomic layer by 0.05 Å. This is in good agreement with the previous LEED-IV study which found an outward relaxation of 0.01 Å, and a buckling effect which caused 3 of the 4 p(2x2) unit cell Pt atoms to be additionally expanded by 0.04 Å [87]. The Pt–O vertical spacing was found to be 1.5 +/- 0.2 Å compared with 1.24 Å found in the LEED-IV study and 1.46 Å in density functional theory (DFT) calculations. In general the SXS results are in good agreement with the previously quoted LEED-IV studies and theoretical results. As buckling of the p(2x2) unit cell did not improve the calculated fit to the data, it was not included in the structural model.

Once the UHV measurements were complete the chamber was brought back up to an N_2 atmosphere. The measurements shown in Figure 4.3.1.2, along with some of the CTR measurements, were then repeated. These results were identical, indicating that the Pt(111)–p(2x2)-O surface was stable in the inert atmosphere. A droplet of water was then contacted with the surface according to the experimental procedures described previously in section 4.2.

4.3.2 Pt(111) – H_2O Interface

Ordered oxygen layers on Pt(111) have been shown previously to help pin ordered water structures at the surface in low temperature UHV experiments [85, 90]. One of the experimental aims was to search for such ordered water structures. Once contact with the water droplet was made, scans were performed along various high symmetry directions in reciprocal space (<H,0>, <0,K> and <H,K> at fixed L values, 0.1, 0.8) to search for ordered structures in the surface plane. Additionally, key lattice positions, such as half integer and 1/3 integer positions, were also probed *via* rocking scans. This is where scattering from the p(2x2)-O [87], ($\sqrt{3}$x$\sqrt{3}$)R30° and (3x3) [85, 90] water structures formed in UHV at monolayer water coverage would be expected. At all the positions measured, nothing other than background scatter was observed. Due to background scatter from the water droplet itself, it is a possibility that scattering from any ordered structures present was too weak to detect. The very weak signal from the p(2x2)-O layer, shown previously in Figure 4.3.1.2, would support this argument. It was therefore not possible to determine categorically whether or not an ordered water layer was present on the surface. It would be interesting to prepare the ($\sqrt{3}$x$\sqrt{3}$)R30° water structure in UHV, and then contact the water droplet, for x-ray

[87] measurements. This, however, would require development of the TRECXI chamber to allow cold sample transfer.

Changes at the surface atomic structure, induced by the presence of bulk water, were monitored by repeating the earlier set of CTR measurements. These measurements were then normalised to the data shown in Figure 4.3.1.3, *i.e.* to the p(2x2)-O data. The results are shown in Figure 4.3.2.1 below:

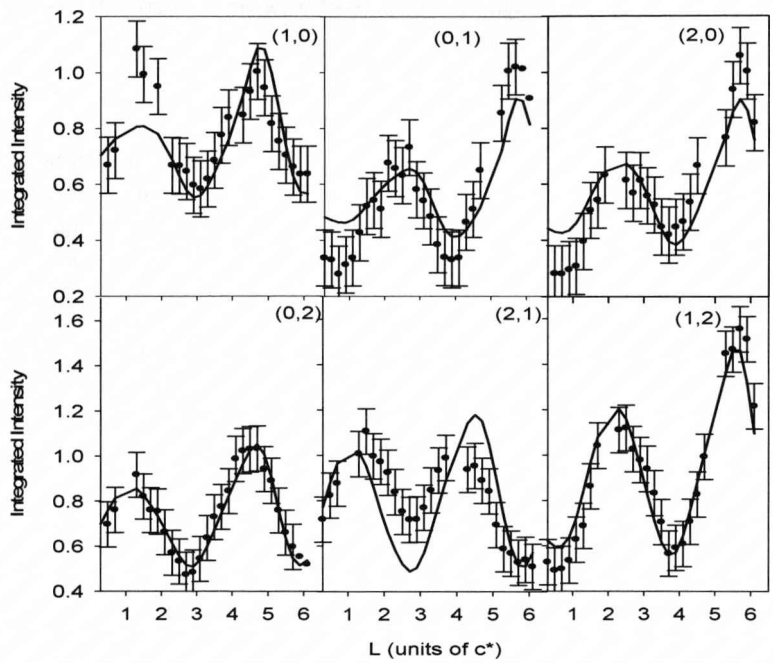

Fig 4.3.2.1: Ratios of the CTR data (Pt(111)-H_2O divided by Pt(111)-p(2x2)-O) . The (H,K) directions are shown. A constant error of +/- 0.1 is assigned to each data point. The solid line is a fit to the data using the structural model shown in Figure 4.3.1.4 above.

The ratio data in Figure 4.3.2.1 above clearly show systematic changes in the CTR intensities, corresponding to structural changes at the interface caused by adsorption of the water over-layer. This is a significant result, as it demonstrates the experiment to be sensitive to structural changes on the Pt surface due to water adsorption. This is in spite of the weak scattering from H_2O molecules, and gives a good demonstration of the capabilities of x-ray based experiments.

The data were fitted using the structural model shown in Figure 4.3.1.4. Attenuation effects due to x-ray adsorption in the electrolyte do not differ significantly with varying *L*. This leads to a constant attenuation effect (compared with the UHV data). This was accounted for by allowing the scale factor multiplying the CTR data to vary when fitting the ratio data set. A constant error of +/- 0.1 was assumed for each ratio data point, shown by the error bars in Figure 4.3.2.1.

Given that no in-plane ordering at the Pt(111)–H_2O interface was detected, it is impossible to build detailed structural models in order to reproduce the CTR ratio data. However, the systematic changes observed in Fig. 4.3.2.1 are consistent with a structural rearrangement at the interface and so it is intuitive to explore the origin of the changes. The calculated curves (shown by the solid lines in Fig. 4.3.2.1) used a very simple (1x1) unit cell allowing only for changes in the relaxation parameters. A fit to the data without the presence of a θ_O adlayer gave a χ^2 of 1.9. The principal structural changes are a reduction in the Pt surface expansion accompanied by an increase in the in-plane component of the Debye–Waller factor consistent with some in-plane distortion of the Pt lattice. This result would be expected for an increased surface coverage by oxygenated species. Including an oxygen layer in the model gave the fit to the data shown in Fig. 4.3.2.1 (χ^2 = 1.3). Different adsorption sites in the (1x1) unit cell were tried but there was a clear preference for the 3-fold hollow site. Models based on the ($\sqrt{3}$x$\sqrt{3}$)R30° and (3x3) structures, previously observed for the mixed OH–H_2O layer in UHV [90], did not improve the fit to the data obtained without an adsorbed O layer. In particular, it was found that a good fit could not be obtained with O adsorbed at a Pt on-top site. In UHV studies the sharpest LEED patterns are observed when water is adsorbed onto a disordered oxygen adlayer with a reduced coverage of $\theta_O \sim 1.5$ [91], compared to the p(2x2) phase (θ_O = 0.25). It is

possible, therefore, that in our experiment the oxygen was stabilized in the 3-fold hollow site although it is clear that a reaction with bulk H_2O has occurred. At present it is thus difficult to reconcile the results with the UHV studies of water adsorption at low temperature. As noted in the following section, the inclusion of the oxygen adlayer to fit the data in Fig 4.3.2.1 is statistically significant, as fits to the CTR data in 0.1 M KOH at -1.0 V, where atomic hydrogen is adsorbed onto the surface [32], are consistent with the removal of the oxygen adlayer (see below). At this stage, however, we cannot rule out that the CTR data could be reproduced with more complex surface models.

4.3.3 Pt(111)-0.1M KOH

After the measurements in bulk H_2O the water droplet was replaced *in situ* with 0.1 M KOH electrolyte and contact was established at -1.0 V (versus Ag/AgCl). The x-ray voltammogram shown in Figure 4.3.3.1 was taken at the (1, 0, 3.6) reciprocal lattice position, which is sensitive to Pt(111) surface expansion. Sweeping anodically from -1.0 V, the reduced intensity in the x-ray signal is due to inward relaxation of the Pt surface. This is caused by desorption of hydrogen from the surface, and reaches a minimum at ~ -0.6 V.

The increase in intensity on the positive sweep is a result of the outward relaxation of the surface caused by the adsorption of OH anions. This outward relaxation is stable on the cathodic sweep until OH desorption occurs, causing inward relaxation and hence a reduction in the signal. Finally hydrogen is adsorbed at approximately -0.75 V and the signal increases due to outward relaxation, showing the x-ray voltammogram (XRV) to be fully reversible.

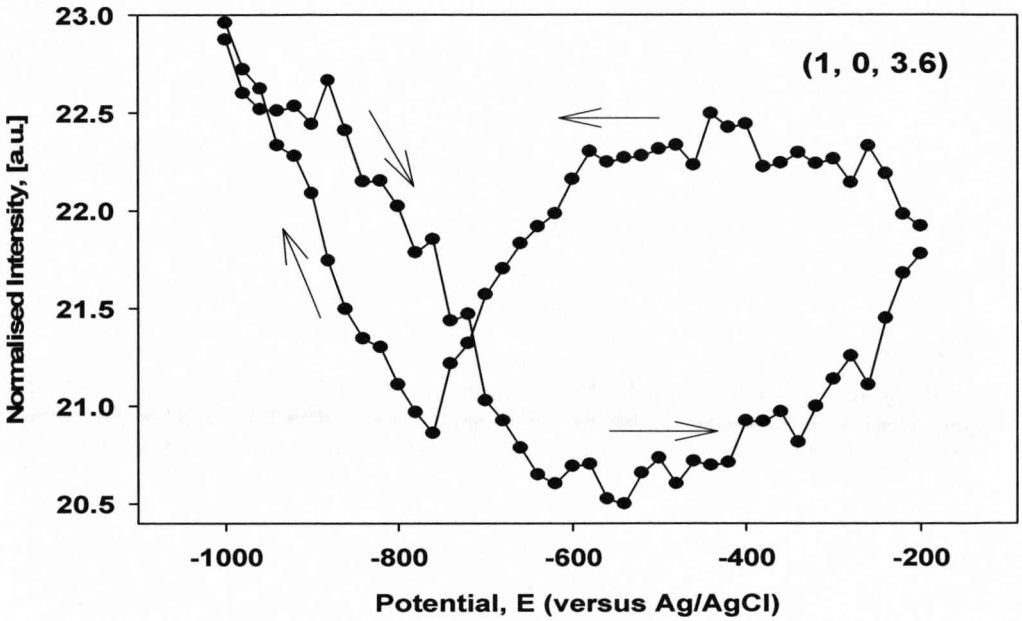

Figure 4.3.3.1: An x-ray voltammogram (XRV) measured at (1, 0, 3.6) for the Pt(111) electrode in 0.1 M KOH. This position is sensitive to Pt(111) surface expansion. The sweep rate was 4 mV s^{-1}.

CTR measurements were again performed and modelled to characterize the surface. At -1.0 V, previous studies have shown that ~ 0.66 monolayers of hydrogen are adsorbed on the Pt(111) surface in this electrolyte [32, 92]. Therefore the coverage of oxygenated species, *i.e.* θ_{OH}, is constrained to be zero. An outward surface expansion, of the topmost Pt layer of ~ 2.2 % was found. This is in excellent agreement with previous measurements on this system [93]. The measured surface expansion with OH adsorbed on the surface is also in excellent agreement with the local density functional (LDF) calculations on this system by Feibelman [94].

After the SXS measurements at -1.0 V, the potential was cycled (between the limits shown in Figure 4.3.3.1) at 4 mV s^{-1} and held at -0.1 V. The measurements were then repeated. Similarly to the Pt(111)-H_2O system, we searched along various (H,K) directions in the surface plane to look for scattering from an ordered OH adlayer. Once again no scattering from such a structure was detected.

Systematic changes in the CTR ratio data (-0.1 V data/-1.0 V data) are clearly illustrated in Figure 4.3.3.3, although these changes are markedly smaller than those presented in Figure 4.3.2.1. Again, the (1x1) unit cell was used to model these systems and the results are presented in Table 4.1. The best fit was obtained with OH adsorbed in the Pt 3-fold hollow sites, in agreement with the Pt(111)-H_2O data.

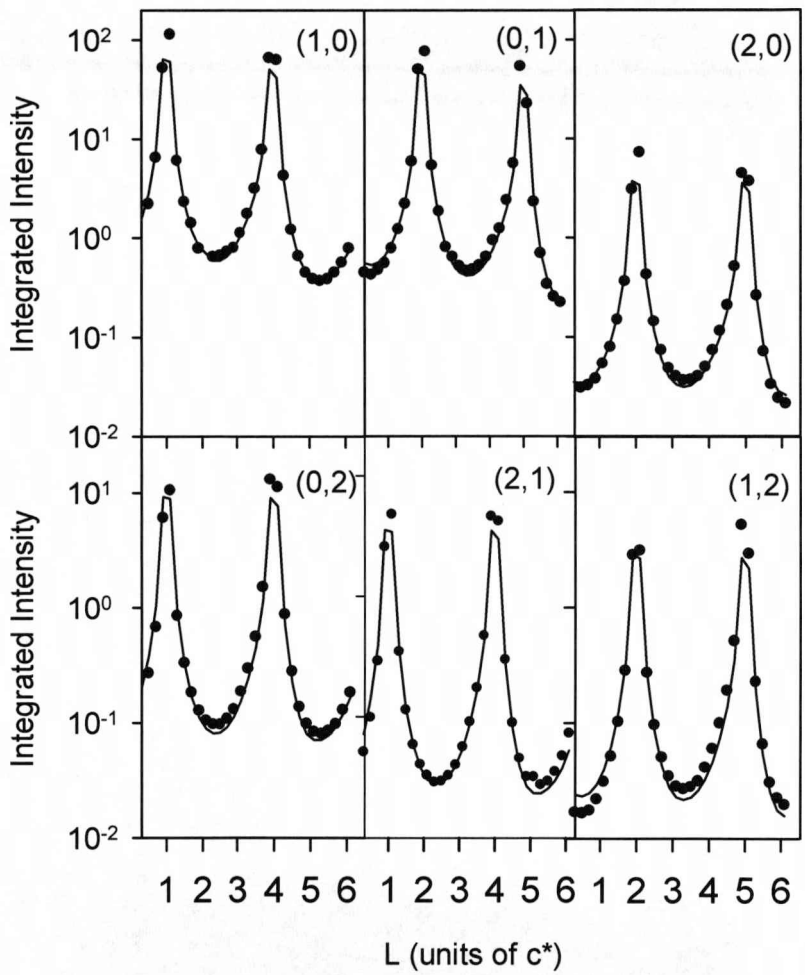

Figure 4.3.3.2: CTR measurements of Pt(111) in 0.1M KOH at -1.0 V. The circles show the background-subtracted integrated intensities, which are corrected for instrumental resolution. The solid lines show the fit obtained from the model shown in Figure 4.3.1.4, and the fit results are presented in Table 4.1.

It must be stated that this model did yield a larger than expected Pt-O spacing. It can be seen from Figure 4.3.3.3 that the model does not profile the measured data perfectly, as some measured features are not reproduced in the calculated curve.

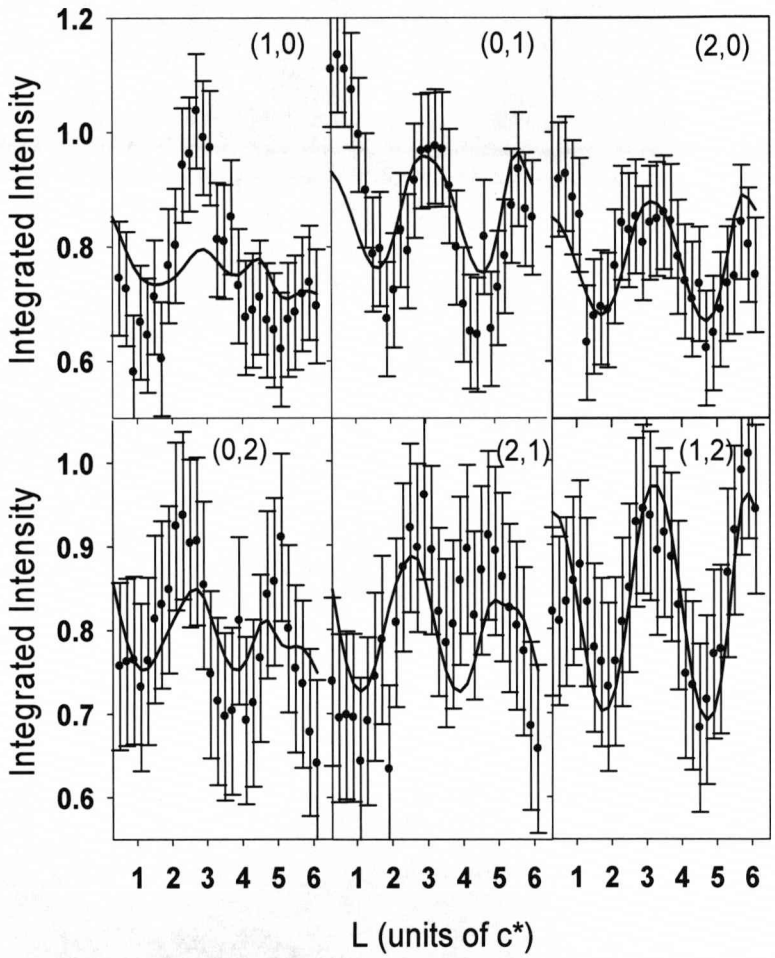

Figure 4.3.3.3: Ratio data for Pt(111)-0.1 M KOH obtained by dividing the CTR data measured at -0.1 V by the CTR data measured at -1 V, where (H,K) values are indicated in brackets. The black circles indicate the measured ratios (a constant error of +/- 0.1 is assumed). The solid line shows the fit data obtained using the model shown in Figure 4.3.1.4.

Further experiments are thus required to gain a more in-depth understanding of the Pt(111)-OH_{ad} interface. Mesh scans, which can probe a 2 dimensional area of reciprocal space, could be used to search for water structures with symmetry different to that suggested by the experiments presented in this Chapter. Also, species known to interact with H_2O could be introduced to the system, and the CTR profiles monitored during this process. These suggestions are a starting point for new experiments which could utilise the x-ray technique to enhance the current understanding of the Pt(111)-OH_{ad} interface.

4.4 Summary

In this Chapter it has been shown how SXS scattering experiments from the Pt(111) surface can be used to monitor the structural changes which result from bulk water adsorption, adsorbates such as OH anions, and adsorbed hydrogen. The experiments discussed also provide an illustration of the excellent scientific opportunities afforded by the TREXCI chamber. The p(2x2) adsorbed oxygen layer was verified with LEED, and then detected with x-rays in both the UHV and N_2 environments. The UHV to electrochemical transfer method was successful, as the results in UHV were unchanged when the TRECXI chamber was filled with N_2 and the measurements repeated. This transfer system thus provides the opportunity to study highly reactive systems in a clean electrochemical environment.

For the Pt(111)-H_2O system we assumed the oxygen adlayer to be present when constructing the model used to provide the calculated curves. This was justified as the calculations from the Pt(111) in 0.1 M KOH (data taken after the bulk water

measurements) are consistent with the removal of an oxygen adlayer. For Pt(111) in 0.1 M KOH, the assumption that no oxygen is on the surface at -1.0 V was made, as hydrogen is preferentially adsorbed at this potential [32]. I suggest that the work in this Chapter has shown how the UHV TRECXI system is an excellent transfer method which could also be used to study reactive surfaces, and artificial surfaces such as man-made alloys. I would also point out that water structures on Pt(111) are a challenging topic, with scope for more experimentation.

Chapter 5

Temperature induced surface ordering and potential dependent reconstructions at Au(hkl)-electrolyte interfaces

5.1 Introduction

Metal surface reconstruction, in which the topmost atomic layer assumes an ordered structure that can differ from the underlying bulk phase of the crystal, is a topic that is well studied in both UHV [21] and electrochemical surface science [63, 95]. In UHV, the surface reconstructions of Au are stable up to high temperatures, whereas in the electrochemical environment the state of the surface can be controlled by the electrode potential *via* the strong adsorbate-metal interaction and/or the electrode surface charge [96].

The Au (111) surface reconstruction has previously been shown to exhibit the well known (px$\sqrt{3}$) phase using a variety of *in situ* methods including STM [97-98], and SXS [99] based studies. Numerous vacuum studies have also been performed, using LEED [100], surface x-ray diffraction [101], and STM [102] techniques. More recently, advanced computational simulations have been performed in an attempt to try and obtain a more fundamental understanding of the Au(111) surface reconstruction [103]. Whilst the (px$\sqrt{3}$) reconstructed phase is widely accepted in both UHV and electrolyte, the exact nature of the surface behaviour is yet to be fully resolved. For example, the ordered array of kinks from UHV measurements (the so called "chevron" phase) [104], is not detected by x-rays when the surface is in contact

with electrolyte . The initial surface morphology of Au (111) plays an important part in the reconstruction process, and will be discussed.

For Au (100), the surface reconstruction involves significant transport of surface Au atoms, as the hexagonal reconstructed surface layer (on the underlying square bulk crystal lattice) has an atomic density that is ~20% greater than the (100) surface plane. Recent video-STM studies, in combination with previous STM results, have shown that the reconstruction proceeds by rapid nucleation of atomic "strings", at the adisland sites formed by the excess surface Au atoms, followed by agglomeration of the strings to form the long-range ordered hexagonal phase [105]. In this Chapter, a series of experiments designed to probe the effects of temperature on the surface reconstructions of the Au(111) and Au(100) faces in 0.1 M KOH are presented. The reader is referred to the introductory chapter for a more in depth discussion.

5.2 Au(111) in 0.1 M KOH – Previous Work

5.2.1 Cyclic Voltammetry

The effect of temperature on the voltammetry of Au(111) in 0.1 M KOH is presented in Figure 5.2.1 below. The peak at ~ 1.25 V, corresponding to surface oxide formation [106], is shifted cathodically with increasing temperature. The small peak at ~ 1.05 V is attributed to the adsorption of oxygenated species, which we believe to be a precursor for the lifting of the reconstruction. From the I/V curves above it can be seen that the processes occurring in the oxidation region, commonly assumed to be place exchange mechanisms between Au and OH (see reference [107] for more details), become more reversible with increasing temperature. By definition this must

impact on the surface morphology, as oxygen reduction cycles (ORC) are known to alter the atomic arrangement of noble metal surfaces [108]. For the specific case of Au(111), STM images have shown that on the reduction cycle a potential sweep causes the formation of monatomic deep "pits" across the surface [109]. It is possible that as a larger current passes on the anodic sweep at higher temperatures, any morphological changes due to this process (and the subsequent cathodic sweep which follows) will be amplified at this temperature. Therefore, at different temperatures, the nucleation of the reconstruction will be occurring on a surface with varying amounts of defects. Concomitantly, the surface reconstruction formed at contrasting temperatures should reflect this.

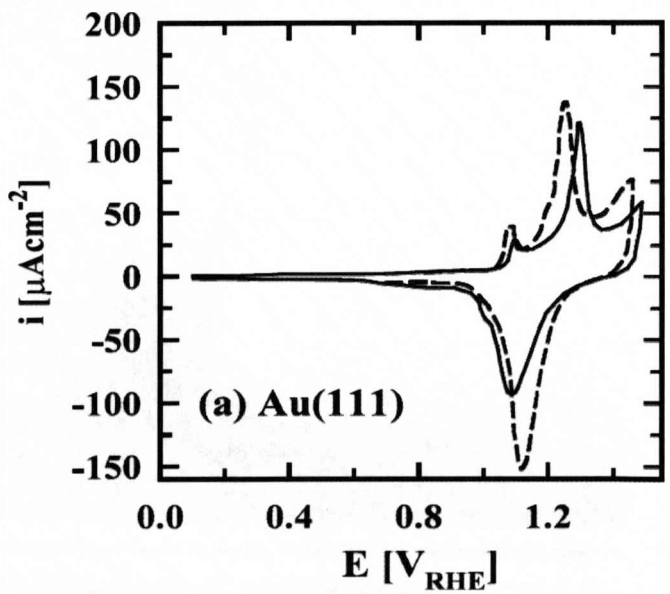

Figure 5.2.1.1: Cyclic voltammetry measurements on Au (111) taken at 50 mV s^{-1} in 0.1 M KOH (dashed line = 333 K, solid line = 293 K). Figure reproduced from reference [106].

5.2.2 The Au (111) Surface Reconstruction

To check the Au(111) surface quality, the rocking scans at anti-Bragg positions were measured, and yielded peaks indicative of a highly ordered surface (Figures not presented – see Chapter 3 for an explanation). Once this was established, the first part of the experiment was designed to probe the potential response of the surface reconstruction. More precisely, the first measurement was of the incommensurability, δ of the surface. This can be related to the "stripe separation" p, which reflects the length of a reconstructed layer unit cell in terms of the number of underlying atoms it overlays.

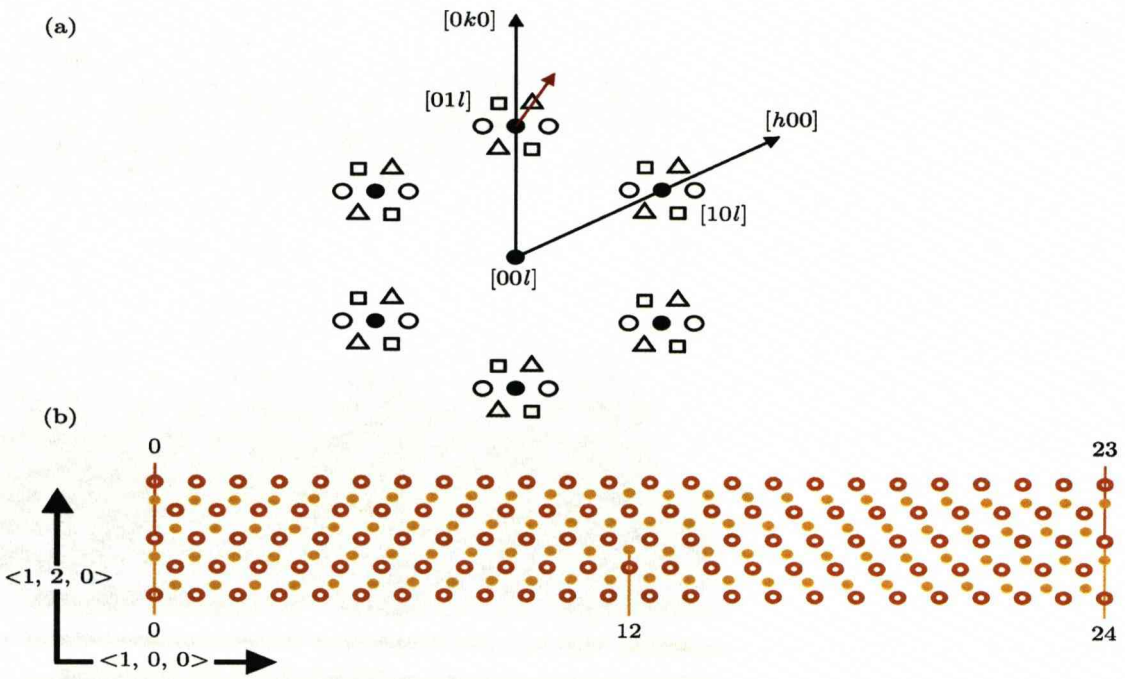

Figure 5.2.2.1: (a) The in-plane diffraction pattern produced by the Au(111) reconstruction. The open symbols represent the scattering from the three rotationally equivalent reconstruction domains. (b) The real space atomic arrangement of the Au (111) reconstructed surface. The open symbols represent the unreconstructed second layer of Au atoms. The closed symbols represent the 2D position of the reconstructed surface atoms relative to the underlying layer.

Figure 5.2.2.1(b) shows a real space model of the Au(111)-(px$\sqrt{3}$) surface reconstruction. The x-ray scattering from this structure gives rise to 3 symmetrically equivalent peaks in reciprocal space - this is illustrated in Figure 5.5.2.1(a). In the real space model shown, p is equal to 23, but is known to vary depending on the applied potential across the surface [99]. This value is a measure of the compression of the reconstructed surface, and was probed by stepping the potential in 50 mV steps, and measuring "hkscans" along the [01] direction. This is illustrated in Figure 5.2.2.2.

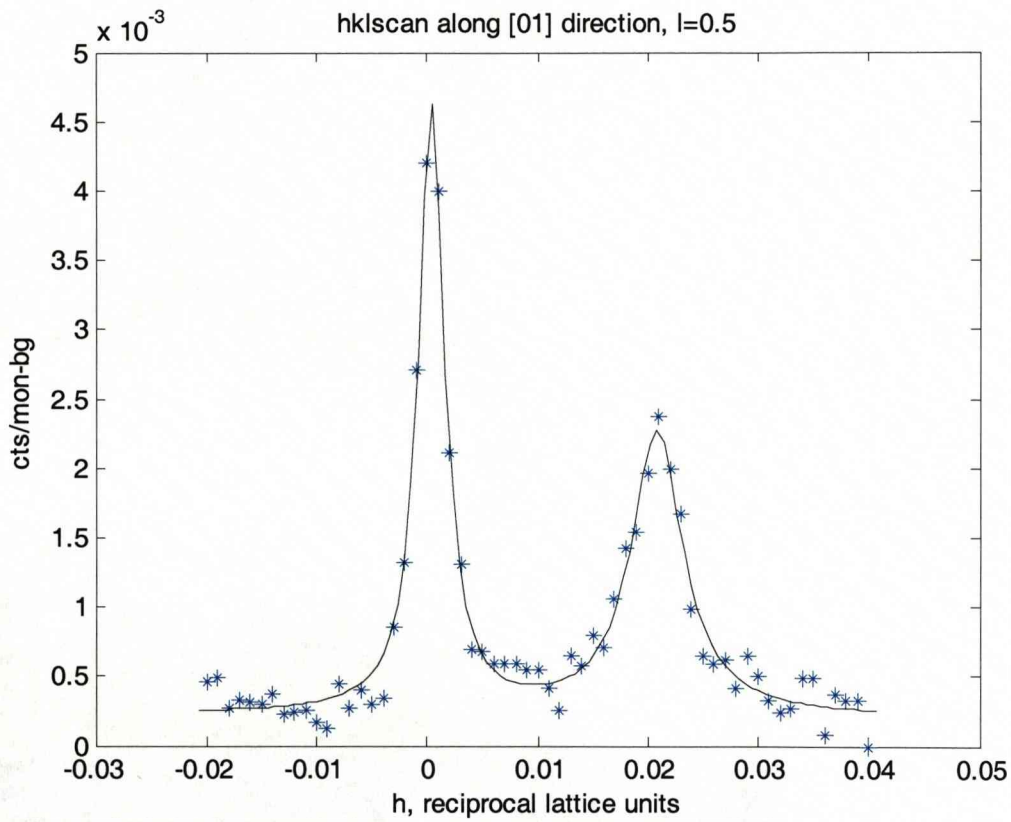

Figure 5.2.2.2: A scan at 299 K along the [01] direction at l = 0.5 performed on Au(111) in 0.1 M KOH, held at -0.75V vs. NHE. The peak at h = 0 is from the CTR, whilst the peak at h = 0.02 is from the reconstructed surface. The black line is a fit to the data using a double lorentzian function. This measurement is known as a "hkscan".

By fitting the hkscans with a double lorentzian lineshape it was possible to determine values of p, and also of the average domain size, D, of the reconstructed surface. The following relationships were used:

$$p = 1/2\delta \tag{5.1}$$

and

$$L_\delta = pa_{NN} \tag{5.2}$$

wfhere a_{NN} is the nearest neighbour distance of Au (2.885 Å). The incommensurability, δ, is simply the h position of the reconstruction peak as illustrated in Figure 5.3.2 above, and L_δ is the stripe separation in Å. Rocking scans at the (0.021, 1.021, 0.5) position were used to confirm the reconstruction - Figure 5.2.2.3 provides an example.

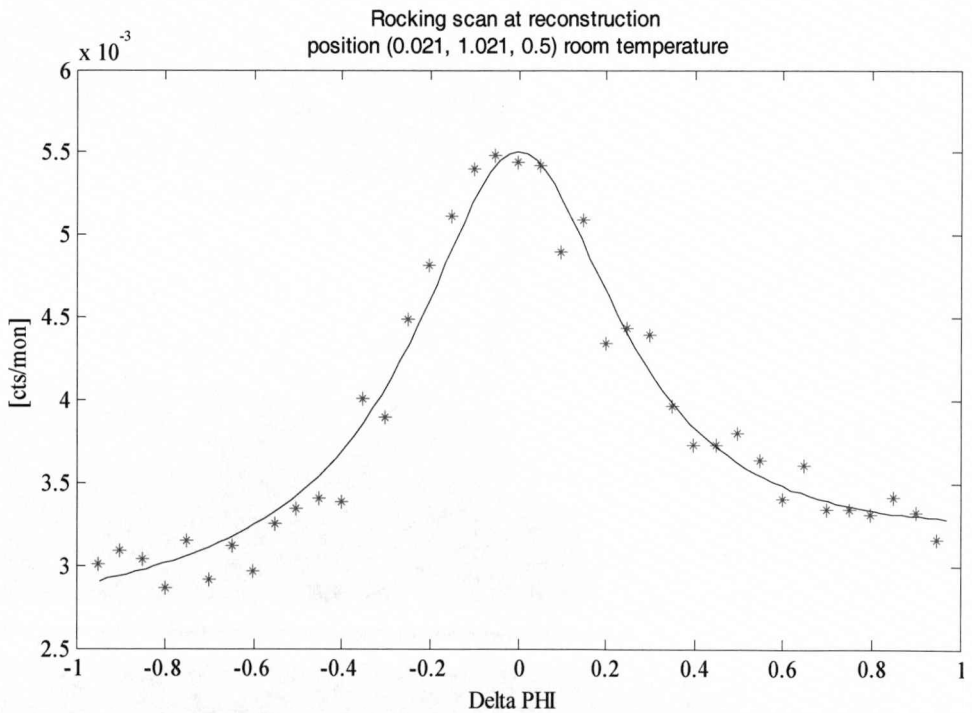

Figure 5.2.2.3: A rocking scan at the reconstruction position on Au(111) in 0.1 M KOH, where the solid black line is a lorentzian fit to the data.

5.2.3 Potential Induced Effects

The effect of potential on the reconstruction of Au(111) was probed at room temperature using the following method. The potential was stepped from the positive potential limit, in steps of 40 mV, to the negative limit. This induces the formation of the reconstruction. At each potential, a hkscan (as shown above), and a rocking scan at (0, 1, 0.5) were performed. From the analysis of this data, using Equations 5.1 and 5.2, Figure 5.2.3.1 was produced. Figure 5.2.3.1(a) shows the integrated intensities measured at (0, 1, 0.5), an 'anti-Bragg' position on the (0 1 L) CTR, and where scattering from the reconstructed phase occurs. This shows that, as the potential is swept negative, the reconstruction starts to form. In part (b) of the Figure, it can be seen that the reduction in potential causes a compression of the (px$\sqrt{3}$) layer, and an accompanying increase in the domain size (part (c)) of the reconstruction. This behaviour is somewhat similar to that found by Wang *et al* [111], yet seems to contain some intricacies which were not found in that study. For example, the "flat regions" in Figure 5.2.3.1(a), at the (px$\sqrt{3}$) position, indicate that the amount of reconstruction stays constant during certain potential windows. This effect is mirrored by the behaviour during the same potential window as seen in (b) and (c) of the same Figure. This suggests that the structure that exists is not changing during this potential window. This could indicate certain "energy barriers" for the formation of the reconstruction, suggesting that it is not a smooth transition but rather a stratified series of potential driven events. In the so called "flat regions" it is difficult to resolve what is occurring from a structural perspective, as the surface is in an intermediate state, being held between two known phases. However, the data provide useful information

on the nature of the Au(111) - (1x1) → Au(111) - (px$\sqrt{3}$) phase transition. For example, it shows that there are certain potential regions in which the stripe separation seems to remain constant, which may indicate a staggered reconstruction process involving more than one energy barrier. The data thus highlights the nature of the qualitative information available from the measurements of the phase transition presented.

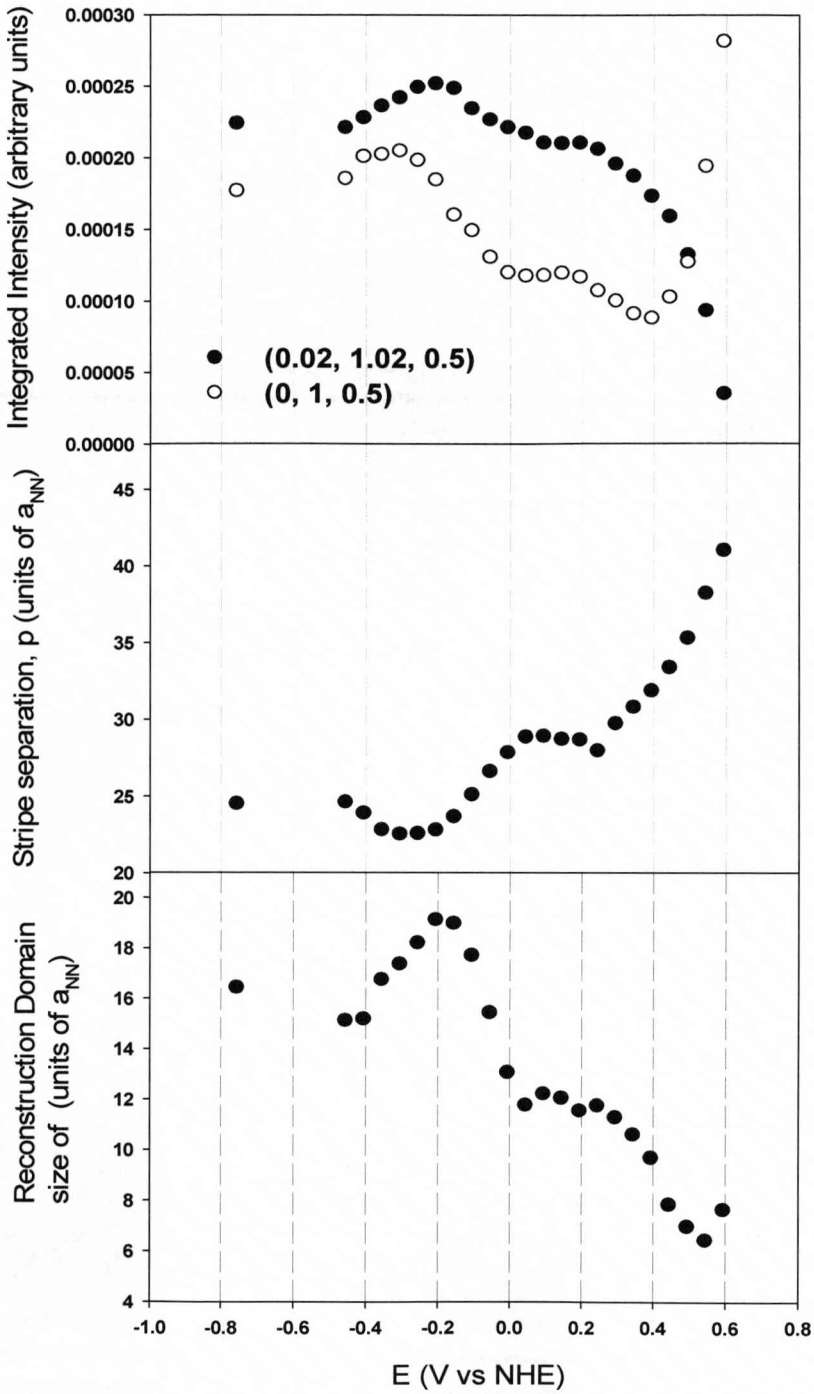

Figure 5.2.3.1: (a) The behaviour of the reconstruction signal, shown by closed symbols, and the signal from the in-plane anti-bragg position (open symbols). (b) The stripe separation, p, in units of a_{NN}, between successive (px$\sqrt{3}$) unit cells, and (c), the domain size of the reconstructed layer.

5.2.4 Temperature Effects

To probe the effect of temperature, the sample was studied at 281 K, 299 K, and 313 K, as shown in Figure 5.2.4.1. Increasing temperature causes a cathodic shift in the potential at which oxygenated species are adsorbed [106]. As the reduction peak is shifted more positively, the redox process is shown to be more reversible with increased temperature for this system [106]. This is an example of a small temperature change having a significant effect on the system. XRV scans at (0, 1, 0.5) were performed at the three different temperatures, as were hkscans along the <0.02, 1.02> direction, to investigate the effect of temperature on the Au(111)-(1x1) ↔ Au(111)-(px$\sqrt{3}$) transition. The results are summarized in Figures 5.2.4.1 and 5.2.4.2.

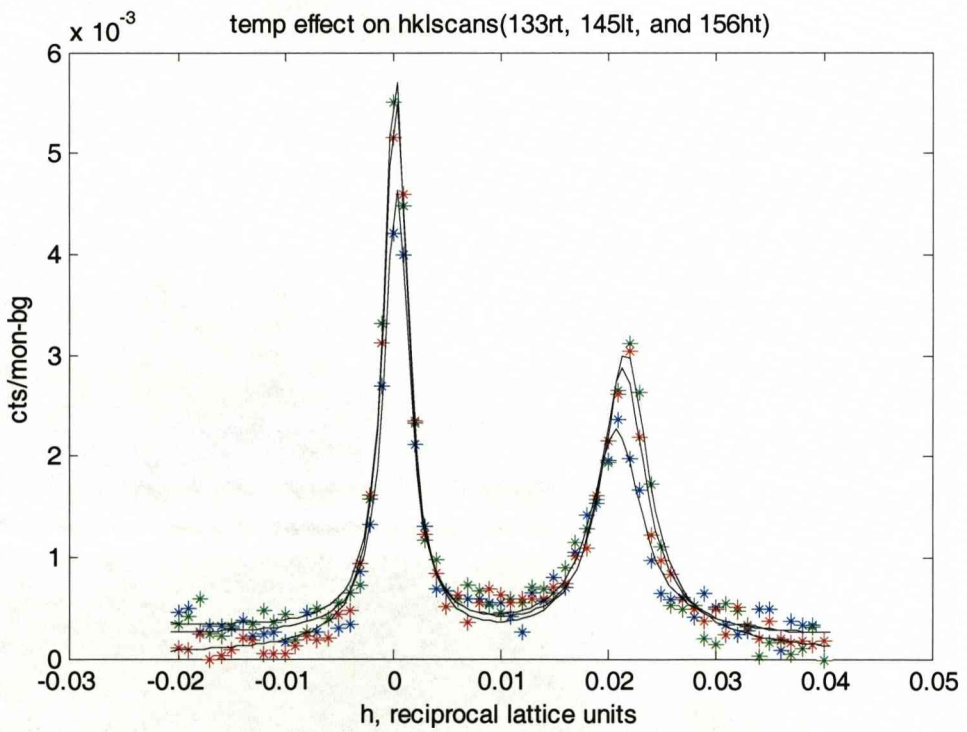

Figure 5.2.4.1: The effect of temperature on the hkscans. The black lines are double lorentzian fits on a sloping background. The background count was arbitrarily set to zero for clarity of comparison. (red = 313 K, green = 299 K, and blue = 281 K).

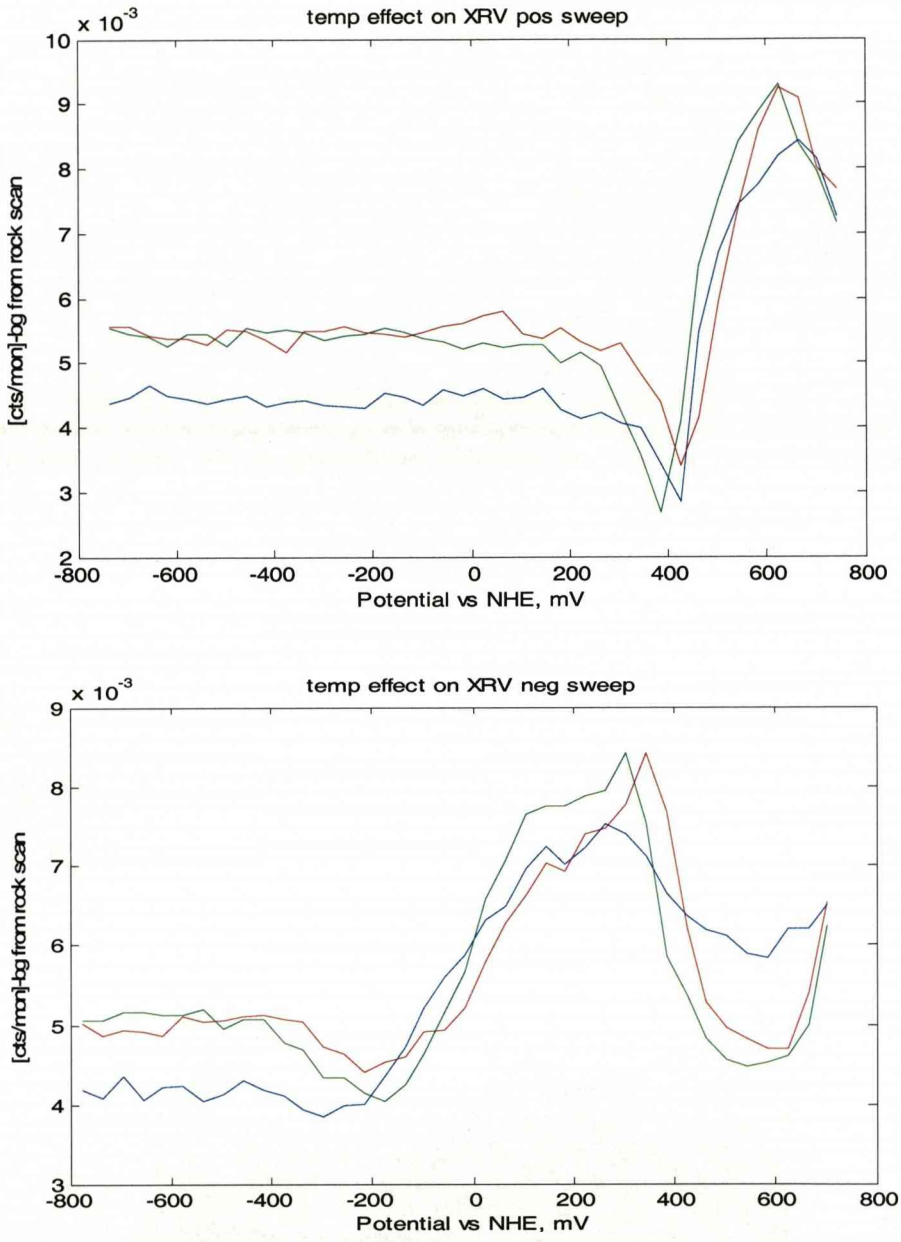

Figure 5.2.4.2: (Top) An XRV taken at (0, 1, 0.5) on Au(111) in 0.1 M KOH, during the positive sweep direction at three different temperatures (red = 313 K, green = 299 K, and blue = 281 K). The background count was deduced from rocking scans at the (0, 1, 0.5) position, and subsequently subtracted. (Bottom) Data from the corresponding negative potential sweeps.

From the hkscans in Figure 5.2.4.1 above, it appears that temperature is having a systematic effect on the formation of the reconstructed surface. From fitting the scans, it is shown that the integrated intensity, which represents the amount of the surface

that is reconstructed, is lowest at low temperature (LT = 281 K). There is no statistically significant difference between the measurements taken at room temperature (RT = 299 K) and high temperature (HT = 313 K). Also, the shift in the reconstruction peak position between temperatures (from fit data h = 0.0208 (281 K), h = 0.0217 (299 K), and h = 0.0214 (313 K), showed that, at the two highest temperatures, the surface was more compressed than at the lowest temperature. Although such differences were subtle they resulted in a p value of 23 for the RT and HT temperature data, but a p value of 24 at LT. The fitted peak widths show that at both RT and HT, the reconstruction domain size (in nearest neighbour units), D, was 31 compared to 28 at low temperature. On the negative potential sweep, the surface morphology is changing due to the reduction of reversible oxide formed at the positive limit, followed by the phase change to the (px$\sqrt{3}$) phase. Initially, the in-plane ordering is lost, and this is followed by an increase in surface ordering as the oxide layer is reduced and place exchange occurs. The resulting occupation of (px$\sqrt{3}$) sites is more in registry with the underlying (1x1) substrate than a random distribution, thus adds to the overall in-plane order. The effect of increasing the temperature seemed to be to improve the reordering kinetics, *i.e.* the peak in the XRV was less smeared at the two highest temperatures.

The total amount of reconstruction was significantly less at LT than that measured at either RT or HT. This is deduced from the integrated intensity of the rocking scans at the reconstruction position at the different temperatures (data not shown). This is likely to result from a combination of the kinetics of the system, coupled with the difference in the initial morphology of the surface before it reconstructs, due to the temperature effect on the redox process (see Figure 5.2.1.1).

On the positive potential sweep the data show no real differences as a function of temperature. At approximately 200 mV, the signal at (0, 1, 0.5) decreases as the atoms in the (px$\sqrt{3}$) sites start to move, which is believed to represent the in-plane order [111]. As these atoms begin to occupy (1x1) sites, there is a well defined increase in the surface ordering, up to a maximum value achieved at around 600 mV. The dip in intensity at potentials positive of this is attributed to the onset of surface oxide formation, which supports the previous comments made about the surface behaviour on the negative potential sweep. In considering the Au(111) reconstruction, it is important to note that the mass transfer is very limited in this process. That is, the compression factor is typically 24/23 = 4.4%, which is relatively small compared with metal reconstructions of other Au(hkl) surfaces. The next section focuses on a system involving a relatively large amount (~20%) of mass transport upon reconstruction, in an attempt to deduce any systematic differences/similarities between systems of (relatively) high and low mass transfer during reconstruction.

5.3 Au(100) Reconstruction - Experimental Results and Discussion

5.3.1 Cyclic Voltammetry

This section begins with a description of the cyclic voltammetry of Au(100) in base solution, emphasizing the importance of the temperature in governing the adsorption of oxygenated species. The nature of these species is still unresolved but, for the purpose of this discussion, the commonly accepted terminology is used; *i.e.*, the

reversible adsorption at $E \leq 0.95$ V corresponds to the formation of an OH adlayer while, at $E > 1.0$ V, irreversible processes (adsorption of OH/O accompanied by place exchange between Au and oxygenated species) correspond to bulk oxide formation [112]. Figure 5.3.1.1 shows that temperature has a relatively small effect on the reversible adsorption of OH. This small effect stems from the reversibility of this process; reversibility implies that the potential at which OH adsorbs is controlled by the free energy of OH adsorption and the latter quantity changes by only a very small amount over the temperature range of interest. For example, simple estimates from standard thermodynamic tables [113], neglecting temperature-induced free energy changes of adsorbed species, (which will be very small) show that a free energy change of ~0.01 eV is to be expected for a temperature change of 279 K to 319 K (see [114] for a discussion). In contrast, the irreversible bulk oxide formation/reduction becomes more reversible at higher temperatures; suggesting that, as for Pt single crystals [50], the temperature-induced changes above 1.0 V are kinetically driven. Notice also that the "reconstruction" peak at ~1.0 V is slightly more pronounced at higher temperature. Given that it has been suggested that this peak may serve as a fingerprint for the lifting of the surface reconstruction [115], this is the first indication that at higher temperature the surface has a higher coverage of the reconstruction.

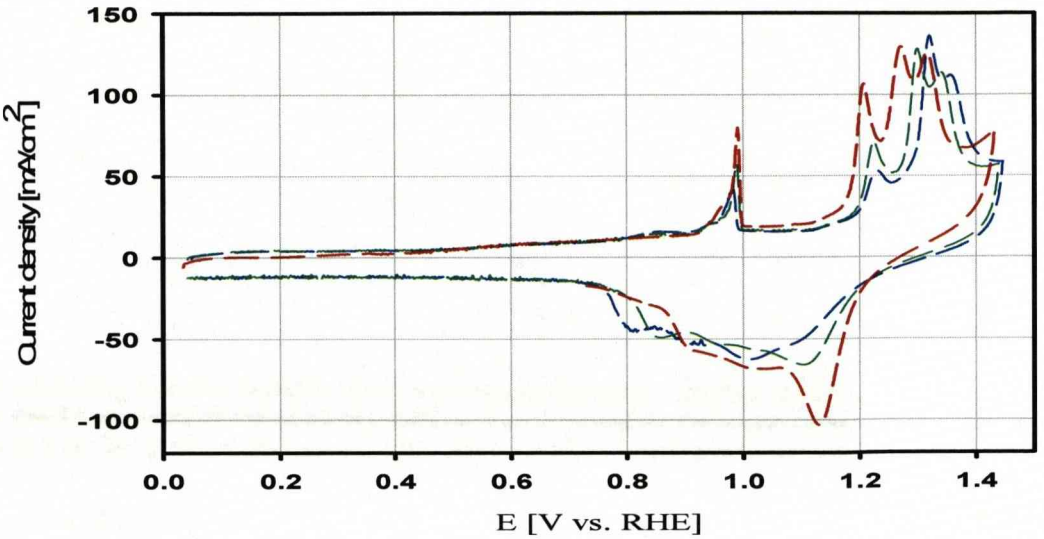

Figure 5.3.1.1: RDE measurements of Au(100) in 0.1 M KOH at 275 K (blue curve), 295 K (green curve) and 311 K (red curve.) showing three distinguished potential regions: (a) reversible adsorption of OH between $0.05 < E < 0.95$ V; (b) the "reconstruction" peak at ≈0.985 V and (c) irreversible oxide formation at $E \geq 1.0$V (sweep rate=5 mV s^{-1}.). The rotation speed was 1600 rpm.

5.3.2 The Effect of OH Adsorption on the "hex" ↔ (1x1) Transition

Detailed atomic-scale information on the surface restructuring is obtained by SXS, concentrating on electrode surfaces for which the potential has been cycled over the range for which the changes in the surface atomic structure are fully reversible, so as to avoid any influence of the *ex situ* surface preparation process on the observed results. Figure 5.3.2.1 shows the effect of temperature on the 'hex' reconstruction of Au(100) and the kinetics of the restructuring (inset):

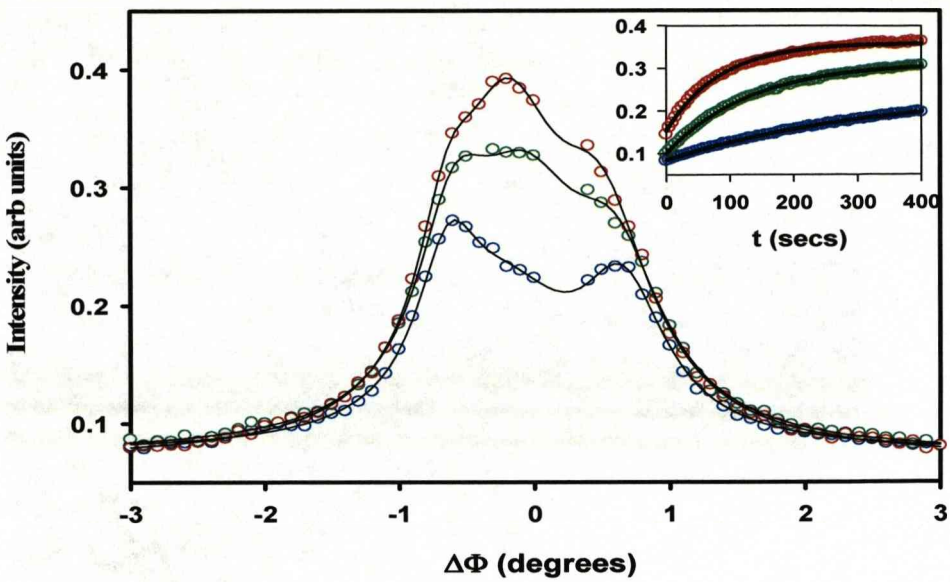

Figure 5.3.2.1: The SXS measured at (1.2, 1.2, 0.3), a position where scattering from the Au(100)-'hex' reconstruction is observed, measured in 0.1 M KOH at 279 K (blue data), 293 K (green data) and 319 K (red data). The [h, k] position of each peak was checked in each case with radial <h, k> scans. The solid lines are fits to the data according to a three-peak lineshape. The inset shows the time dependence of the reformation of the 'hex' reconstruction at 0.05 V after a potential sweep over the range 0.05 - 1.4 V with a sweep rate of 5 mV s^{-1}. The solid lines are fits to the data as described in the text.

Figure 5.3.2.1 shows rocking scans through the (1.2, 1.2, 0.3) reciprocal lattice position, where scattering from the 'hex' reconstruction is observed [116]. These measurements were performed after stabilizing the temperature and then performing several potential cycles over the range 0.05 V to 1.45 V, which leads to the lifting and reformation of the reconstruction, and then holding the potential at 0.05 V for ~ 30 minutes, at which point the intensity of the peak at each temperature had saturated. At low temperature the data are consistent with the presence of the rotated 'hex' phase. The fitted lineshape to the data indicates the presence of 2 peaks rotated by ± 0.65°. In the fit to the data a central (unrotated) peak was also included but the intensity of this central peak is negligible at low temperature. At higher temperature, however, the data indicate the presence of additional unrotated 'hex' domains (*i.e.* the central peak

is greatly increased in intensity whereas the rotated peaks are relatively unchanged), implying that at 295 K and 311 K the total coverage of the 'hex' reconstruction increases principally through the growth of unrotated 'hex' domains (Figure 5.3.2.1 – central peak intensity increases). The nature of the 'hex' reconstruction with regard to the issue of rotation is still not fully understood either in UHV or in electrochemistry. It was proposed that in UHV rotated domains are formed presumably due to energy minimization of an incommensurate overlayer, although simple models using the theory developed by Novaco-McTague fail to predict the observed rotation angles [119]. Nevertheless, the Au(100) reconstruction involves significant transport of surface Au atoms as the hexagonal reconstructed surface layer (on the underlying square bulk crystal lattice) has an atomic density that is ~ 20% greater than the (100) surface plane. The inset to Figure 5.3.2.1 shows how the kinetics of the long-range ordering (agglomeration of the so called strings [118]) in the "hex" reconstruction depend on the temperature of electrolyte. Fits of a $1-\exp\left(-\frac{t-t_0}{\tau}\right)$ form to these data (solid lines) indicate that the time constant, τ, for the slow formation of the reconstructed surface decreases significantly as the temperature is increased. Although it is not possible to rule out a more complex kinetic model on the basis of such a limited data set (for example, the existence of more than one time constant in the reordering process) using this simple model allows an activation energy for the diffusion process to be obtained. Assuming that the time constant should follow an $\exp(-E_a/kT)$ form, where E_a is the activation energy for diffusion and k is the Boltzmann constant. Calculating a linear fit to the data of $\ln(\tau)$ versus 1/T, gives an activation energy E_a=0.33±0.06 eV.

Importantly, in UHV the 'hex' phase exhibits domains that are also either rotated or unrotated with respect to the underlying Au lattice. However, the temperature window of stability of the rotated phase in UHV is much wider than in the electrochemical environment; an unrotated domain becomes predominant only at ~ 900 K, demonstrating that extremely high temperatures are needed to induce surface restructuring in UHV conditions [119]. The temperature effects on morphological changes of Au surface atoms in UHV appear, therefore, to be at odds with the electrochemical results in Figure 5.3.2.1. Although the transformation from rotated to unrotated "hex" domains in UHV and electrochemical environments is difficult to compare, it is apparent that the driving force for this process must be different in these two environments. In UHV the transformation from rotated to unrotated domains occurs directly as the temperature is increased whereas in the electrochemical environment the transformation only occurs after cycling of the electrode potential into the potential region of oxide formation. The behavior in the electrochemical environment therefore depends upon consideration of temperature effects on the kinetics of bulk oxide formation and reduction. It is this second process which probably controls the nature of metal "active sites" required for the development and propagation of the reconstructed phase. Although oxygenated species are not present on the surface in the reconstructed phase, they indeed play a role in the formation. It is interesting that recent results for the Au(100) surface in UHV have shown that the presence of oxygen leads to formation only of the non-rotated 'hex' phase [120]. To explore further the effect of bulk oxide formation on the results in Figure 5.3.2.1, Br was added to the electrolyte, as it is known to protect the gold surface effectively from oxide formation.

5.3.3 The Effect of Bromide Anions on the "hex" ↔ (1x1) Transition

The addition of bromide anions to 0.1 M KOH strongly affects the reconstruction of the Au(100) surface. During a cathodic potential sweep the changes in the Br_{ad} structure are fully reversible but the formation of the "hex" Au reconstruction then occurs from a surface that is free of Au adislands (Br_{ad} significantly increases Au diffusion on the surface so that the excess Au adatoms are incorporated at steps on the unreconstructed surface [121]). This leads to the formation of a well-ordered rotated "hex" phase although due to the lack of nucleation centres the timescale for formation is rather slow. The SXS results for the 'hex' reconstruction obtained in 0.1 M KOH + 0.01 M Br^- is shown in Figure 5.3.3.1.

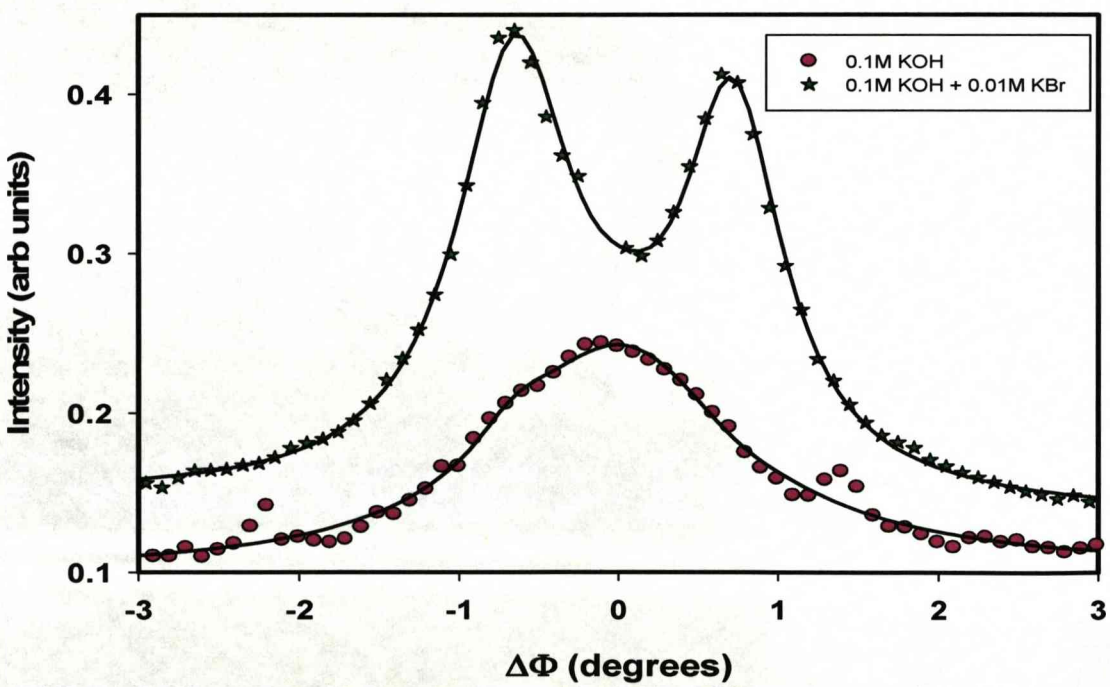

Figure 5.3.3.1: The SXS at (1.2, 1.2, 0.3), a position where scattering from the Au(100)-'hex' reconstruction is observed, measured in 0.1 M KOH + 0.01 M Br^- (star symbols) and 0.1 M KOH (circles) at room temperature (293 K).

The fitted lineshape to the data indicates the presence of two rotated peaks which are, in contrast to the results in Br-free electrolyte, much stronger and very stable (no unrotated domains are observed) between 275-311 K. It is therefore apparent that adsorbed Br^- acts to facilitate the formation of rotated "hex" domains. This effect may be understood in terms of combined effects of blocking of oxide formation by Br^- [112] and an increased gold surface mobility induced by chemisorbed Br^- which means that the reconstruction forms on a surface that has considerably fewer defects. Previous results have also indicated that the step-terrace morphology is also modified in Br-containing electrolyte [121]. Clearly the role of anions is significant in determining the mobility of surface Au adatoms with the resultant effect on the ordered surface. Interestingly, in this case, changing the temperature (again over the range 277 K– 313 K) has no effect on the structural behaviour, either the Br_{ad} structures (see below) or the Au reconstruction, that are observed. In contrast to the situation in 0.1 M KOH (where only OH adsorption/desorption occurs, which enhances the Au mobility) it appears, therefore, that the blocking of the surface by the anion species means that the anion-Au interaction fully determines surface ordering and temperature changes, in the range studied, play no active role. Thus it appears that temperature changes only affect the formation of the 'hex' reconstruction by the influence on bulk oxide formation, which in turn determines the morphology of the unreconstructed surface on which the reconstruction forms. We note here that in studies of the Au(100) surface reconstruction under conditions of Au homoepitaxy in the electrochemical environment, the timescale for formation of the reconstruction on the unreconstructed surface is very fast [122]. This is presumably due to the ready availability of excess surface Au adatoms *via* the deposition process. Furthermore, deposition of Au onto the reconstructed surface caused a transition from a rotated

'hex' phase to an unrotated phase [123]. It appears, therefore, that formation of the 'hex' reconstruction at high temperature (in our studies) is similar to the conditions observed in Au homoepitaxy, implying a strong dependence on the surface morphology and the mobility of Au adatoms. A definitive understanding of the nature of the 'hex' reconstruction both in UHV and the electrochemical environment awaits further study.

5.3.4 The Structure of Adsorbed Bromide on Au(100)

In Br^--containing electrolyte, lifting of the Au(100) reconstruction at room temperature is always accompanied by Br^- adsorption, resulting in the formation of a c($\sqrt{2}$x2$\sqrt{2}$) Br phase which undergoes a uniaxial compression as the potential is increased [124]. Figure 5.3.4.1 shows the temperature-dependent x-ray voltammetry data measured at (1, 0.5, 0.1), where scattering due to the commensurate c($\sqrt{2}$x2$\sqrt{2}$) Br phase appears. While in the positive potential sweep direction the ordering of the Br^- adlayer (*i.e.* due to adsorption of Br from solution) is temperature dependent (Figure 5.3.4.1 indicates slower ordering at low temperatures), in the negative potential sweep direction the ordering of the commensurate phase (in this case due to desorption of Br from the incommensurate structure) is almost temperature independent. We conclude, therefore, that the temperature-induced hysteresis in intensity shown in Figure 5.3.4.1 is, in fact, a temperature-controlled surface mobility of adsorbed anions and thus only the kinetics of formation of the c($\sqrt{2}$x2$\sqrt{2}$) Br phase are affected by temperature changes. This was confirmed by equilibrium studies of the ordered Br phase (rocking scans at fixed potentials) in which the SXS spectra from the Br phase at each potential were measured after waiting for several minutes. These data unambiguously showed that temperature only affects the kinetics of the ordering

as identical results were obtained in the equilibrium studies in both the anodic and cathodic sweep directions.

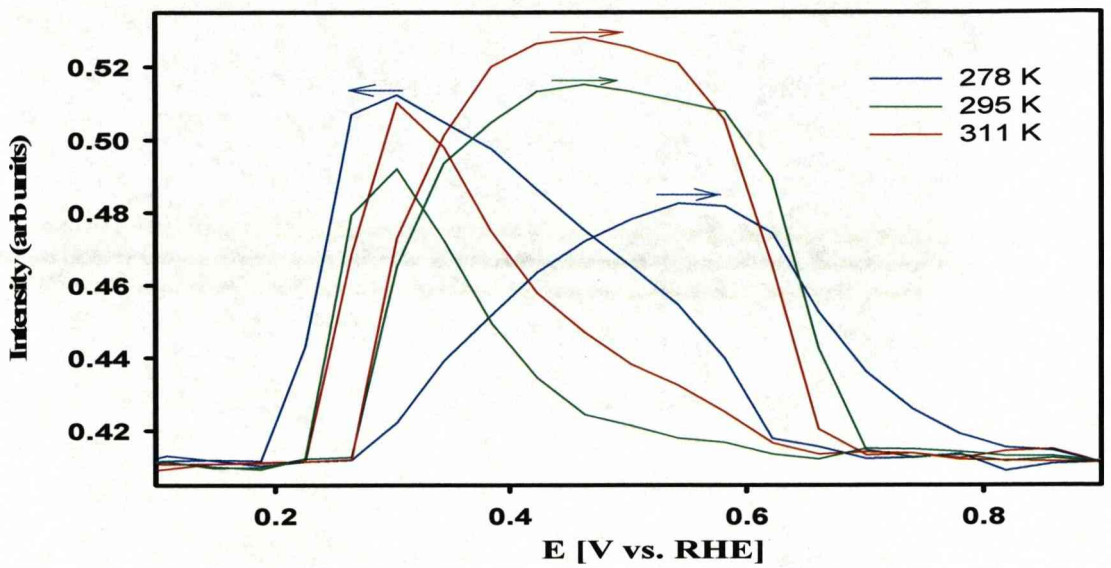

Figure 5.3.4.1: X-ray voltammetry (XRV) measured at (1, 0.5, 0.2), a position where scattering from the commensurate Br-c($\sqrt{2}$x2$\sqrt{2}$) structure is observed, for Au(100) in 0.1 M KOH + 10^{-2} M KBr electrolyte. The arrows indicate the sweep directions and the data were measured at 279 K (blue data), 293 K (green data) and 319 K (red data). The sweep rate was 5 mV s^{-1}.

It can thus be concluded that the effect of temperature on the structures and phase transitions of adsorbed anion adlayers is negligible.

5.4 Summary

In this Chapter, I have presented results which probe the behaviour of the reconstructions of two of the low index gold faces in 0.1 M KOH. The effects of potential and temperature have been discussed. Both surfaces show changes in the reconstruction behaviour due to small temperature changes. The Au(111) surface reconstruction was shown to have some temperature dependency, in that both the

stripe separation p, and the reconstruction domain size D, were different at low temperature compared to both room and high temperature.

For the Au(100) reconstruction, which involves greater mass transport, the effects have been more pronounced. The unrotated hexagonal reconstruction was shown to change dramatically over the small temperature range probed, and this is believed to be due to a "pinning" effect of the surface oxide formed at positive potentials [125]. By introducing Br^- anions, which inhibit oxide formation, the unrotated phase was significantly suppressed. This supports the given explanation that the unrotated phase does indeed originate from surface oxide. The concluding results from this Chapter, which shows that there is no temperature effect on the adsorption of anion layers, or their ordering, is crucial to the work on CO/Pt systems which follows in Chapter 6.

Chapter 6

The Effects of Temperature on the Pt(111)/CO interface

6.1 Introduction

The previous Chapter suggests that unreactive adsorbates are not strongly affected by the temperature changes. It is important, however, to extend the study to ordered adsorbates that can react on the surface. A unique system in this respect is the ordering of a CO adlayer on Pt(111), where the presence of the CO adlayer structures can be followed in detail by SXS [34, 57, 127]. In previous work [50, 57, 128], it was proposed that a potential-driven phase transition occurs due to small, yet clearly discernable, oxidation of the CO adlayer. This reversible p(2x2)-3CO (surface coverage, Θ_{CO} = 0.75 ML) ↔ ($\sqrt{19}$x$\sqrt{19}$)R23.4°-13CO (Θ_{CO} = 0.68 ML) transformation in the CO adlayer has been shown to be driven by interaction of CO_{ad} and oxygenated species (denoted hereafter as OH [129]) although there is evidence from FTIR studies that the transformation also occurs if CO is removed from solution at 0.05 V [130]. Note that the structures are hereafter abbreviated as (2x2) and $\sqrt{19}$, respectively.

6.2 Surface Preparation

This Chapter begins with a qualitative discussion regarding the effects of surface preparation. After annealing the Pt(111) sample with an RF heater, it is cooled in argon gas. STM studies of this "as prepared" surface have been performed, and are shown in Figure 6.2.1 below [131].

The cycling procedure described in Figure caption 6.2.1 above is termed "CO-annealing", and provides a surface comprising Pt(111) terraces with long range order. The final stepped surface can actually be prepared by cycling (in the presence of CO) to 0.75 V (as opposed to 0.95 V, which causes bulk oxidization of CO from the surface), but many more potential cycles are required. This demonstrates how the potential prehistory determines surface morphology and activity. By performing this surface CO annealing procedure before the temperature based x-ray measurements are performed, a clean surface that is largely free of defects is produced. That is, after the CO annealing process it is assumed that a surface with good long range order, similar to that shown in Figure 6.2.1(c), is present.

The cycling procedure described in Figure caption 6.2.1 above is termed "CO-annealing", and provides a surface comprising Pt(111) terraces with long range order. The final stepped surface can actually be prepared by cycling (in the presence of CO) to 0.75 V (as opposed to 0.95 V, which causes bulk oxidization of CO from the surface), but many more potential cycles are required. This demonstrates how the potential prehistory determines surface morphology and activity. By performing this surface CO annealing procedure before the temperature based x-ray measurements are performed, a clean surface that is largely free of defects is produced. That is, after the CO annealing process it is assumed that a surface with good long range order, similar to that shown in Figure 6.2.1(c), is present.

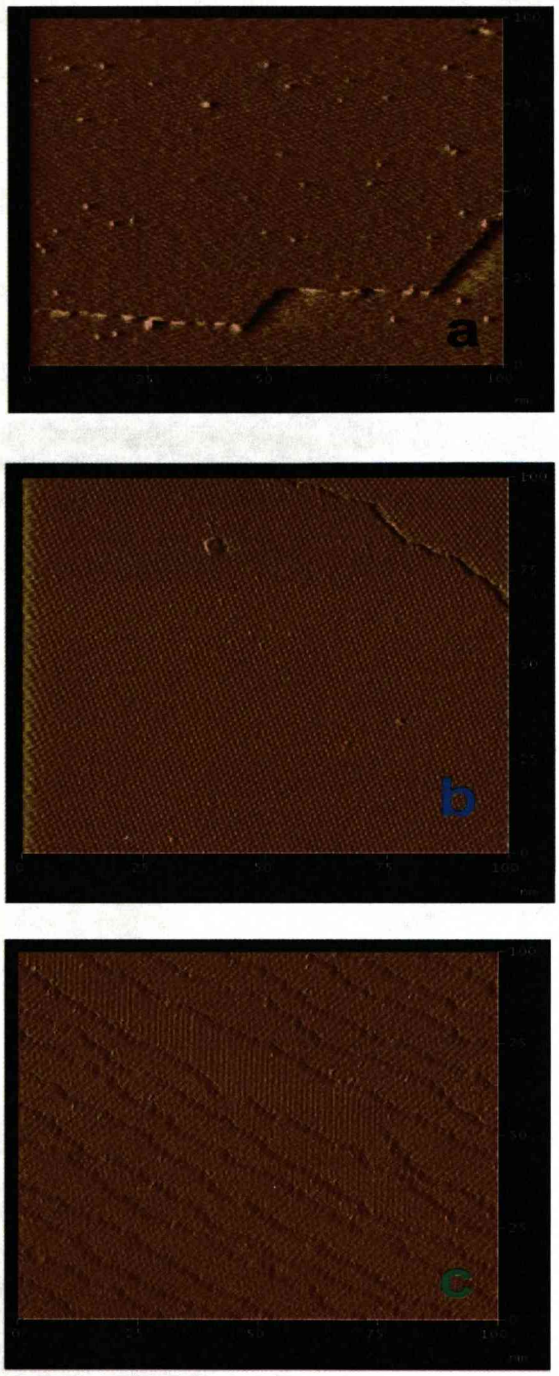

Figure 6.2.1: STM images of the Pt(111) surface in $HClO_4$, in the presence of CO. Panel (a) shows the as prepared surface (, (b) the surface after 20 potential cycles to 0.75 V, and (c) after 20 cycles to 0.95 V. The sweep rate was 50mv s^{-1}, and the negative limit for the sweeps was 0.05 V – the CO saturated electrolyte was equilibrated at this potential in these experiments. Taken from reference [8].

6.3 Experimental Results

The structure of CO on Pt(111) at ambient temperature has been studied previously, showing that it can exist in two phases, the (2x2) phase and the √19 phase, depending on surface potential [57, 127]. The x-ray measurements performed were considerate of the importance played by the potential prehistory on the electrode surface, and thus systematically probe the temperature dependent behaviour of the CO structures at non ambient temperatures.

A description of Figure 6.3.1 (see below) provides a useful introduction to the effect of temperature on the structure of adsorbed CO on Pt(111) found during these experiments: **(a)** Polarization curves indicating the temperature-controlled CO oxidation reaction in the pre-ignition potential region and at the ignition potential. **(a')** Enlargement of the pre-ignition region showing enhanced CO oxidation at higher temperatures. **(b)** XRV measured at a CO-p(2x2) peak (only anodic sweeps are shown) as a function of temperature. **(b')** the integrated intensity (open symbols-arb. units) and domain size (closed symbols, units are nm) of the CO-p(2x2) structure measured at 0.05 V as a function of temperature. **(c)** XRV measured at a CO-√19 peak (only anodic sweeps are shown) as a function of temperature. (c') the integrated intensity (open symbols-arbitrary units) and domain size (closed symbols, units are nm) of the CO-√19 structure measured at 0.9 V as a function of temperature. Note that at 319 K the p(2x2) and √19 structures are coexistent at 0.05 V whereas at 279 K the structures are coexistent at 0.9 V. Red data correspond to data measured at 319 K, green data at 293 K (room temperature) and blue data at 279 K. All of the results were

obtained after several cycles of the electrode potential over the full potential range shown.

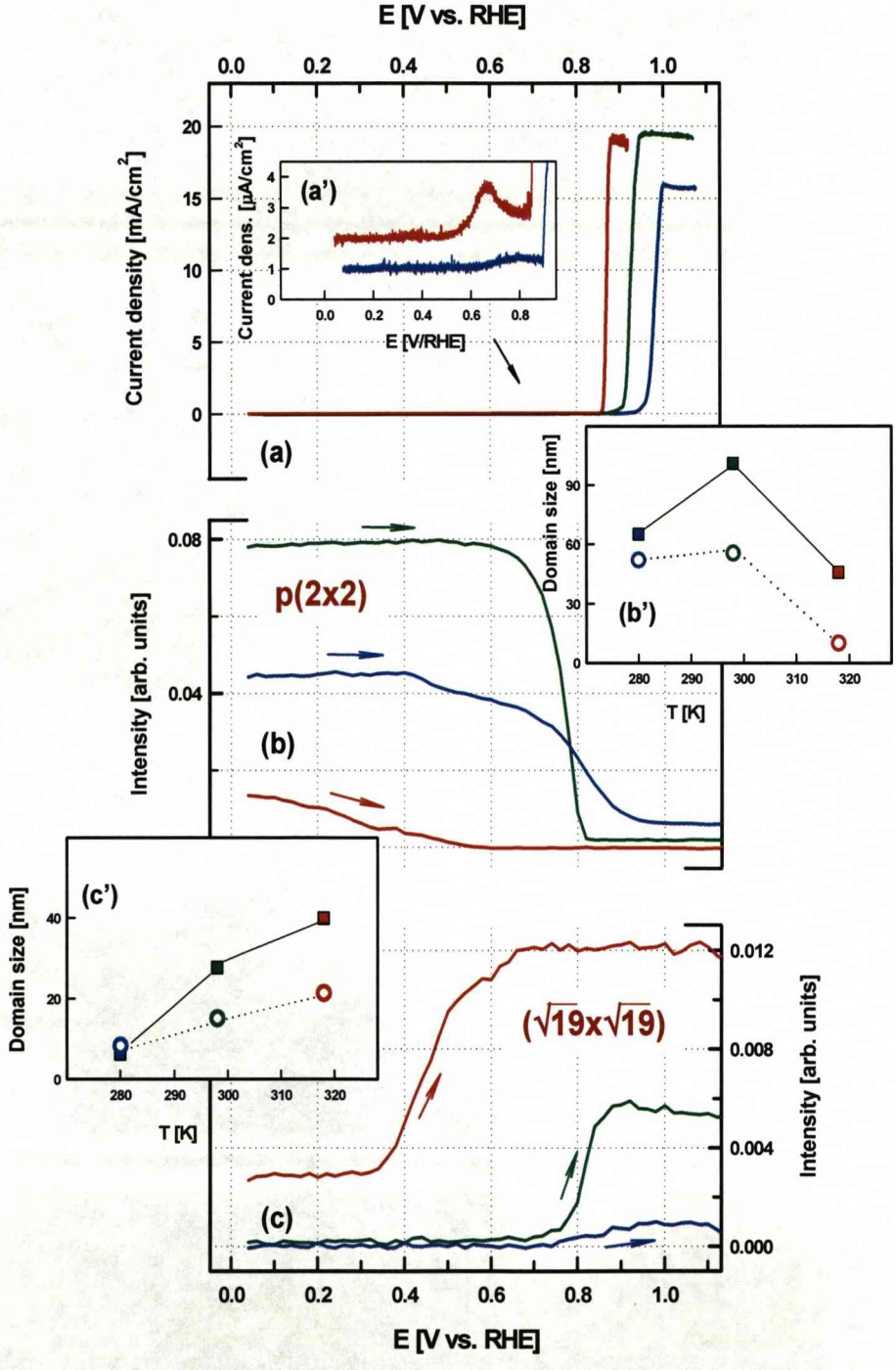

Figure 6.3.1: *Experimental data illustrating the temperature effect on CO adsorbed on Pt(111). See text for full details.*

Figure 6.3.1 shows the dramatic effect that a small temperature change has on the (2x2)↔√19 phase transformation in 0.1 M $HClO_4$. In particular, the transition is shifted by ~ 0.5 V as a result of only a 20 K change in temperature. The (2x2)↔√19 phase transformation is triggered by CO oxidation, which can be observed in the so-called pre-ignition region between 0.4 V and 0.7 V (Figure 6.3.1(b')). Figure 6.3.1 also shows that there is a negative shift in the ignition potential for CO oxidation as the temperature is increased. Figures 6.3.1(b) and 6.3.1(c) show the x-ray voltammetry (XRV) data for the (2x2) and √19 structures at the three different temperatures. Fits to the rocking curves through the (1/2, 1/2) and (3/19, 14/19) CO reflections (measured at l=0.2) were obtained after potential cycling over the range 0.05-1.2 V and then holding at the fixed potential for ~5 minutes.

Figures 6.3.1(b') and 6.3.1(c') show the integrated intensities and domain sizes (inversely proportional to the widths of the diffraction peaks) as a function of temperature for both CO structures. From these data it is apparent that the ordering of the p(2x2)-3CO structure is frustrated under both "cold" (280 K) as well as "hot" (319 K) conditions. The fact that the integrated intensities and the widths of the (2x2) peaks show a "volcano" relationship with the temperature of electrolyte may indicate that the balance between the rate of CO ordering and the surface coverage by OH (rate of CO oxidation) reaches a maximum at room temperature (293 K). Note also that the potential window of stability of the (2x2) structure (Figure 6.3.1(b)) decreases significantly by increasing the temperature, reflecting the negative shift in the onset of OH. In contrast to the (2x2) structure, the ordering of the √19 structure (*i.e.* coherent domain size) increases linearly by increasing the temperature (from 4.7 nm at 279 K to 40 nm at 319 K). This may be due to the enhanced mobility of CO as the temperature increases which allows for the formation of larger domains of a structure

which has a large unit cell. Most importantly, it can be seen that at 319 K (Figure 6.3.1(c)) the √19 phase exists even at the onset of the hydrogen evolution reaction (at ~0.05 V) and is coexistent with the (2x2) phase. The coexistence between the (2x2) and √19 structures at intermediate CO coverage has also been inferred from FTIR spectroscopy [132] although these results were obtained in solution free of CO where it is possible to control the CO coverage. It is important to re-emphasize that all of the data presented here were measured after potential cycling at each temperature. After changes to the temperature the first potential sweep is typically not representative of equilibrium conditions; for example, raising the temperature from 293 K to 319 K whilst holding at 0.05 V leads to little change in the intensity of the (2x2) peak. It is only upon cycling the potential that the transformation to the mixed (2x2)/√19 phase at 0.05 V (319 K) is observed. This also indicates that the temperature effects can be attributed to a kinetic rather than a thermodynamic driving force.

Given that in CO-saturated solution at ambient temperatures and at low overpotentials (~0.05 V) only the (2x2) has been observed, the question naturally arises as to what the driving force is for the transformation to the coexisting √19 structure when the temperature is increased. Resolving this question could provide the fundamental understanding necessary to develop CO oxidation catalysts of superior activity. As discussed previously, the rate of CO electrooxidation is a complex interplay between the adsorption and re-adsorption of CO and oxygenated species, diffusion of co-adsorbed CO and OH, and the kinetics of the reaction between CO and oxygenated species [12]. Although all of these factors may simultaneously contribute to the (2x2)↔√19 transition in Figure 6.3.1, we propose that the major effect arises through the temperature-enhanced reactivity of the oxidative removal of CO.

6.4 The Effect of Bromide Anions

To confirm the above hypothesis, Br^- anions were added to the electrolyte because below ≈1.0 V Br anions cannot displace CO from the surface. However, Br will successfully block the adsorption of OH; the free energy of specific bromide anion adsorption at standard conditions and room temperature on Pt(111) is found, using DFT calculations performed by J.P. Greeley (Argonne National Laboratory), to be 0.7 eV more negative than that of OH. We also note that temperature has a negligible effect on Br adsorption; as was the case with Au(100)-Br, SXS results for the Pt(111)-Br system revealed that temperature changes affect neither Br^- ordering nor the surface coverage by Br^-. It thus might be expected that, as Br and OH are in competition for Pt adsorption sites, the presence of adsorbed Br may prevent the temperature effect observed in Figure 6.3.1 by blocking the adsorption of OH which is required for the oxidative removal of CO and drives the (2x2)↔√19 transition.

Identical experiments for the Pt(111)-CO system to those shown in Figure 6.3.1 were performed in 0.1 M HClO4 to which 0.01 M Br- had been added and the solution was being purged continuously with CO. The results are summarized in Figure 6.4.1 obtained at room temperature (blue curves, 293 K) and at 319 K (red curves). The XRV results at the CO-(2x2) and CO-√19 positions are shown for the anodic sweeps only in the top and bottom panels of Figure 6.4.1 respectively. The central panel shows the corresponding polarization curves for CO oxidation with the inset showing a blow-up of the pre-oxidation region (0.5 V – 0.9 V). All of the results were obtained after several cycles of the electrode potential over the full potential range shown. Unlike the results obtained in the absence of Br- anions (Figure 6.3.1), raising the temperature does not change the coverage of the CO-(2x2) adlayer at

negative potential (0.0 V) and, correspondingly, there is no signal from the √19 structure at this potential. This implies that, consistently with the DFT results, the adsorption of oxygenated species, necessary for oxidation of CO via the Langmuir-Hinshelwood mechanism, is blocked by the Br- anions. The pre-oxidation of CO is still shifted cathodically as the temperature is increased, as shown by the pre-oxidation peak in the polarization curves (inset) and the shift in the (2x2)↔√19 transition measured by XRV. Interestingly at positive potentials (1.2 V) the √19 structure disappears (in contrast to the results shown in Figure 6.3.1 obtained in pure perchloric acid). This implies that the CO is replaced by Br- anions at this potential and highlights the balance between the relative adsorption strengths of CO, oxygenated species and the spectator Br- anions in determining the reaction pathways.

The results summarized in Figure 6.4.1 unambiguously show that in solution containing Br, temperature does not drive the transformation in the CO adlayer as the active sites for adsorption of oxygenated species are blocked by the spectator anions, Brad, and these spectator anions are unaffected by temperature changes Therefore, the observed differences in Figure 6.3.1 can be explained through the temperature-controlled CO oxidation rates which are, at this potential, thermodynamically accessible but, at lower temperatures, hindered by reduced reactivity of OH, including both OH adsorption and reaction with CO.

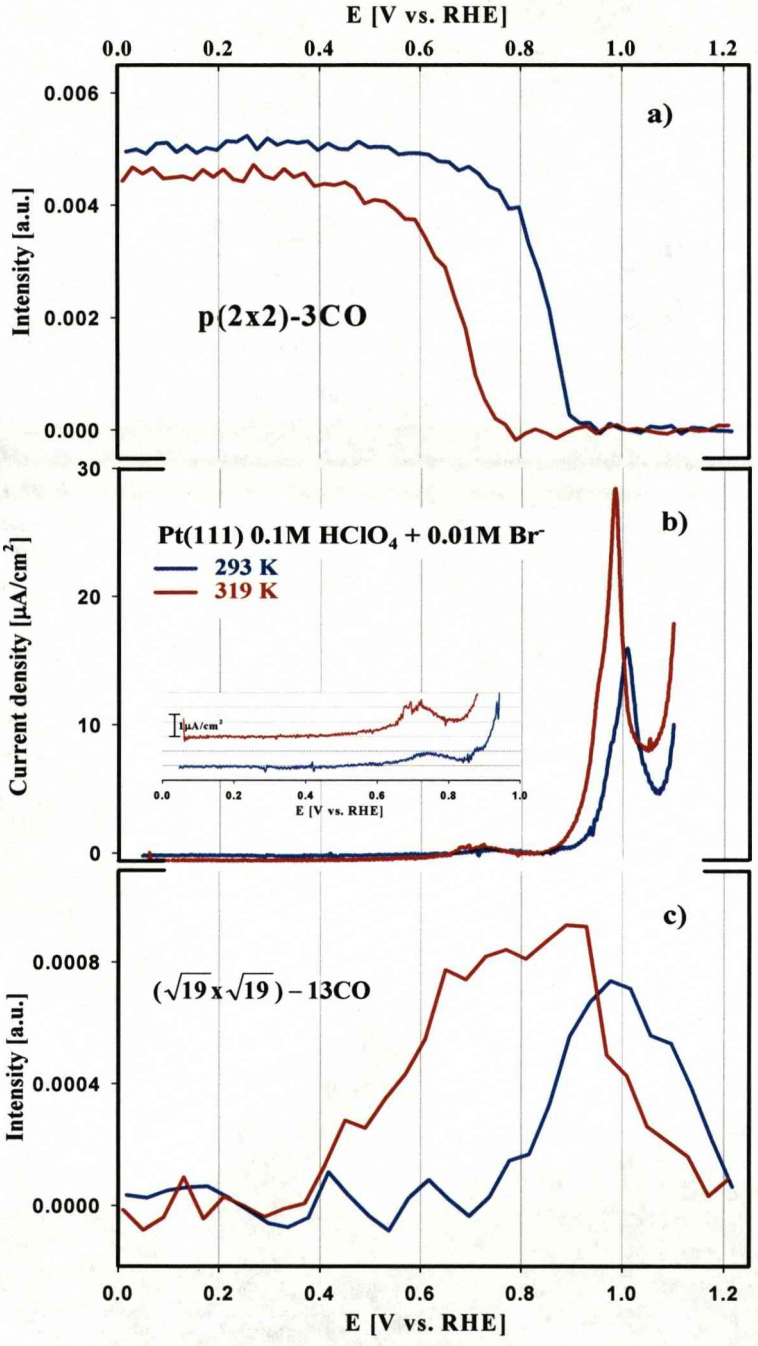

Figure 6.4.1: Temperature effects on the structure and oxidation of CO on the Pt(111) electrode in 0.1 M $HClO_4$ + 0.01 M KBr measured at 293 K (blue curves) and 319 K (red curves). (**a**) XRV measured at a CO-p(2x2) peak. (**b**) Polarization curves. Inset is an enlargement of the pre-ignition region. (**c**) XRV measured at a CO-$\sqrt{19}$ peak. (only anodic curves are shown). The sweep rate for both the electrochemical and SXS measurements was 2 mV s^{-1}. All of the results were obtained after several cycles of the electrode potential over the full potential range shown.

6.5 Summary

In this Chapter, we have demonstrated that small temperature changes can have dramatic effects on the structure and reactivity of electrochemical interfaces. The molecular-level mechanisms responsible for these temperature-induced changes range from increases in the mobility and oxide place exchange of metal surface atoms to reactivity-induced phase transitions in adsorbate overlayers. This was previously illustrated by a detailed study of the potential-induced 'hex' reconstruction of Au(100), in which the nature of the reconstructed surface depends on the temperature effect both on surface Au adatom mobility and on reversible oxide formation, the latter process determining the morphology of the surface on which the reconstruction nucleates. Spectator species (bromide anions), both the potential dependence of adsorption/desorption and the equilibrium ordering in the bromide adlayer, were found to be unaffected by temperature. Theoretical calculations support these results and indicate that the observed temperature effects in all systems are not driven by thermodynamics. In the case of reactive species, the example presented being CO adsorbed onto Pt(111), a strong temperature effect was observed on the ordering in the CO adlayer that is dependent on the adsorption of oxygenated species. The temperature results therefore suggest that the main effects are on the kinetics of oxide formation, the activation of water and the adsorption of oxygenated species. We believe that these results open up new opportunities to establish correlations between temperature, structure, and surface reactivity that will be important for the future development of efficient energy conversion systems. The results also form a first step in developing a fundamental understanding of the reactions in many electrochemical systems that operate at non-ambient temperatures.

Chapter 7

Concluding remarks

The experiments presented in this thesis provide examples of the detailed level of surface characterisation available using *in situ* synchrotron radiation x-ray scattering experiments. It was shown in Chapter 4 how such experiments can be utilised, in conjunction with a portable UHV transfer chamber (TRECXI), to investigate changes at the interface caused by adsorbates which are known to interact weakly with x-rays. In Chapters 5 and 6, by monitoring key reciprocal lattice positions, it was shown that the effect of temperature on potential induced structural changes at the interface can be probed. Examples of surface reconstructions, unreactive adsorbates, and reactive species have all been presented, highlighting the flexibility of the x-ray imaging techniques. The complimentary CV and RDE measurements provide a great deal of information, and have been used to support explanations of the x-ray measurements in numerous instances.

By utilising the capabilities of the TRECXI chamber, it was shown that the presence of the water layer caused a change in the interface structure, as inferred from the ratio data set presented in Figure 4.3.2.1. An in-plane ordered water structure was not detected, even though various high symmetry crystallographic directions were probed. However, given the weakness of the scattered signal from the p(2x2) oxygen layer, coupled with the background signal level, this is not surprising. At a potential of -1 V, the CTR profiles indicate that there is an outward relaxation of the topmost Pt layer by ~ 2.2% of the bulk layer spacing, due to adsorbed hydrogen. This is in excellent agreement with previous measurements on this system [93]. Figure 4.3.3.3 shows

systematic structural changes caused by the adsorption of OH on the surface, but this data could not be modelled accurately with the simple model proposed. These initial studies have significant scope for expansion, and highlight the intricate details the experimental techniques demonstrated can unearth.

Chapter 5 presented results showing the effect of temperature on the surface reconstruction of two low index Au samples in 0.1 M KOH. The Au(111) – (px$\sqrt{3}$) reconstruction was presented first, as an example of a system with relatively little mass transport occurring during the phase change. It was clear that temperature had an effect on the surface, as the reconstructed phase formed at low temperature had a smaller average domain size, and was less compressed, compared to the data measured at room and high temperatures. Following this, the Au(100) surface reconstruction was probed, which is known to involve much more mass transport during the formation of the hex phase (typically 20% compared with 4.4% for the Au(111) reconstruction). Here, it was suggested that the effect of temperature on surface oxide formation was linked to the behaviour of the reconstruction, in that at higher temperature there was more surface oxide to be "pinned" to the surface, thus giving rise to the unrotated domains. This theory was probed by the introduction of bromine anions, which inhibit surface oxide formation. The resulting lack/suppression of the unrotated phase with bromine present suggests this could well be the case.

In Chapter 6, a reactive adsorbate was probed, in the form of adsorbed CO molecules on a Pt(111) substrate. The complex relationship between temperature and the ordered CO layer was explained in terms of a complex interplay between the adsorption and re-adsorption of CO and oxygenated species, diffusion of co-adsorbed CO and OH, and the kinetics of the reaction between CO and oxygenated species. By introducing unreactive bromine anions, it was shown that the temperature effect could

be frustrated. As bromine anions are blocking the adsorption sites for OH^-, they frustrate the temperature effects seen previously in the bromine free system.

These results provide an insight into both the behaviour of the discussed systems, and also the capabilities of the techniques from an imaging perspective. Gathering detailed information about the electrified solid/liquid interface is a challenging process experimentally, especially when temperature effects are to be considered also. It was interesting that such small temperature changes had such marked effects, and how the effect of light elements on the interfacial structure could still be inferred from the CTR profiles even though the elements themselves could not be imaged. Further experiments on all of these systems will undoubtedly be performed, as they constitute both an interesting and commercially relevant area of research. This should facilitate a more detailed understanding of both the systems discussed and electrode/electrolyte interfaces generally.

Bibliography

1. M.G. Sammant, et al., J. Phys.Chem., 92 (1988): p. 220.
2. M.G. Sammant, et al., Surf. Sci, 1988. L29: p. 193.
3. *Nature Insight Materials for clean energy. Nature*, 2001. 414: p. 331-377.
4. *Sustainability and Energy. Science*, 2007. 315: p. 733-870.
5. C. A. Lucas and N. M. Markovic, , *Advances in Electrochemical Science and Engineering. Wiley VCH*, 2006.
6. *Solid-liquid Interfaces. Springer Verlag*, 2002.
7. D. M. Kolb, *Prog. Surf. Sci*, 1996. 51: p. 109-173.
8. M. F. Toney, et al., *Nature*, 1994. 368: p. 444-446.
9. S. Huemann, et al., *J. Phys. Chem. B*, 2006. 110: p. 24955-24963.
10. C. A. Lucas and N. M. Markovic, , *In-Situ Spectroscopic Studies of Adsorption at the Electrode and Electrocatalysis Elsevier*, 2007.
11. V. R. Stamenković, et al., *Science*, 2007. 315: p. 493-497.
12. F. U. Renner, et al., *Nature*, 2006. 439.
13. I. K. Robinson, Phys. Rev. B, 1986(33).
14. R. Feidenhans'l, Surf. Sci. Reports, 1989(10).
15. P. H. Fuoss and S. Brennan, Annu. Rev. Mater. Sci,, 1990(20): p. 360.
16. J. Clavilier, J. Electroanal. Chem, 1980. 107.
17. N. M. Markovic, et al., J. Electroanal. Chem, 1986. 241: p. 309.
18. L. A. Kibler, et al., J. Electroanal. Chem., 2000(484): p. 73-82.
19. Y. S. Chu, I. K. Robinson, and A. A. Gewirth, Phys. Rev. B, 1997. 55: p. 7945.
20. O. M. Magnussen, et al., J. Phys. Chem, 2000(104): p. 1222.
21. P. A. Thiel and P. J. Estrup, *CRC Handbook of Surface Imaging and Visualization.* CRC Press, Boca Raton, 1995.
22. G. A. Somorjai and M. A. Van Hove, Progress in Surface Science, 1989. 30: p. 201.
23. G. A. Somorjai, *Introduction to Surface Chemistry and Catalysis.* John Wiley & Sons, New York, 1993.

24. R. I. Masel, *Principles of Adsorption and Reaction on Solid Surfaces.* John Wiley & Sons, 1996.
25. M. A. Van Hove, in Landolt-Boernstein (Ed.), Physics of Covered Solid Surfaces, 1999.
26. J. Greeley, J. K. Norskov, and M. Mavrikakis, Annual Review of Physical Chemistry, 2002. 53: p. 319-348.
27. See reference [1].
28. B. M. Ocko, et al., Phys. Rev. Lett, 1990. 65: p. 1466-1469.
29. I. M. Tidswell, N. M. Markovic, and P. N. Ross, Phys. Rev. Lett, 1993. 71: p. 1601-1604.
30. M. F. Toney and B. M. Ocko, *Synch. Rad. News*, 1993. 6: p. 28-33.
31. I. M. Tidswell, N. M. Markovic, and P. N. Ross, J. Electroanal. Chem, 1994. 376: p. 119-126.
32. N. M. Markovic and P. N. Ross, Surf. Sci. Reports, 2002. 45: p. 117-230.
33. C. A. Lucas and N. M. Markovic, in Ernesto J. Calvo (Ed.),The Encyclopedia of Electrochemistry, volume 2, section 4.1.2.1.2., Wiley-VCH, 2004.
34. J. Wang, et al., J. Phys. Chem, 2005. 109: p. 24-26.
35. W. Haiss, et al., J. Electroanal. Chem, 1998. 452: p. 199.
36. R. J. Nichols, et al., Surf. Sci, 2002. 263: p. 513.
37. K. M. Ho and K. P. Bohnen, Phys. Rev. Lett, 1987. 59.
38. J. K. Norskov, Surf. Sci, 1994. 299: p. 690.
39. J. Wang, et al., Science, 1992. 255: p. 1416-1418.
40. I. M. Tidswell, N. M. Markovic, and P. N. Ross, Surf. Sci, 1994. 317: p. 241-252.
41. O. M. Magnussen, *Chem. Rev*, 2002. 102: p. 679-726.
42. B. B. Blizanac, et al., J. Phys. Chem, 2003(108): p. 625-634.
43. B. M. Ocko, J. Wang, and T. Wandlowski, Phys. Rev. Lett, 1997. 79: p. 1511.
44. D. W. Suggs and A. J. Bard, J. Phys. Chem, 1995. 99: p. 8349.
45. C. M. Vitus, et al., J. Phys. Chem, 1991. 95: p. 7559.
46. K. Sashikata, et al., J. Chem. Phys, 1996. 100: p. 20027.
47. B. M. Ocko, et al., Phys. Rev. B, 2003. 53: p. 7654-7657.
48. R. J. Nichols, in J.Lipkowski and P.N.Ross (Eds.), Adsorption of Molecules at Metal electrodes, VCH Publisher, Inc., New York, 1992, Ch. 7.

49. C. Korzeniewski, in A.Wieckowski (Ed.), Interfacial Electrocehmistry-Theory, Experiment and Applications, Marcel Dekker, Inc, New York-Basel, 1999, Ch. 20.
50. N. M. Markovic, et al., J. Phys. Chem. B, 1999. 103: p. 487-495.
51. N. P. Lebedeva, et al., J. Electroanal. Chem, 2000. 487: p. 37-44.
52. N. P. Lebedeva, et al., J. Phys. Chem. B, 2002. 106: p. 9863-9872.
53. I. Villegas and M. J. Weaver, *J. Chem. Phys*, 1994. 101: p. 1648.
54. K. Yoshima, M. Song, and M. Ito, Surf. Sci, 1996. 368: p. 389.
55. N. M. Markovic, in W. Vielstich, A. Lamm and H. A. Gasteiger (Eds.), Handbook of Fuel Cells; Fundamentals, Technology and Application, p368-393, John Wiley & Sons Inc., 2003.
56. I. Villegas, X. Gao, and M. J. Weaver, Electrochim. Acta, 1995. 40: p. 1267-1275.
57. C. A. Lucas, N. M. Marković, and P. N. Ross, *Surf. Sci.*, 1999. 425: p. L381-L386.
58. N. M. Markovic, et al., Surf. Sci, 2002. 499: p. L149-L158.
59. A. J. Bard and L. R. Faulkner, Electrochemical Methods, Wiley & Sons, New York, 1980.
60. C. A. Lucas, et al., Surf. Sci, 2000. 448: p. 65-76.
61. C. A. Lucas, N. M. Markovic, and P. N. Ross Jr., Surf. Sci, 2000: p. 77-86.
62. N. M. Markovic, et al., Langmuir, 2000. 16.
63. K. Itaya, *Prog.Surf. Sci*, 1998. 58: p. 121-24.
64. *for a discussion, see V. A. Marichev, Surf. Sci. Rep. 2005, 56, 277-324.*
65. M. Labayen and O. M. Magnussen, *Surf. Sci,*, 2004. 573: p. 128-139.
66. A. C. Fisher, *Electrode Dynamics.* Oxford University Press, 1996.
67. A. W. Bott, Curr. Sep Drug Dev, 14:2 (1995): p. 64.
68. D. M. Kolb, *Surf. Sci*, 2002. 500: p. 722-740.
69. R. G. Compton and G. H. W. Sanders, Electrode Potentials. Oxford University Press, 1996.
70. Fisher, A.C., Electrode Dynamics. Oxford University Press, 1996.
71. I. K. Robinson and D. J. Tweet, Rep. Prog. Phys, 55 (1992): p. 599.
72. J. Als-Nielsen and D. McMorrow, Elements of Modern X-ray Physics. John Wiley and Sons, Ltd, 2001.
73. R. Feidenhans'l, Surf. Sci. Rep, 10 (1989).

74. J. M. Cowley, *International Tables for Crystallography.* Kluwer Academic Publishers, 1999. Vol C.
75. http://www.ssrl.slac.stanford.edu/absorb.html.
76. F. U. Renner, Y. Grunder, and J. Zegenhagen, Rev. Sci. Instrum, 2007. 78.
77. http://www.esrf.eu/UsersAndScience/Experiments/CRG/BM28.
78. http://www.esrf.eu/UsersAndScience/Experiments/StructMaterials/ID32.
79. http://cep.xor.aps.anl.gov/12bm-info.html.
80. E. Vlieg, J. Appl. Cryst,, 1997. 30,.
81. D. Menzel, Science, 2002. 58: p. 295.
82. P. J. Feibelman, Science, 2002. 99: p. 295.
83. A. Glebov, et al., The Journal of Chemical Physics, 1997. 106: p. 9382.
84. A. P. Seitsonen, et al., Journal of the American Chemical Society, 2001. 123: p. 7347.
85. C. Clay, S. Haq, and A. Hodgson, Physical Review Letters, 2004. 92: p. 046102.
86. http://www.esrf.eu/UsersAndScience/Experiments/SurfaceScience/ID32/Preparation_Labs/SurfaceLab.html.
87. N. Materer, et al., Surface Science, 1995. 325: p. 207.
88. M. Nakamura, et al., Surf. Sci, 2004. 563.
89. E. Vleig, Journal of Applied Crystallography, 1997. 30: p. 532.
90. G. Held, et al., The Journal of Chemical Physics, 2005. 123: p. 064711.
91. K. Bedurftig, et al., The Journal of Chemical Physics, 1999. 111: p. 11147.
92. N. S. Marinkovic, N. M. Markovic, and R. R. Adzic, Journal of Electroanalytical Chemistry, 1992. 330: p. 433.
93. C. A. Lucas, Electrochim. Actas, 2002. 47.
94. P. J. Feibelman, Physical Review B, 1997. 56: p. 2175.
95. D. M. Kolb, *Prog. in Surf. Sci.*, 1996(51): p. 109-173.
96. V. A. Marichev, V.A., *Surf. Sci. Rep*, 2005(56): p. 277-324.
97. M. A. Schneeweiss, et al., *Anodic Oxidation of Au(111).* Canadian Journal of Chemistry, 1997. 75: p. 1703-1709.
98. X. Gao, A. Hamelin, and M. J. Weaver, *Atomic relaxation at ordered electrode surfaces probed by scanning tunneling microscopy: Au(111) in aqueous solution compared with ultrahigh-vacuum environments.* The Journal of Chemical Physics, 1991. 95(9): p. 6993-6996.

99. J. Wang, et al., *In situ x-ray-diffraction and -reflectivity studies of the Au(111)/electrolyte interface: Reconstruction and anion adsorption.* Physical Review B, 1992. 46(16): p. 10321-10338.

100. J. Perdereau, J. P. Biberian, and G. E. Rhead, J. Phys, 1974. F 4: p. 1978.

101. A. R. Sandy, et al., *Structure and phases of the Au(111) surface: X-ray-scattering measurements.* Physical Review B, 1991. 43(6): p. 4667.

102. J. V. Barth, et al., *Scanning tunneling microscopy observations on the reconstructed Au(111) surface: Atomic structure, long-range superstructure, rotational domains, and surface defects.* Physical Review B, 1990. 42(15): p. 9307.

103. Y. Wang, N. S. Hush, and J. R. Reimers, *Simulation of the Au(111)-(22 x sqrt(3)) surface reconstruction.* Physical Review B (Condensed Matter and Materials Physics), 2007. 75(23): p. 233416.

104. Sandy, A.R., et al., *Structure and phases of the Au(111) surface: X-ray-scattering measurements.* Physical Review B, 1991. 43(6): p. 4667.

105. See reference [65]

106. T. J. Schmidt, et al., *Oxygen electrocatalysis in alkaline electrolyte: Pt(hkl), Au(hkl) and the effect of Pd-modification.* Electrochimica Acta, 2002. 47(22-23): p. 3765-3776.

107. M. A. Schneeweiss, D. M. KolB., D. Liu, and D. Mandler, *Anodic Oxidation of Au(111).* Canadian Journal of Chemistry, 1997. 75: p. 1703-1709.

108. N. Furuya and M. Shibata, *Structural changes at various Pt single crystal surfaces with potential cycles in acidic and alkaline solutions.* Journal of Electroanalytical Chemistry, 1999. 467(1): p. 85-91.

109. H. Honbo, S. Sugawara, and K. Itaya, *Detailed in situ scanning tunneling microscopy of single crystal planes of gold(111) in aqueous solutions.* Analytical Chemistry, 1990. 62(22): p. 2424-2429.

110. See referemce [106]

111. Wang, J., et al., *In situ x-ray-diffraction and -reflectivity studies of the Au(111)/electrolyte interface: Reconstruction and anion adsorption.* Physical Review B, 1992. 46(16): p. 10321-10338.

112. B. B. Blizanac, et al., J. Phys. Chem. B, 2004. 108: p. 5304-5313.

113. http://webbook.nist.gov/chemistry

114. C. A. Lucas, et al., *Temperature-Induced Ordering of Metal/Adsorbate Structures at Electrochemical Interfaces.* Journal of the American Chemical Society, 2009. 131(22): p. 7654-7661.

115. A. Hamelin, et al., J. Electroanal. Chem, 1990. 295(291).

116. B. M. Ocko, et al., Phys. Rev. Lett, 1990. 65: p. 1466-1469.

117. See reference [119].

118. M. Labayen, Nat. Mat, 2003. 2: p. 783-787.

119. D. L. Abernathy, et al., *Physical Review B*, 1992. *45*: p. 9272-9291.

120. H. You, unpublished data.

121. X. Gao, et al., Surf. Sci. Rep, 1993. 296(333).

122. D. Kaminski, et al., J. Phys. Chem. C, 2007. 111: p. 17067-17073.

123. K. Krug, J. Stettner, O. M. Magnussen, private communication (2009).

124. T. Wandlowski, et al., J. Phys. Chem. B, 1996. 100: p. 10277-10287.

125. Lucas, C.A., et al., *Temperature-Induced Ordering of Metal/Adsorbate Structures at Electrochemical Interfaces.* Journal of the American Chemical Society, 2009. 131(22): p. 7654-7661.

126. See reference [34]

127. Y. V. Tolmachev, et al., Electrochem. and Solid-State Lett, 2004. 7: p. E23.

128. I. Villegas and M. J. Weaver, J. Chem. Phys, 1994. 101: p. 1648-1660.

129. *The precise nature of the oxygenated species has yet to be confirmed by spectroscopic methods.*

130. A. Lopez-Cudero, A. Cuesta, and C. Gutierrez, J. Electroanal. Chem, 2005. 579: p. 1-12.

131. D.S. Strmcnik, et al., Journal of the American Chemical Society, 2008. 130: p. 15332-15339.

132. A. Cuesta, et al., ChemPhysChem, 2006. 7: p. 2346-2351.